Università degli Studi di Napoli *Federico II*

DOTTORATO DI RICERCA IN FISICA
ciclo XXXVI

Coordinatore: Prof. Vincenzo Canale

Biocompatible Fabrication of TMDs Nanosheets: Theoretical and Experimental Studies on Bacterial Interactions and Radiation-Induced Modification

Settore Scientifico Disciplinare : FIS/07

Dottorando:
Jaber Adam Musa Ibrahim

Tutor:
Prof. Carlo Altucci

Anni 2021/2024

List of Publications

[1] **Jaber Adam**, Maria Rosaria Del Sorbo, Jasneet Kaur, et al. Surface interactions studies of novel Two-dimensional molybdenum disulfide with gram-negative and gram-positive bacteria. *Analytical Letters*, 56(2):357–371, 2023.

[2] **Jaber Adam**, Manjot Singh, Avazbek Abduvakhidov, et al. The effectiveness of cyrene as a solvent in exfoliating 2D TMDs nanosheets. *International Journal of Molecular Sciences*, 24(13):10450, 2023.

[3] M. Singh, D. Bianco, **Jaber Adam**, A. Capaccio, S. Clemente, M. R. Del Sorbo, C. Feoli, J. Kaur, C. Nappi, R. Panico, G. Rusciano, M. Rossi, A. Sasso, M. Valadan, A. Cuocolo, E. Battista, P. A. Netti, and C. Altucci. Gamma rays impact on 2D-MoS_2 in water solution. *Submitted for publication in Scientific Reports*, 2024.

Declaration of Originality

I, **Jaber Adam Musa Ibrahim**, affirm that this thesis is the outcome of my original research, with due acknowledgment of all sources and references. I confirm the originality of the content, ensuring it has not been submitted for any other academic award and that proper citation accompanies ideas, data, or statements from external sources. Contributions from others are duly recognized. I am aware of the consequences of academic misconduct and declare that this thesis has not been previously submitted elsewhere. This work stands as an authentic and original contribution to knowledge.

Copyright Statement

Jaber Adam Musa Ibrahim
Jaber.adam@unina.it

Abstract

Two-dimensional transition metal dichalcogenides (TMDs) nanosheets exhibit exceptional electronic, optical, and mechanical properties, making them attractive for various applications. However, traditional fabrication methods often employ harsh solvents and hinder control over TMDs-environment interactions. This thesis addresses these limitations by exploring biocompatible strategies for TMDs nanosheet fabrication, investigating their properties, and envisioning biocompatible applications.

A somewhat novel theoretical framework, based on the extended Deriaguin-Landau-Verwey-Overbeek (DLVO) model, is developed to understand the interactions between TMDs nanosheets and bacteria in biocompatible solvents. The DLVO model is a theory for simulating the interactions between two particles into a stable colloidal dispersion. In such a context these interactions are driven by the zeta potential and possible coulombic forces due to the ionic surrounding environment. Here we present a novel extension of this model to account for the interactions of TMDs nanosheets in solution with biological membranes. This extended model guides the design of TMDs for targeted antimicrobial therapies.

Liquid-phase exfoliation (LPE) is adopted as the TMDs nanosheets fabrication technique. LPE is carried on in water and another pretty novel, supposed-to-be biocompatible solvent, cyrene. Cyrene is explored as an alternative route for high-quality MoS_2 and WS_2 nanosheets. The impact of cyrene's properties on nanosheet characteristics is investigated experimentally and theoretically, expanding the toolbox of biocompatible TMDs fabrication methods.

Furthermore, this thesis investigates the modification of TMDs nanosheet properties using radiation within an aqueous environment. Radiation-induced changes are analyzed, and underlying mechanisms are elucidated using Monte Carlo simulations. These findings hold promise for applications such as targeted drug delivery, radiosensitization, and localized radiotherapy.

This thesis lays the foundation for developing novel TMDs-based applications that prioritize safety, biocompatibility, and environmental impact. It demonstrates the potential of TMDs in biocompatible environments, opening doors for responsibly designed and effective technologies.

Keywords: 2D-MoS_2, 2D-WS_2, two-dimensional nanomaterials, liquid phase exfoliation, cyrene, DLVO, bacteria-surface interaction.

Acknowledgements

In the name of ***Allah***, the Most Gracious, the Most Merciful. First and foremost, I thank ***Allah*** for granting me the strength, patience, and wisdom to complete this PhD journey. Without His guidance and blessings, this achievement would not have been possible.

I would like to express my heartfelt gratitude to my PhD supervisor, ***Prof. Carlo Altucci,*** who has been a true role model in science for me. His remarkable intelligence, openness to ideas, and insightful guidance have been invaluable throughout my research journey. I greatly appreciate the freedom and encouragement he provided during my PhD. His kindness, support, and sense of humor created an inspiring and supportive environment. I am truly fortunate to have had such an exceptional supervisor.

I am profoundly grateful to my group members for their invaluable support throughout this journey. To the postdoctoral researchers ***Dr. Mohammadhassan Valadan*** and ***Dr. Manjot Singh,*** with whom I worked closely, your expertise and guidance have been indispensable. I also extend my heartfelt thanks to the current and former PhD students in our group for the engaging discussions, collaborative spirit, and unforgettable memories we've shared.

Special thanks to our esteemed ***collaborators*** for their invaluable contributions and insights. Your support and expertise have profoundly enriched my research, and I deeply appreciate the depth and breadth you have brought to this work.

I would also like to thank ***Prof. Vincenzo Canale,*** our PhD coordinator, for his guidance and support throughout this program. Special thanks to ***Mr. Guido Celetano***, the Department of Physics Secretary, whose invaluable assistance and efficiency were consistently crucial. Guido was always there when needed, providing timely help and ensuring everything ran smoothly. His unwavering support made a significant difference in navigating the program's challenges.

I sincerely appreciate the reviewers of my PhD thesis, ***Prof. Josuè Mota Morales*** and ***Prof. Matteo Ceccarelli***. Your thorough evaluation and constructive feedback have been instrumental in refining and strengthening my work.

To my mother (***Zahraa***), whose boundless love and relentless efforts have profoundly shaped my personality and provided me with an education she herself never had the chance to receive, I owe everything I am today to her. Her unwavering support, deep sacrifices, and endless encouragement have been the cornerstone of my journey. I am deeply grateful to my father (***Adam***), whose guidance and support, even from afar, have been a constant source of strength. His encouragement has been instrumental in my achievements.

To my brothers, ***Abaker***, ***Tarig***, and ***Mohamed***, and to my sisters, ***Fatoma*** (may Allah grant her Jannah) and ***Souhier***, your steadfast support and boundless love have been my guiding light. As the youngest, I've been fortunate to benefit from all the wisdom and guidance you've generously shared. To all my ***nieces*** and ***nephews***, whose joy and inspiration continually enrich our family, I am deeply grateful. I love each of you dearly.

I also want to acknowledge the ***Sudanese community in Naple***s, who have been like a family to me. Your companionship and support have made my time here feel like home.

I would also like to express my heartfelt gratitude to the University of Napoli Federico II, Physics Department, and the Government of Italy for providing me with the scholarship to pursue my PhD. Your support has been instrumental in my academic journey. Additionally, I am profoundly thankful to the beautiful city of Napoli for the rich experiences in its vibrant food culture and the warmth of its people. "***Grazie***" for making this chapter of my life truly memorable.

Lastly, to ***myself*** - well done! You have persevered through challenges, embraced opportunities, and come out stronger. Keep believing in yourself, and remember, the journey is as important as the destination.

Contents

List of Figures

List of Tables

List of Equations

List of Abbreviations

AFM	Atomic Force Microscopy
DLVO	Derjaguin, Landau, Verwey and Overbeek (DLVO) theory
DLS	Dynamic Light Scattering
DMF	Dimethylformamide
GO	Graphene Oxide
LPE	Liquid Phase Exfoliation
MoS_2	Molybdenum Disulfide
NMP	N-methyl-2-pyrrolidone
NSs	Nanosheets
SEM	Scanning Electron Microscopy
TMDs	Transition Metal Dichalcogenides
WS_2	Tungsten Disulfide
XPS	X-ray Photoelectron Spectroscopy

Chapter 1

Introduction

1.1 Nanomaterials

Recent advancements in material science have placed nanomaterials at the forefront of scientific inquiry. Their exceptional properties, distinct from those observed in bulk materials, arise from the unique behavior of matter at the nanoscale. This has ignited significant interest from researchers and engineers across various disciplines, as these novel materials hold immense potential for groundbreaking applications. The term "nano" derives from the Greek word "nanos," meaning dwarf, given the characteristically small size regime of these materials. Typically, nanomaterials possess dimensions ranging from 1 to 100 nanometers, leading to the emergence of uniqe physical, chemical, and biological properties[1, 2].

Within nanomaterials, distinctions based on dimension further clarify their varied structures and functionalities. Based on the dimensions, we can classify nanomaterials as zero-dimensional, one-dimensional, two-dimensional, and three-dimensional. Zero-dimensional (0D) nanomaterials, all three dimensions (length, width, height) are confined to the nanoscale, such as quantum dots [3] and fullerenes[4], exhibit confinement in all three spatial dimensions, resulting in quantum confinement effects that impart unique optical and electronic properties. One-dimensional (1D) nanomaterials, the width and height are confined to the nanoscale, while the length extends beyond the nanoscale, represented by nanotubes [5] and nanowires[6], demonstrate extended length along one dimension while retaining nanoscale diameter, facilitating applications in electronics, sensors, and energy storage. Two-dimensional (2D) nanomaterials the thickness is confined to the nanoscale, while the length and width extend beyond it, represented by graphene [7] and transition metal dichalcogenides [8], possess atomic-scale thickness with extended lateral dimensions, enabling exceptional mechanical, electrical, and thermal properties. Lastly, three-dimensional (3D) nanomaterials materials, while not all dimensions are strictly within the nanoscale, these materials possess nanoscale features throughout their structure, including nanoporous structures and nanostructured composites, exhibit nanoscale features distributed throughout three-dimensional space, offering tailored properties for applications in catalysis, filtration, and biomedical scaffolds [9].

Furthermore, the potential applications of nanomaterials are remarkably diverse, spanning a wide range of disciplines including medicine, electronics, energy, and environmental remediation. From targeted drug delivery systems with enhanced efficacy to ultra-sensitive sensors with unprecedented detection capabilities, nanomaterials are revolutionizing various industries and fostering groundbreaking advancements in scientific and technological fields[10].

1.2 2D Nanomaterials

Leveraging the fundamental principles of nanomaterials established earlier, this section delves into the unique properties of two-dimensional (2D) nanomaterials. Characterized by their atomic-scale thickness and extended in-plane dimensions, 2D materials exhibit a fascinating interplay between quantum confinement effects and surface interactions. This unique interplay leads to the emergence of novel properties not observed in their bulk counterparts. The reduction in dimensionality grants 2D nanomaterials an exceptionally high surface-to-volume ratio. This amplified surface area significantly enhances their reactivity, mechanical strength, and electrical conductivity. Additionally, the atomic-scale thickness translates to remarkable flexibility and transparency, further broadening their potential applications across diverse fields[11].

The isolation of graphene in 2004 by Andre Geim and Konstantin Novoselov (Nobel Prize in Physics, 2010) marked a pivotal moment in the field of 2D nanomaterials [12]. This groundbreaking discovery involved successfully isolating a single atomic layer of carbon atoms arranged in a hexagonal lattice, a material now known as graphene. Graphene's exceptional properties, including remarkable mechanical strength, exceptional electrical conductivity, and high optical transparency, sparked significant scientific interest [12]. Furthermore, the success with graphene ignited an intense pursuit of other 2D nanomaterials with the potential to exhibit similarly extraordinary or even entirely novel properties, propelling research and innovation in this growing field [7].

Among the diverse array of 2D nanomaterials that have since been discovered or synthesized, notable examples include transition metal dichalcogenides (TMDs), graphene oxide (GO)[13], boron nitride nanosheets [14], black phosphorus[15]. Beyond these examples, many other 2D nanomaterials continue to emerge as promising candidates for diverse applications. Examples like black phosphorus (phosphorene)[16], with its tunable bandgap and excellent carrier mobility, hexagonal boron nitride (h-BN)[17], an insulator possessing superb thermal conductivity, and Xenes (monoelemental 2D materials like silicene and germanene) offer unique properties. MXenes [18](2D transition metal carbides, nitrides, and carbonitrides) also demonstrate metallic conductivity and surface functionality, while layered double hydroxides (LDHs) feature tunable compositions and biocompatibility[19]. Each of these materials possesses unique chemical, mechanical, electrical, and optical properties, rendering them highly versatile for applications spanning electronics, photonics, sensing, catalysis, and beyond.

Transition metal dichalcogenides (TMDs) constitute a distinguished class of 2D nanomaterials characterized by layers of transition metal atoms intercalated between chalcogen atoms, Figure 1.1 shows the transition metals and chalcogen elements in the periodic table. This distinctive atomic arrangement imbues TMDs with a rich spectrum of electronic [20, 21], optical [22, 23], chemical[24, 25], thermal [26, 27], mechanical [28] and catalytic properties [29], making them highly sought-after materials for a wide range of applications. TMDs, positioned within the periodic table between metals and nonmetals, exhibit fascinating phenomena at the nanoscale owing to their unique bonding configurations and structural flexibility.

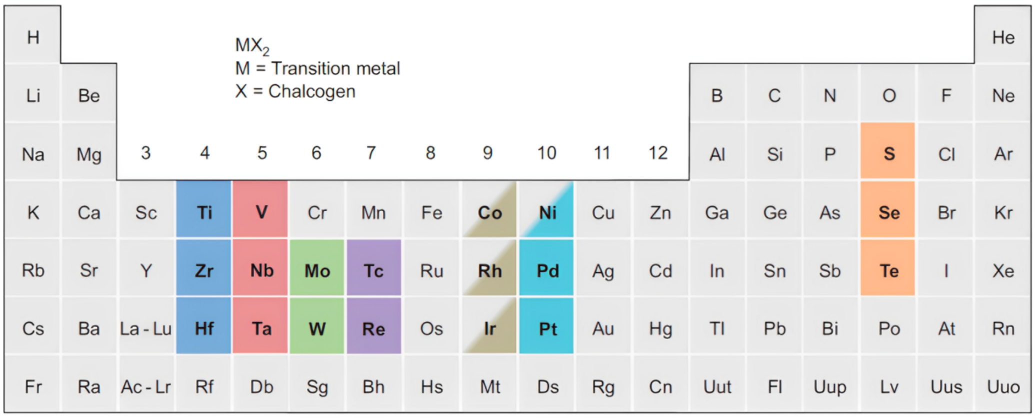

Figure 1.1: Highlighted on the periodic table are transition metals and chalcogen elements such as S, Se, and Te, known for their tendency to form 2D layered crystalline structures. Note the partial highlighting for Co, Rh, Ir, and Ni, indicating their limited involvement in forming these layered structures among certain dichalcogenides, adapted from [30]

Among the prominent transition metal dichalcogenides (TMDs), molybdenum disulfide (MoS_2) [31] and tungsten disulfide (WS_2) [32] have emerged as frontrunners for exploration in various fields. These layered materials share a similar crystal structure, but subtle differences in their atomic composition lead to unique properties. Both MoS_2 and WS_2 exhibit excellent biocompatibility and high surface areas, making them promising candidates for drug delivery and biomedical imaging applications [33, 34]. This combination of distinct properties and potential applications positions MoS_2 and WS_2 as key players among the other 2D nanomaterials.

Molybdenum disulfide (MoS_2) nanosheets have emerged as a revolutionary material with immense potential in biomedicine. These nanosheets are a specific type of two-dimensional (2D) transition metal dichalcogenide (TMD) characterized by a unique layered structure [33] Figure 1.2 shows MoS_2 crystal structure. Each layer consists of a central molybdenum (Mo) atom sandwiched between two hexagonal planes of sulfur (S) atoms, forming a honeycomb-like lattice [35]. This particular arrangement gives rise to remarkable properties that make MoS_2 nanosheets particularly attractive for biomedical applications.

One key property of MoS_2 nanosheets is their large surface area. Similar to graphene, MoS_2 nanosheets possess an exceptionally high surface area due to their ultrathin, 2D nature [33]. This vast surface area allows for efficient loading and conjugation of biomolecules, drugs, or imaging agents. This makes them ideal for drug delivery and bioimaging applications, as a larger surface area allows for more molecules to be attached, increasing their efficacy [36].

Another fascinating property of MoS_2 nanosheets is their thickness-dependent bandgap. MoS_2 exhibits a unique characteristic where its bandgap (energy difference between valence and conduction bands) varies depending on the number of layers [35]. This tunable bandgap allows for precise control over its optical and electrical properties. This controllability is crucial for designing targeted therapies and biosensors, as researchers can tailor the material's properties for specific applications [35].

MoS_2 nanosheets also have strong absorbance in the light spectrum's near-infrared (NIR) region. This property is advantageous for photothermal therapy applications [33, 34]. NIR light penetrates deep into tissues with minimal side effects. MoS_2 nanosheets can convert this light into heat, enabling targeted destruction of diseased cells through a process called photothermal therapy [33, 34].

The unique properties of MoS_2 nanosheets open doors to a multitude of exciting possibilities in biomedicine. For example, MoS_2 nanosheets can be employed as carriers for targeted drug delivery. Their high surface area allows for efficient drug loading, and their surface chemistry can be tailored to achieve specific targeting of diseased cells [36]. Additionally, the NIR absorption property of MoS_2 nanosheets makes them excellent agents for photothermal therapy. Upon NIR irradiation, they generate heat that can destroy cancer cells with minimal damage to surrounding healthy tissues [33, 34]. Furthermore, in biosensing applications, MoS_2 nanosheets can be engineered into highly sensitive biosensors for the detection of various biomarkers associated with diseases. Their unique electrical properties allow for the specific detection of biomolecules with high accuracy [35].

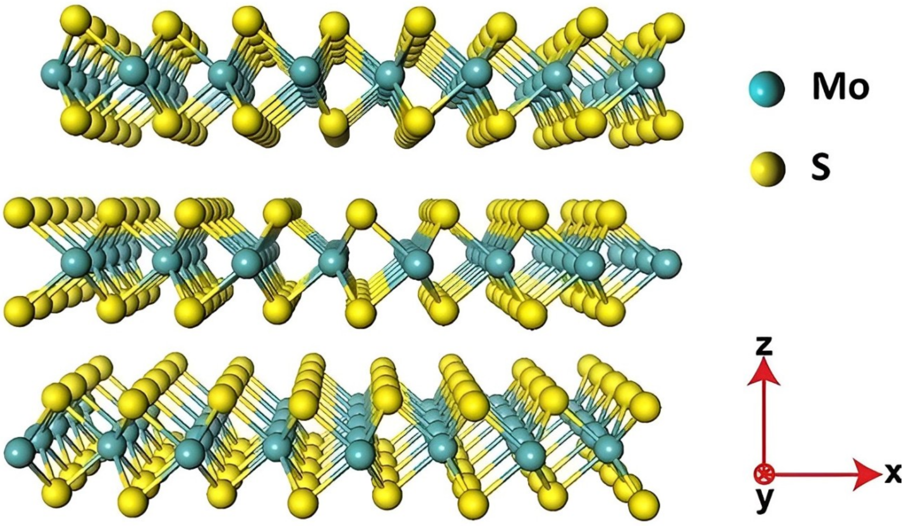

Figure 1.2: Crystal structure of MoS_2, adapted from [37]

WS_2 nanosheets, on the other hand, consist of one tungsten atom (W) bonded to two sulfur atoms (S). They form a layered structure, with each layer composed of a sheet of tungsten atoms sandwiched between two layers of sulfur atoms. Similar to MoS_2, WS_2 nanosheets offer unique properties due to their thin structure, consisting of just a few atomic layers, and a large surface area [38, 39]. This large surface area is advantageous for interactions with biological systems, making WS_2 nanosheets attractive for biomedical applications such as drug delivery systems. Their surface can bind to drugs or other therapeutic molecules, allowing for targeted drug delivery to diseased cells and potentially improving treatment efficacy while reducing side effects [40].

These properties make WS_2 nanosheets promising candidates for drug delivery systems. Their large surface area allows them to bind to drugs or other therapeutic molecules [40]. Researchers are exploring their use as carriers to deliver drugs directly to diseased cells. This could potentially improve treatment efficacy and reduce side effects by targeting only the diseased area [40].

Another promising application of WS_2 nanosheets lies in tissue engineering. Their properties, including good electrical conductivity and potential biocompatibility, could be beneficial for cell growth and improved functionality of engineered tissues [38, 39]. For instance, research has been conducted on using WS_2 nanosheets to reinforce DNA hydrogels for tissue engineering applications [38].

The electrical properties and large surface area of WS_2 nanosheets also make them suitable for use in biosensor development [39]. These sensors could potentially detect biological molecules or pathogens, aiding in disease diagnosis.

In terms of photothermal therapy, WS_2 nanosheets also possess strong NIR absorption, similar to MoS_2, which can be utilized to generate heat for the destruction of cancer cells with minimal damage to surrounding tissues. However, WS_2 nanosheets may offer higher efficiency in some applications due to their different electronic properties [40].

In biosensing, WS_2 nanosheets can be used to create highly sensitive biosensors, similar to MoS_2. Their excellent electrical conductivity and large surface area allow for the detection of biomolecules with high accuracy, making them suitable for various diagnostic applications [39].

1.3 Fabrication Methods

In nanomaterial fabrication, two primary approaches dominate, (I) top-down and (ii) bottom-up methods. These methodologies represent distinct strategies for synthesizing nanomaterials, each with advantages and limitations.

Top-down fabrication involves downsizing bulk materials into nanoscale structures through mechanical, chemical, or lithographic techniques. This method offers precise control over the size, shape, and composition of resulting nanomaterials. Mechanical exfoliation, a prominent top-down technique, relies on the mechanical cleavage or peeling of bulk materials, such as graphite, to produce thin layers of nanomaterials like graphene [41]. Another top-down approach is lithography, where patterns are defined on a substrate using photolithography or electron beam lithography, followed by selective etching or deposition to create nanoscale features [42]. Chemical etching is also commonly employed, involving the selective removal of material from a substrate using chemical reactions[43].

Conversely, bottom-up fabrication relies on the self-assembly of atoms or molecules to construct nanomaterials from the ground up. This approach enables precise control over atomic arrangements and structural properties, yielding materials with tailored functionalities. Chemical vapor deposition (CVD) is a prominent bottom-up technique wherein precursor gases react on a substrate surface to form nanomaterials. For example, in synthesizing graphene by CVD, hydrocarbon precursors decompose on a metal catalyst substrate, leading to the growth of graphene layers [44]. Molecular beam epitaxy (MBE) is another bottom-up method where atoms or molecules are deposited layer by layer to build up nanostructures with atomic precision [45]. Self-assembly processes, such as sol-gel synthesis [46] or molecular self-assembly, rely on the spontaneous organization of molecules into ordered structures, offering a bottom-up approach to nanomaterial fabrication.

Liquid phase exfoliation (LPE), one of the top-down approaches, has emerged as a versatile and scalable technique for synthesizing two-dimensional nanomaterials from bulk-layered materials. In LPE, bulk materials are dispersed in a solvent and subjected to mechanical or chemical exfoliation processes, leading to the isolation of individual nanosheets dispersed in the liquid phase. This method offers several advantages, including simplicity, scalability, and the ability to produce high-quality nanomaterials with minimal defects [47].

Several variants exist within LPE method, each with unique mechanisms and applications. These include sonication-assisted exfoliation, where ultrasonic waves are used to break apart layered structures and promote nanosheet dispersion, and shear-assisted exfoliation, where mechanical forces are applied to induce exfoliation [48]. Additionally, chemical exfoliation methods involving intercalation of solvents or surfactants between layers can enhance exfoliation efficiency and yield pristine nanosheets [49].

Sonication, in particular, has emerged as a widely employed technique for liquid phase exfoliation due to its simplicity and effectiveness. Ultrasonic waves generated by a sonicator probe induce cavitation in the liquid medium, creating localized pressure differentials and shear forces that promote the exfoliation of layered materials. This gentle yet efficient process enables the production of large quantities of dispersed nanosheets with controlled thickness and size distribution, making sonication a cornerstone technique in the fabrication of two-dimensional nanomaterials for various applications [50], Figure 1.3 shows a schematic view of the liquid phase exfoliation procedure.

The choice of solvent is essential in this process. Considerable effort has been dedicated to identifying suitable solvents by analyzing their chemical and physics interactions with nanosheets, focusing on factors such as surface tension and Hansen solubility parameters, which significantly influence the exfoliation efficiency, material quality, and suitability for various applications [52, 53]. Prior attempts at exfoliation typically utilized solvents

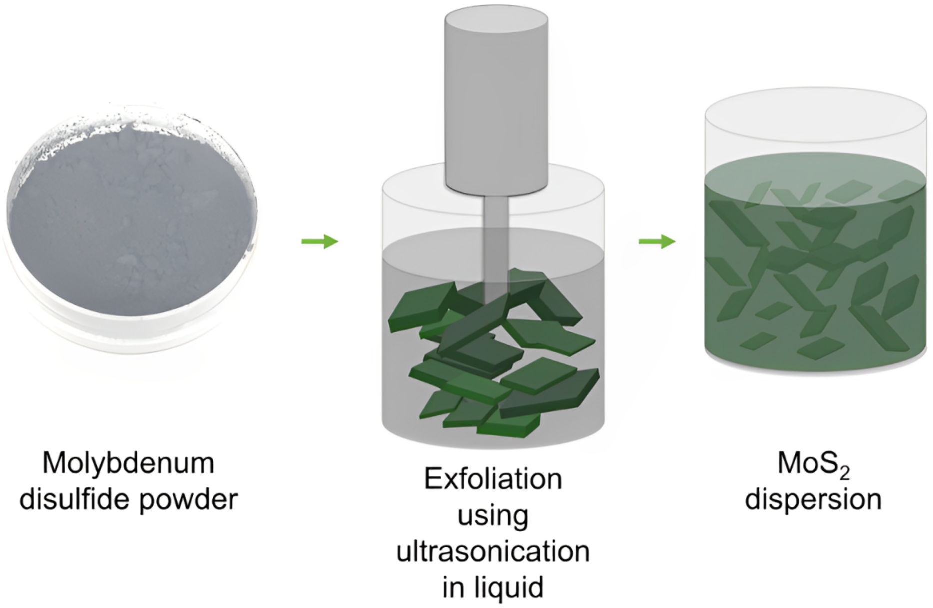

Figure 1.3: A schematic depicting the liquid phase exfoliation procedure. The process begins with molybdenum disulfide powder and concludes with the dispersion of exfoliated nanosheets in the chosen solvent. While the diagram focuses on molybdenum disulfide, the procedure is applicable to other layered materials as well, adapted from [51]

that, while effective in yielding nanosheets, posed considerable drawbacks, particularly in the context of biomedical applications, due to their toxicity and environmental impact [50].

For instance, conventional organic solvents such as N-methyl-2-pyrrolidone (NMP) and dimethylformamide (DMF) have been widely employed in nanomaterial synthesis due to their strong solvation power and ability to disperse layered materials effectively. However, their toxicity profiles and potential environmental hazards limit their applicability in biomedical and eco-friendly applications [54, 55, 56]. Similarly, while effective in exfoliation, chlorinated solvents like chloroform and dichloromethane raise concerns regarding human health and environmental sustainability [57, 58].

The toxicity of these conventional organic solvents arises from their ability to disrupt biological processes, induce cellular damage, and pose health risks upon exposure. Their persistence in the environment further intensifies their adverse effects, highlighting the need for safer and more sustainable alternatives in nanomaterial synthesis [59, 60].

NMP is classified as a reproductive toxicant and a potential developmental toxin. It can be absorbed through the skin, inhalation, or ingestion, leading to systemic toxicity. NMP disrupts cellular function by interfering with enzyme activity and membrane structure. Prolonged or high-level exposure to NMP has been linked to adverse reproductive effects, including miscarriages, developmental abnormalities, and infertility. Additionally, NMP is persistent in the environment, contributing to soil and water contamination [61].

DMF is known to cause skin and eye irritation upon contact. It is readily absorbed through the skin and inhalation, leading to systemic toxicity. DMF can disrupt cellular membranes and interfere with metabolic processes, resulting in liver and kidney damage. Chronic exposure to DMF has been associated with adverse health effects, including reproductive toxicity, neurotoxicity, and carcinogenicity. Furthermore, DMF is flammable and poses fire hazards, increasing its risk profile [56].

On the other hand, the emergence of cyrene as a bio-based solvent represents a promising advancement in green chemistry. Cyrene, a bio-based solvent derived from cellulose, possesses a unique combination of physical and chemical properties, making it highly suitable for a wide range of industrial applications. Chemically, cyrene is characterized as a polar aprotic solvent, owing to its ability to solvate a wide range of polar and nonpolar compounds alike. This unique property makes cyrene exceptionally versatile, enabling it to dissolve various materials, including organic compounds, polymers, and nanomaterials, easily [62, 63]. Additionally, cyrene exhibits a relatively high boiling point and low viscosity, facilitating efficient processing and handling across a broad temperature range. Furthermore, cyrene is renowned for its low toxicity profile, making it a safer alternative to many conventional organic solvents. Its nature further enhances its eco-friendly credentials, ensuring minimal environmental impact throughout its lifecycle. These combined physical and chemical properties position cyrene as a promising solvent of choice for sustainable manufacturing processes across industries ranging from pharmaceuticals and cosmetics to nanotechnology and beyond [64].

Cyrene's appeal lies in its multifaceted advantages, making it a desirable option for nanomaterial synthesis. Firstly, its high polarity facilitates efficient solvation and dispersion of a wide range of materials, including layered nanosheets like MoS_2 and WS_2. This inherent property enables effective intercalation between layers, thereby promoting exfoliation and generating nanoscale materials with controlled thickness and morphology [65].

Moreover, cyrene's low toxicity profile is of great importance, particularly in applications where the final nanomaterials may come into contact with biological systems or the environment, for example cyrene also emerges as a promising ally in the fight against food spoilage, offering a bio-based solution to extend shelf life and preserve the taste and nutritional value of perishable foods [66]. Unlike conventional organic solvents that may pose health hazards and environmental risks, cyrene offers a safe and sustainable alternative, ensuring the integrity of both the synthesis process and the resulting nanomaterials. Additionally, cyrene's biodegradability further enhances its appeal as a green solvent. As a solvent derived from renewable sources, cyrene undergoes natural degradation processes, minimizing its environmental footprint and contributing to overall sustainability. This characteristic aligns with the growing global emphasis on circular economy principles, where the end-of-life fate of chemicals and materials is carefully considered to minimize waste and resource depletion [67].

In essence, cyrene's emergence as a bio-based solvent represents not only a technological advancement but also a paradigm shift towards more sustainable and environmentally conscious practices in nanomaterial synthesis. Its unique combination of high polarity, low toxicity, and biodegradability positions cyrene as a frontrunner in the quest for greener solvents, offering unprecedented opportunities for the development of next-generation nanotechnologies with minimal ecological impact [68].

1.4 TMDs Applications

Transition metal dichalcogenides (TMDs) have attracted significant interest not only for their electronic and optical properties but also for their potential applications in biomedicine. The exploration of TMDs in biomedical research extends to various areas, including drug delivery, imaging, biosensing, and antibacterial applications. One particularly intriguing aspect of TMDs' biomedical potential lies in their surface interactions with pathogens, such as bacteria, and their implications for infection control and therapeutic interventions[69, 33].

Understanding the surface interaction between TMDs and different pathogens, including bacteria, is paramount for several reasons. Firstly, bacteria pose a significant threat to public health, causing various infectious diseases ranging from mild to life-threatening. With the rise of antibiotic-resistant bacteria, there is an urgent need for alternative strategies to combat bacterial infections. TMDs present a promising avenue due to their unique physicochemical properties and the possibility of tailored surface modifications to enhance antibacterial efficacy.

Moreover, the surface interaction between TMDs and bacteria is crucial in determining the outcome of various biomedical applications. For instance, in drug delivery systems utilizing TMDs as carriers, the interaction between the nanomaterial surface and bacterial membranes can influence drug release kinetics, biodistribution, and therapeutic efficacy. Similarly, in biosensing applications, the specificity and sensitivity of TMD-based sensors for bacterial detection depend on the recognition and binding events occurring at the material interface.

Furthermore, explanining the surface interaction between TMDs and bacteria provides valuable insights into the mechanisms underlying antibacterial activity, facilitating the design of next-generation antimicrobial materials with enhanced efficacy and selectivity. By understanding how TMDs interact with bacterial membranes, cell walls, and biofilms, researchers can engineer surface properties to promote desirable bactericidal effects while minimizing unintended consequences such as cytotoxicity or immune response activation.

The interaction between MoS_2 nanosheets and bacteria stands as a critical domain of inquiry, bearing significant implications for biomedical applications and environmental stewardship. These nanosheets exhibit multifaceted antibacterial properties, engaging in physical interactions with bacterial membranes while also instigating biochemical processes that induce oxidative stress. Recent investigations have unveiled notable insights into the diverse mechanisms underlying MoS_2 nanosheets' antibacterial activity. Surface-immobilized MoS_2 nanosheets have been observed to exert heightened antibacterial effects against *Escherichia coli*, triggering oxidative stress and morphological damage to bacterial cells [70]. Furthermore, chitosan-exfoliated MoS_2 nanosheets have demonstrated the capacity to depolarize membranes, deactivate metabolism, and induce oxidative stress in both Gram-positive and Gram-negative bacteria [71]. Bi-doped MoS_2 nanosheets exhibit enhanced antimicrobial activity against Staphylococcus aureus and E. coli, suggesting their potential utility in industrial and environmental contexts [72]. However, the deployment of MoS_2 nanosheets also poses environmental risks, as evidenced by their significant reduction of beneficial soil bacteria survival [73]. Moreover, the interaction with MoS_2 nanosheets can lead to phospholipid extraction and structural alterations in E. coli membranes, resulting in bacterial death [74]. The structural nuances of MoS_2, such as nanoflowers, play a pivotal role in influencing antibacterial activity, with specific structures exhibiting superior performance [75]. Additionally, the presence of metallic states on MoS_2 nanosheets' surfaces has been associated with microbial inactivation [76]. These insights not only contribute to our understanding of MoS_2 nanosheets' antibacterial mechanisms but also open avenues for their application, such as in advanced therapy for bacteria-infected wounds through the release of nitric oxide and photothermal activities [77]. Furthermore, the potential impact on carbon and nitrogen metabolism in cyanobacteria hints at broader implications for global biogeochemical cycles [78]. Moreover, the effectiveness of MoS_2 nanosheets in disinfecting multi-drug resistant bacteria underscores their promise for combating antibiotic resistance [79]. These findings collectively underscore the intricate interplay between MoS_2 nanosheets and bacteria, offering insights that could inform the development of novel antibacterial strategies and environmental risk management approaches.

In this doctoral thesis, our primary objective is to synthesize high quality MoS_2 and WS_2 nanosheets via exfoliation methods utilizing environmentally friendly solvents, particularly water and cyrene. The utilization of such green solvents underscores our commitment to sustainable and eco-conscious scientific practices. Our research is motivated by two main aims: first, to investigate the surface interactions between these nanosheets, produced in green solvents, and bacteria, employing the established DLVO (Derjaguin-Landau-Verwey-Overbeek) theory; second, to examine the behavior of MoS_2 nanosheets in radiation environments, a crucial inquiry with implications for diverse fields ranging from materials science to nuclear engineering.

By focusing on the exfoliation of MoS_2 and WS_2 nanosheets in water and cyrene, we contribute to the ongoing endeavor to develop sustainable methodologies within nanomaterial synthesis. These green solvents offer advantages in terms of both environmental impact and safety, aligning with the principles of green chemistry. Through carful experimentation and analysis, we aim to establish robust protocols for the production of high-quality nanomaterials with minimal ecological footprint.

The exploration of surface interactions between nanosheets and bacteria is a pivotal aspect of this research. By employing the DLVO theory, which explains the forces governing colloidal interactions, we seek to understand the mechanisms underlying the behavior of nanomaterials in biological environments. Such insights hold promise for many applications, such as in antimicrobial coatings, drug delivery systems, and environmental remediation technologies.

Furthermore, the investigation into the response of MoS_2 nanosheets to radiation environments is of paramount importance. As nanomaterials find increasing utilization in various radiation-sensitive applications, including nuclear reactors and medical imaging, understanding their behavior under irradiation is crucial for ensuring safety and reliability. Through systematic experimentation and characterization, we endeavor to elucidate the effects of radiation on MoS_2 nanosheets, thus contributing to the advancement of radiation-resistant materials.

1.5 Thesis Outlines

The primary objective of this research is to synthesize two-dimensional transition metal dichalcogenides (TMDs) using environmentally friendly solvents, specifically cyrene and water. The research explores the synthesis process and characterizations and investigates the potential applications of these nanosheets in two distinct areas. Firstly, it examines the interaction between TMDs nanosheets and bacteria to understand their antibacterial properties. Secondly, it analyzes the impact of gamma photons generated from positron annihilation on 2D-MoS_2 nanosheets in a water solution. Both theoretical frameworks, particularly the DLVO theory, Monte Carlo simulation, and experimental methods, are utilized to achieve these goals. Through a combination of synthesis techniques, theoretical modeling, and experimental investigations, this research seeks to contribute to our understanding of the synthesis, properties, and potential applications of environmentally friendly TMD nanosheets.

This doctoral dissertation is structured in an article-based format. Each chapter aligns with a research article that has been published or is currently under consideration for publication in a reputable and peer-reviewed international scientific journal. This approach facilitates the systematic presentation of research results and fosters knowledge sharing within the academic community.

Chapter 1: *Introduction*: The introductory chapter of the thesis provides a comprehensive overview of (2D) nanomaterials, with a particular emphasis on transition metal dichalcogenides (TMDs) such as MoS_2 and WS_2. It begins by discussing nanomaterials in a broad context, investigating their significance and relevance in various fields. Subsequently, the focus narrows down to TMDs, highlighting their unique properties and potential applications. The chapter explores different fabrication methods employed in synthesizing TMDs, providing insights into the rigorous processes involved in their production. Furthermore, it explores the diverse range of applications of TMDs across different domains, highlighting their versatility and significance in contemporary research and technology. Finally, the chapter outlines the structure and content of the thesis, offering a roadmap to navigate through the subsequent chapters.

Chapter 2: *Material and Methods*: The Materials and Methods section of the thesis serves as a detailed guide to the experimental procedures and techniques employed throughout the research. It commences by enumerating the materials utilized in the study, providing a comprehensive list of substances and compounds essential to the experimental investigations conducted. The section then proceeds to explain the Liquid Phase Exfoliation method utilizing ultrasonication, a pivotal technique employed for the synthesis and preparation of TMDs two-dimensional materials used in the thesis. Furthermore, the method of centrifugation is explained, highlighting its role in separating and purifying exfoliated nanomaterials and the size selection.

Subsequently, the section navigates through the characterization techniques employed to analyze the synthesized materials. These include UV-Vis spectroscopy, Raman spectroscopy, Atomic Force Microscopy (AFM), Scanning Electron Microscopy (SEM), Zeta potential analysis, Dynamic Light Scattering (DLS), and X-ray Photoelectron Spectroscopy (XPS). Each technique is discussed in detail, elucidating its principles of operation, experimental setup, and specific application in characterizing the properties and structural features of the synthesized nanomaterials.

Moreover, the section provides an overview of the DLVO theory, an important tool in colloid and surface science, which elucidates the interaction forces between colloidal particles dispersed in a liquid medium. This theoretical framework is crucial for understanding the behavior of nanosheets in solution and provides insights into the mechanisms governing their aggregation and dispersion phenomena, as well as their nanosheets-nanosheets interaction and nanosheets-bacteria interactions.

Furthermore, we explain the details of the Monte Carlo Method, a powerful computational method widely used across scientific fields to model electron and photon transport, crucial for understanding radiation-matter interactions.

Chapter 3: *Surface Interactions Studies of Novel Two-dimensional Molybdenum Disulfide with Gram-Negative and Gram-Positive Bacteria*: This chapter investigates a detailed exploration of the interactions between various strains of gram-negative and gram-positive bacteria and two-dimensional molybdenum disulfide (MoS_2) nanosheets. This investigation is conducted within the context of two environmentally friendly solvents, water and cyrene, thereby highlighting the relevance of the study in sustainable nanomaterial applications. The theoretical framework of the DLVO theory serves as the basis of this exploration, providing a systematic understanding of the forces governing the interactions between nanomaterials and bacterial cells.

The chapter outlines the DLVO model employed. It offers a comprehensive analysis of the results, shedding light on the surface properties of MoS_2 nanosheets and their ability to interact with bacterial cells. Moreover, it explores the implications of these findings in the antibacterial research. This chapter is inspired by an article already published.

Chapter 4: *The Effectiveness of cyrene as a Solvent in Exfoliating 2D TMDs Nanosheets*: This chapter dives deep into a comprehensive investigation of cyrene's viability as an environmentally friendly solvent for the exfoliation process of two-dimensional transition metal dichalcogenide (TMD) nanosheets, specifically focusing on MoS_2 and WS_2. This study evaluates cyrene's performance against traditional solvents, aiming to uncover its potential as a sustainable alternative in nanomaterial processing.

Central to the chapter is the explanation of the experimental methodology employed to assess cyrene's effectiveness, which is liquid phase exfoliation, centrifugation, and characterizations. The DLVO model is used here again to confirm the results. This includes detailed procedures for the synthesis and exfoliation of MoS_2 and WS_2 nanosheets using cyrene, different characterization methods, and comparative analyses against conventional solvents. The results obtained from these experiments are rigorously analyzed, offering insights into cyrene's capacity to facilitate the exfoliation of TMD nanosheets, its impact on the properties of the resulting materials, and it is possible biomedical applications. This chapter corresponds to an article already published.

Chapter 5: *Gamma rays impact on 2D-MoS_2 in Water Solution*: This chapter investigates the impact of 511 KeV photons generated from positron annihilation on the behavior of two-dimensional MoS_2 nanosheets in aqueous solutions. Again, we used the LPE technique to exfoliate the material, followed by centrifugation and detailed characterizations. We also use the Monte Carlo code from the PENELOPE system by F. Salvat et al [80]. We simulated these processes in low-energy scenarios, building on their foundational work in 2001. Through this method, validated by Sempau et al. in 2003 [81], we analyzed complex interactions with precision, employing an adapted simulation algorithm to simulate the gamma radiation propagation through the water solvent and the interactions of the high energy photons with the nanosheets within the water context, which is essential for our research objectives. In the chapter, the discussion is devoted to review experimental setup, results, and implications of the study in understanding the interaction between nanomaterials and gamma radiation, with potential applications in nanomedicine and materials science. This chapter corresponds to an article submitted for publication.

Chapter 6: *Discussion*: The Discussion section acts as the link between the three chapters, all of which are based on articles that are published or submitted for publication. Here, we connect the insights from chapters 3, 4, and 5. Additionally, the Discussion section provides a platform to illustrate how the chapters are linked, showing how the findings from one study support and enhance those of the others. By combining the knowledge from these chapters, we aim to provide a comprehensive understanding of the research topic. This also helps us grasp the broader implications and importance of the research findings. Through a holistic analysis of how these chapters relate to each other, we gain a deeper insight into the research subject.

Chapter 7: *Conclusion and Future Works*: In this chapter, we wrap up the thesis by summarizing the main findings and suggesting where future research could go. It looks back on what the research has accomplished and suggests new paths for study. We bring together the main challenges and how to tackle them. We also consider what questions remain unanswered and what new things could be explored.

We also consider how our research fits into the bigger picture of what's happening in the academic world and how it could be helpful outside of academia.

Chapter 2

Materials and Methods

2.1 Materials

The original bulk molybdenum disulfide (MoS_2) powder (Sigma-Aldrich, Darmstadt, Germany, catalog number: 69860, particle size: 6 μm, purity: 99%, density: 5.06 g/mL at 25 °C) and tungsten disulfide (WS_2) powder (Sigma-Aldrich, Darmstadt, Germany, catalog number: 243639, particle size: 2 μm, purity: 99%, density: 7.5 g/mL at 25 °C) were subjected to exfoliation using water or cyrene, a solvent (Sigma-Aldrich, catalog number: 807796, molecular weight: 128.13 g/mol, flash point: 108 °C, density: 1.25 g/mL). The materials were dispersed in solvent at an initial 5 mg/mL concentration. The solution underwent bath sonication for 15 minutes as a pretreatment step.

2.2 Liquid Phase Exfoliation - Ultrasonication

Synthesis of two-dimensional (2D) transition metal dichalcogenides (TMDs) nanomaterials encompasses diverse methodologies, each with unique advantages and challenges. This study focuses on liquid phase exfoliation, a top-down approach that offers scalability and versatility in producing high-quality nanosheets. Liquid phase exfoliation involves the dispersion of bulk TMDs crystals in a solvent followed by mechanical or chemical energy to separate the layers into nanoscale thickness. Ultrasonication, a commonly employed technique, imparts mechanical energy to break interlayer bonds and facilitate exfoliation. This method is particularly suitable for synthesizing TMDs nanosheets due to its ability to achieve uniform dispersion and control over nanosheets thickness [82].

In the liquid phase exfoliation (LPE) process utilizing ultrasonication, several crucial factors interplay to influence the quality of the produced nanosheets. Ultrasonic power, defining the intensity of the ultrasound waves, is pivotal as it governs the vigor of cavitation, aiding in exfoliating the bulk material into nanosheets. However, finding the optimal balance is essential, as excessive power can lead to overheating and degradation of the nanomaterial. Frequency selection is equally critical, as it determines the size and intensity of cavitation bubbles. Lower frequencies penetrate deeper into the solution, while higher frequencies exert more localized effects, requiring careful consideration based on the specific nanomaterial and solvent system [83, 84].

Duration of sonication directly impacts the extent of exfoliation; longer sonication times generally yield higher nanosheets yields, yet excessive sonication can lead to material degradation [50]. The choice of solvent is crucial for effectively dispersing and exfoliating the material into nanosheets. One important consideration is matching the surface tension of the solvent with that of the material being exfoliated. When the surface tensions are matched, it promotes better wetting and interaction between the solvent and the material's surface, facilitating the exfoliation process. This leads to more efficient dispersion and higher-quality nanosheets [85]. Temperature fluctuations during sonication can affect the mobility of solvent molecules, influencing interlayer separation and, subsequently, exfoliation efficiency. However, maintaining optimal temperatures is crucial to avoid thermal degradation of the nanomaterial. An ice bath is a common method to control and maintain lower temperatures during exfoliation. By immersing the reaction vessel or container containing the solvent and material in an ice bath, heat generated during sonication is dissipated, keeping the temperature within the desired range. This helps preserve the nanomaterial's integrity and ensures that the exfoliation process proceeds without thermal degradation, resulting in high-quality nanosheets [86].

The concentration of the starting material in the solvent affects inter-particle interactions and agglomeration tendencies. Balancing concentration is essential; while higher concentrations may increase agglomeration, lower concentrations may result in fewer nanosheets produced per unit volume of solvent. Additives or surfactants can stabilize nanosheets and prevent re-agglomeration post-exfoliation, necessitating careful selection and concentration [87].

Pre-treatment methods such as chemical functionalization or mechanical milling can modify bulk material surfaces, enhancing exfoliation efficiency. Mechanical shearing forces generated during sonication contribute significantly to exfoliation by breaking apart bulk material into smaller nanosheets. These forces must be controlled to avoid excessive fragmentation. Additionally, the stability of the dispersion and its tendency to re-agglomerate over time are crucial considerations, necessitating proper storage conditions to maintain dispersion stability and nanosheets quality over time. Optimization of these factors through systematic experimentation and careful control is important for achieving high-quality nanosheets via LPE with the sonication method [88].

LPE was performed in this thesis using tip sonication with a Bandelin Ultrasound SONOPLUS HD3200, Berlin, Germany (operating frequency of 20 kHz and maximum power of 200 W) tip sonicator equipped with a probe (KE-76). The materials were dispersed in the solvent at a predefined initial concentration; then, the solution was pretreated with bath sonication for 15 min and then subjected to exfoliation in a quartz bottle using pulse mode (10 seconds on, 10 seconds off). Sonication was conducted in an ice bath to prevent overheating due to cavitation bubble collisions, maintaining the device's operating temperature at 15 °C. Output power was monitored to ensure consistency throughout sonication, resulting in a uniform dispersion.

2.3 Centrifugation

After the ultrasonication process, centrifugation serves as a vital step to further refine the dispersed nanosheets by separating them from any residual bulk crystals and large aggregates that may still be present in the solution and separating nanosheets based on their size selectively. This purification step is essential for obtaining a high-quality nanosheets dispersion. Centrifugation parameters, including the speed and duration, are carefully optimized to achieve efficient separation and concentration of the nanosheets [89].

Liquid phase exfoliation generally produces nanosheets that exhibit a wide range of lateral size and thickness. Backes et al. pioneered the liquid cascaded centrifugation technique, providing a method that offers a sophisticated approach to achieving precise size selection and purification of nanosheets. This method involves a series of centrifugation steps, each with specific parameters tailored to progressively isolate nanosheets of desired sizes. Initially, lower centrifugation speeds are applied to the dispersion, targeting removing larger particles and aggregates that might still be present after ultrasonication. These larger contaminants tend to sediment more rapidly under lower centrifugal forces, allowing for their separation from the dispersed nanosheets. Following this initial centrifugation step, the supernatant containing the dispersed nanosheets is collected, and subsequent rounds of centrifugation are conducted at progressively higher speeds. These higher speeds are designed to target smaller particles and finer nanosheets, allowing for further refinement of the nanosheets dispersion. The cascaded centrifugation method enables precise control over the size selection process by iteratively adjusting the centrifugation parameters, such as speed and duration. This iterative approach allows for the separation of nanosheets based on their size distribution, ultimately leading to the isolation of a homogeneous population of nanosheets with desired characteristics [90].

However, it's important to note that while the cascaded centrifugation method offers enhanced purification capabilities, careful consideration must be given to the centrifugation conditions to prevent damage to the nanosheets. Balancing the centrifugation force and duration is crucial to avoid overcompaction or deformation of the nanosheets, which could compromise their structural integrity and performance. Therefore, careful optimization and control of the centrifugation process are essential to ensure the successful implementation of the cascaded centrifugation method for nanosheets purification [91], Figure2.1 shows starting from powder form sample, the process of ultrasonication followed by centrifugation and the dispersion after sonication.

In this thesis post-sonication, the dispersion underwent centrifugation (Megafuge^{TM} 16 Centrifuge, Thermo Scientific^{TM}, Waltham, MA, USA, equipped with a rotating angle rotor) at room temperature, with the sediment containing unexfoliated material being discarded. Subsequently, the supernatant underwent another centrifugation steps, and the sediment was discarded in the final step. The supernatant was then stored at 4 °C for subsequent use.

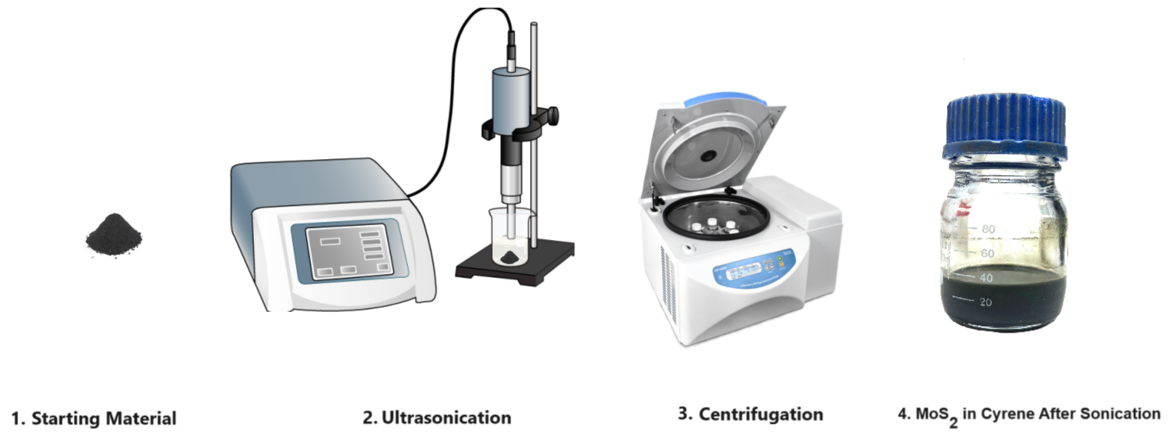

1. Starting Material
2. Ultrasonication
3. Centrifugation
4. MoS_2 in Cyrene After Sonication

Figure 2.1: Process of exfoliation through ultrasonication and centrifugation steps.

2.4 Characterization Techniques

The synthesized TMDs nanosheets undergo comprehensive characterization to understand their structural, optical, and morphological properties.

2.4.1 UV-Visible Spectroscopy

UV-Visible (UV-Vis) spectroscopy is a widely used technique to investigate the optical properties of materials. It measures a substance's interaction with light in the ultraviolet (UV) and visible regions of the electromagnetic spectrum. When a molecule absorbs UV-Vis light, its electrons can be excited from a lower energy ground state to a higher energy excited state. The wavelengths of light absorbed correlate to specific energy transitions within the molecule. By analyzing the spectrum of absorbed and transmitted light, UV-Vis spectroscopy offers insights into the electronic structure and, indirectly, the composition of materials. In the world of nanoscience, UV-Vis spectroscopy has emerged as an indispensable tool for characterizing nanosheets produced via liquid-phase exfoliation. It can confirm the exfoliation of the nanosheets, which often exhibit characteristic absorption peaks in the UV-Vis spectrum that differ from their bulk counterparts. The appearance of these peaks confirms the successful exfoliation of the bulk material into nanosheets. For example, in a paper on the liquid-phase exfoliation of MoS_2, the distinct excitonic peaks observed in the UV-Vis spectrum served as clear evidence of nanosheets formation [92]. It can also estimate nanosheets' size and thickness, and the position and intensity of absorption peaks in the UV-Vis spectra of nanosheets can be correlated to their size and thickness. As nanosheets become thinner, their absorption peaks often shift towards shorter wavelengths (blue shift) due to quantum confinement effects [93]. Thus, analyzing spectral shifts provides a means for indirectly estimating nanosheets dimensions. It can also give information about the concentration by using the Beer-Lambert Law, which relates the absorbance of a sample to its concentration. By using standards of known concentration, UV-Vis spectroscopy offers a way to determine the approximate concentration of nanosheets in a suspension [94].

The Beer-Lambert Law, expressed as $A = \epsilon \cdot c \cdot l$, relates absorbance ($A$) to the molar absorptivity coefficient (ϵ), concentration (c), and path length (l) of the cuvette. Absorbance, a unitless quantity, indicates the extent of light absorption by the material.

The molar absorptivity coefficient (ϵ), a material-specific constant, represents the ability of the nanosheets to absorb light at a particular wavelength and is measured in L mol^{-1} cm^{-1}. To determine ϵ, one typically measures absorbance (A) using a standard solution of the same nanosheets material with a known concentration. The calculation for ϵ involves dividing A by the product of concentration (c) and path length (l):

$$\epsilon = \frac{A}{c \cdot l} \tag{2.1}$$

In cases where a standard solution is unavailable, literature values for ϵ may be utilized, albeit with potentially reduced accuracy. The subsequent step involves calculating nanosheet concentration (c) in the suspension. This calculation expressed as $c = \frac{A}{\epsilon \cdot l}$, relies on the absorbance value and the molar absorptivity coefficient.

By carefully executing these steps and employing an accurate value for ϵ, the concentration of 2D nanosheets within the suspension can be effectively estimated using UV-Vis spectroscopy.

UV-vis characterization can also give a glimpse into the dispersion stability, nanosheets dispersions tend to aggregate over time, which affects their optical properties. By monitoring UV-Vis spectra regularly, changes in peak positions or intensities can point towards potential agglomeration or sedimentation, revealing information about the stability of the nanosheets dispersion [91], Figure 2.2 shows a schematic representation of UV-vis extinction spectroscopy.

The UV–Vis spectroscopy measurements were performed using a Jasco-700 UV–Vis spectrophotometer, Italy, with a 1 cm thick quartz cuvette and a spectral range of 200–800 nm to determine the exfoliated MoS_2/WS_2 absorption spectra.

2.4.2 Raman Spectroscopy

Raman spectroscopy is a vibrational spectroscopic technique based on the inelastic scattering of light. When a laser beam interacts with a molecule, it can cause the molecule's bonds to vibrate. A small portion of the scattered light undergoes a shift in energy (frequency) that corresponds to these vibrational modes. By measuring this Raman shift, we gain a characteristic "fingerprint" that reveals details about a material's chemical structure, bonding, and crystal lattice. Raman spectroscopy is a powerful tool for investigating nanosheets produced by liquid-phase exfoliation. It provides several key insights. It confirms the successful exfoliation of the nanosheets, Raman spectra of nanosheets often differ significantly from those of their bulk counterparts. New Raman peaks may emerge, or existing peaks might shift or change in intensity due to reduced dimension-

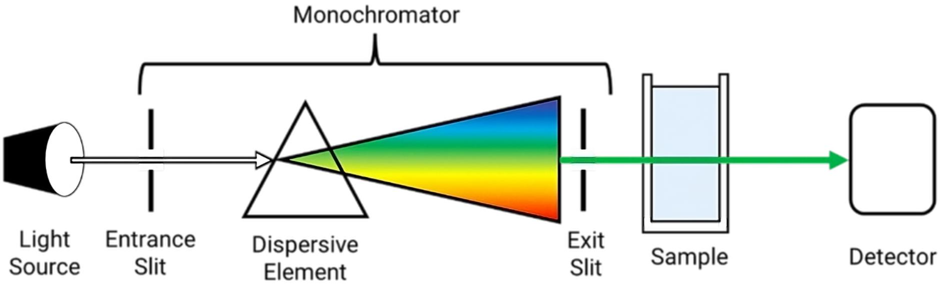

(a)

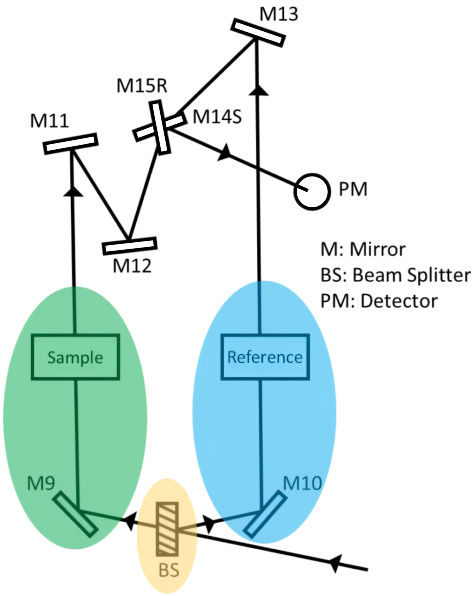

(b)

Figure 2.2: Diagrams illustrating UV-visible extinction spectroscopy, adapted from [95] (a) A basic block diagram of the elements in a single beam UV-Visible spectrometer and (b) Double beam instrument schematic. The beam splitter is highlighted in yellow, the reference beam in blue, and the sample beam is highlighted in green

ality. These spectral changes signify the successful exfoliation of bulk material into thin nanosheets [96]. Raman spectroscopy can also differentiate between various nanosheets types. For instance, graphene, MoS_2, and other two-dimensional (2D) materials exhibit unique Raman signatures that allow for unambiguous identification [97]. The Raman spectra of nanosheets are also sensitive to their crystalline quality and the presence of defects. Peak broadening and intensity changes can reveal information about crystal domain size, strain, and the nature of defects within the nanosheets [98]. In layered materials like graphene or MoS_2, the positions of certain Raman peaks shift systematically with the number of layers. This dependence allows for a non-destructive estimation of nanosheets thickness [99]. One of the most remarkable applications of Raman spectroscopy lies in its ability to estimate the number of layers in transition metal dichalcogenides (TMDs) like MoS_2, WS_2, and others. In these layered materials, certain Raman modes exhibit characteristic changes in frequency (peak position) and intensity as the number of layers varies [99].

The Raman spectrum of MoS_2 exhibits characteristic bands, denoted as E_{2g} and A_{1g}, corresponding to the in-plane and out-of-plane vibrational modes, respectively. In bulk MoS_2, these bands usually at approximately 380 cm^{-1} for E_{2g} and 403 cm^{-1} for A_{1g} . After MoS_2 exfoliation, such as in the formation of the nanosheets, the Raman features of the bulk material are modified. Specifically, there is an increase in the frequency of the E_{2g} band and a corresponding decrease in the frequency of the A_{1g} band [99]. This frequency shift ($\Delta\nu$) can be defined as:

$$\Delta\nu = \nu_{E_{2g}} - \nu_{A_{1g}} \tag{2.2}$$

where $\nu_{E_{2g}}$ and $\nu_{A_{1g}}$ represent the frequencies of the E_{2g} and A_{1g} bands, respectively, in the nanostructured MoS_2. This shift in frequency provides a means to identify the number of layers in the MoS_2 nanoflakes [100].

In WS_2, similar to MoS_2, Raman spectroscopy can also be used to determine the number of layers in the material. The characteristic Raman bands for WS_2 include the E_{2g} and A_{1g} modes, corresponding to in-plane and out-of-plane vibrational modes, respectively [101], Figure 2.3 shows a schematic representation of energy levels utilized in Raman spectroscopy.

In this thesis, measurements of Raman spectra were conducted using the commercial WiTec Alpha 300 confocal micro-Raman system. This system is composed of an inverted confocal Raman microscope and an atomic force microscope (AFM) placed on top of the inverted confocal microscope. This latter is equipped with a 532 nm probe generated with a frequency-doubled Nd-YAG laser and an 1800 grove/mm grating, assuring a spectral resolution of ∼1.5 cm−1.

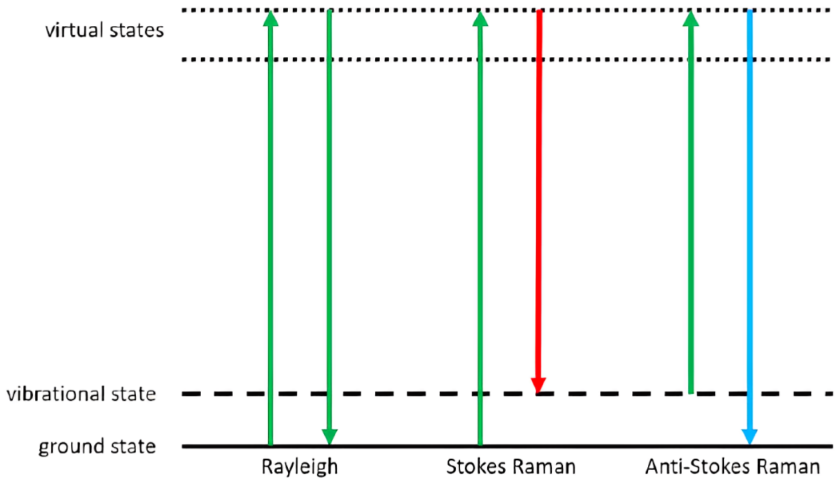

Figure 2.3: Diagram showing the energy levels utilized in Raman spectroscopy, adapted from [102]

2.4.3 Atomic Force Microscopy (AFM)

Atomic Force Microscopy (AFM) is a scanning probe microscopy type that creates ultra-high-resolution surface images. Unlike traditional light microscopy, AFM doesn't rely on lenses or light beams. Instead, it uses a tiny, sharp tip mounted on a cantilever to scan a sample's surface physically. The cantilever deflects as the tip interacts with the surface due to forces like van der Waals interactions and electrostatic forces. A laser system detects these deflections, generating a detailed topographic map of the surface with resolutions down to the nanometer scale. AFM is an indispensable tool in nanosheets characterization, offering numerous insights: in the surface topography and thickness measurement, AFM directly visualizes the surface morphology of nanosheets deposited on a substrate. This allows for highly precise measurements of nanosheets thickness, revealing whether the nanosheets are single-layer, few-layer, or multilayer [103]. Also, it can determine the lateral size of the nanosheets; AFM scans provide images from which the lateral dimensions (length and width) of nanosheets can be accurately determined [104]. AFM can quantify the surface roughness of nanosheets, which is often correlated with their defect density and functional properties. AFM can assess the quality of exfoliated nanosheets, and the acquired images reveal crucial information about the degree of exfoliation. It can show whether the nanosheets are well-separated or tend to form aggregates. This information is essential for evaluating the effectiveness of liquid-phase exfoliation processes [91]. It can also help in functionalization studies, by using special AFM modes with functionalized tips, we can probe interactions between nanosheets and other molecules. This enables the study of nanosheets surface functionalization and its effect on properties [105], Figure 2.4 shows a schematic representation of atomic force microscopy.

AFM analysis was performed using the same device used in Raman analysis in intermittent contact mode to avoid the perturbation of flakes' adhesion to the substrate. Nanoflake suspensions were drop-cast on glass coverslips and stored for 48 h at room

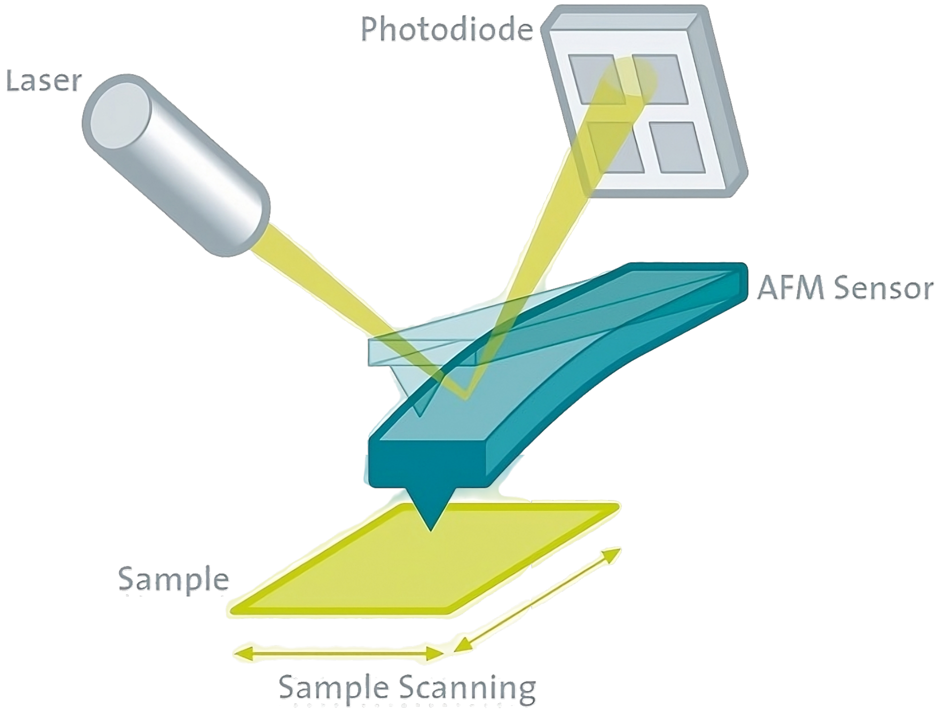

Figure 2.4: Diagram representing atomic force microscopy, adapted from [106]

temperature to allow complete solvent evaporation. Measurements were performed using a 100 infinite-corrected objective, which provided in-plane and axial resolutions (PSF-HWHM) of ~0.3 and 1 μm, respectively.

2.4.4 Zeta Potential and Dynamic Light Scattering (DLS)

Zeta Potential measures the overall surface charge of a particle or nanosheets suspended in a liquid medium. This surface charge arises due to the presence of ions on the material's surface and its interaction with the surrounding solvent. A high zeta potential (either strongly positive or strongly negative) generally indicates good colloidal stability, as the electrostatic repulsion between charged particles prevents them from aggregating. Conversely, a low zeta potential suggests a tendency for particles or nanosheets to clump together. In nanosheets characterization, zeta potential measurements provide insights into the stability of nanosheets dispersions and can help evaluate whether the surface of the nanosheets has been successfully functionalized to change its charge properties. A high magnitude zeta potential, whether positive or negative, indicates good dispersion stability due to electrostatic repulsion. For example, in a study on graphene oxide (GO) nanosheets, a highly negative zeta potential of around -50 mV suggested the successful production of a stable aqueous GO dispersion [107]. Also, changes in zeta potential can signal surface modification of nanosheets. In a paper investigating the functionalization of MoS_2 nanosheets, a shift in zeta potential from negative to positive after treatment with a cationic surfactant confirmed the surface modification [108]

Dynamic Light Scattering (DLS) is a technique used to determine the size distribution of particles and nanosheets in suspension. It works by illuminating a sample with a laser and analyzing the fluctuations in scattered light intensity. Smaller particles move faster in solution (Brownian motion), leading to faster fluctuations in the scattered light. By analyzing these fluctuations, DLS can determine the hydrodynamic diameter of the particles or nanosheets – the effective size of the particle plus its surrounding layer of solvent and ions. In the context of nanosheets, DLS is valuable for monitoring the size distribution of the produced nanosheets, checking for the presence of large aggregates, and assessing how factors like sonication time or the addition of dispersants affect the size of the nanosheets in dispersion. DLS offers insight into the average size (hydrodynamic diameter) of nanosheets in dispersion and reveals the size distribution's breadth. For example a study focusing on boron nitride (BN) nanosheets production found a DLS-measured average size of around 200 nm, indicating successful exfoliation [109]. DLS is also sensitive to the formation of aggregates, a common issue in nanosheets dispersions. The observation of markedly increased sizes within the Dynamic Light Scattering (DLS) distribution is a notable indicator of potential aggregation phenomena. Some research used DLS to track how factors like pH or stabilizing agents' presence affect nanosheets aggregation tendency [91], Figures 2.5 (a) and (b) show a schematic representation of zeta-potential and DLS, respectively.

In this thesis, the ζ-potential and DLS measurements were performed using a Malvern Zetasizer Nano system, United Kingdom (UK), with a 633 nm He-Ne laser as the excitation source. The ζ-potential measurements were performed to determine the charge on the surface of the exfoliated NMs. DLS data reported is taken as the average of three measurements ($n = 3$) measured at 25 °C in disposable folded capillary cells (DTS1070) in water dispersants. The samples were injected in folded capillary cells, and the electrophoretic mobility (μ) value was measured using a combination of electrophoresis and laser Doppler velocimetry techniques. All the measurements were carried out at 25 °C.

2.4.5 Scanning Electron Microscopy (SEM)

SEM is a powerful imaging technique that produces high-resolution images by scanning a sample's surface with a focused beam of electrons. When the electrons interact with the sample, they generate various signals, including secondary electrons, which reveal detailed information about the surface topography, and backscattered electrons, which provide some insight into the material's composition. SEM plays a crucial role in nanosheets characterizations for several reasons. It can help confirm nanosheets formation by providing direct visual evidence of successful exfoliation. Nanosheets have distinctive morphologies that are readily distinguishable from their bulk counterparts in SEM images. For example, the successful exfoliation of graphite into graphene nanosheets can be confirmed by the appearance of thin, sheet-like structures in SEM [111]. High-resolution SEM images can also reveal the lateral dimensions (length and width) of individual nanosheets, along with details of their shape (e.g., regular, jagged edges)[48]. SEM also unveils the surface texture and presence of wrinkles, folds, or defects on the nanosheets. This information relates to the quality of the exfoliation process and the properties of the nanosheets. SEM is not as precise as AFM for the thickness estimation, but it can provide thickness

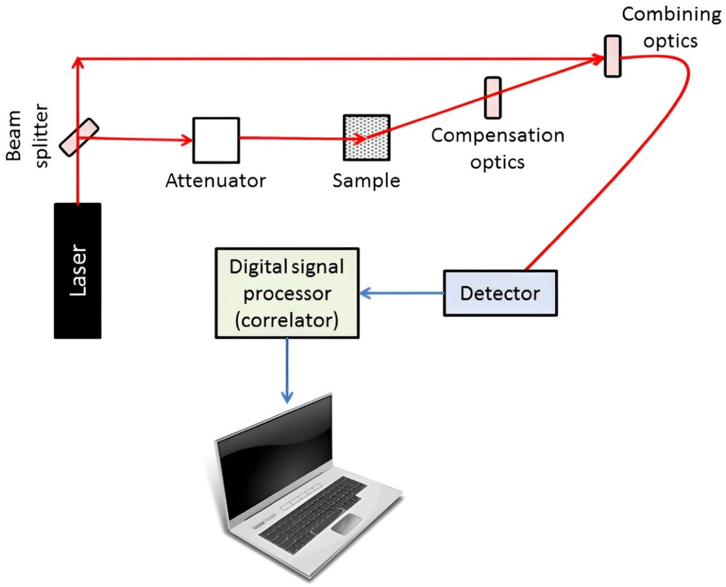

(a) Zeta-potential

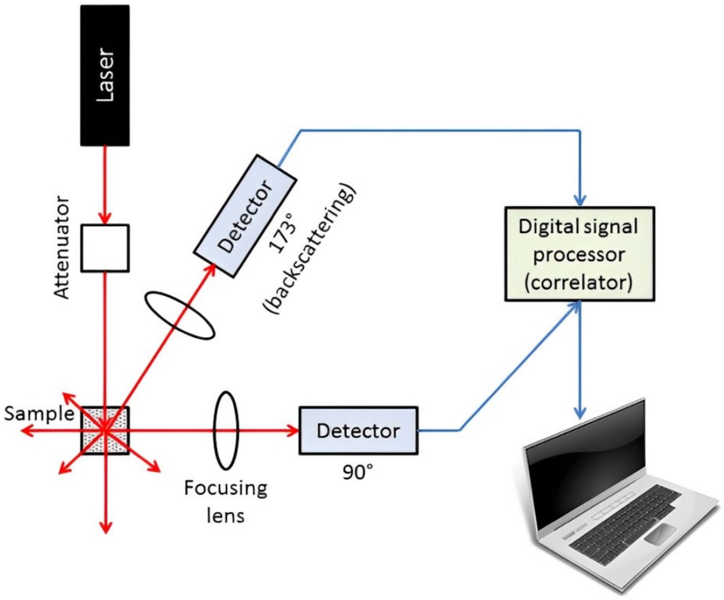

(b) DLS

Figure 2.5: Diagram outlining the principles of (a) Zeta-potential and (b) DLS, adapted from [110]

estimates when nanosheets are deposited on their edge. By utilizing cross-sectional SEM, it's possible to visualize the stacking of individual sheets directly[112], Figure 2.6 shows a schematic representation of scanning electron microscopy.

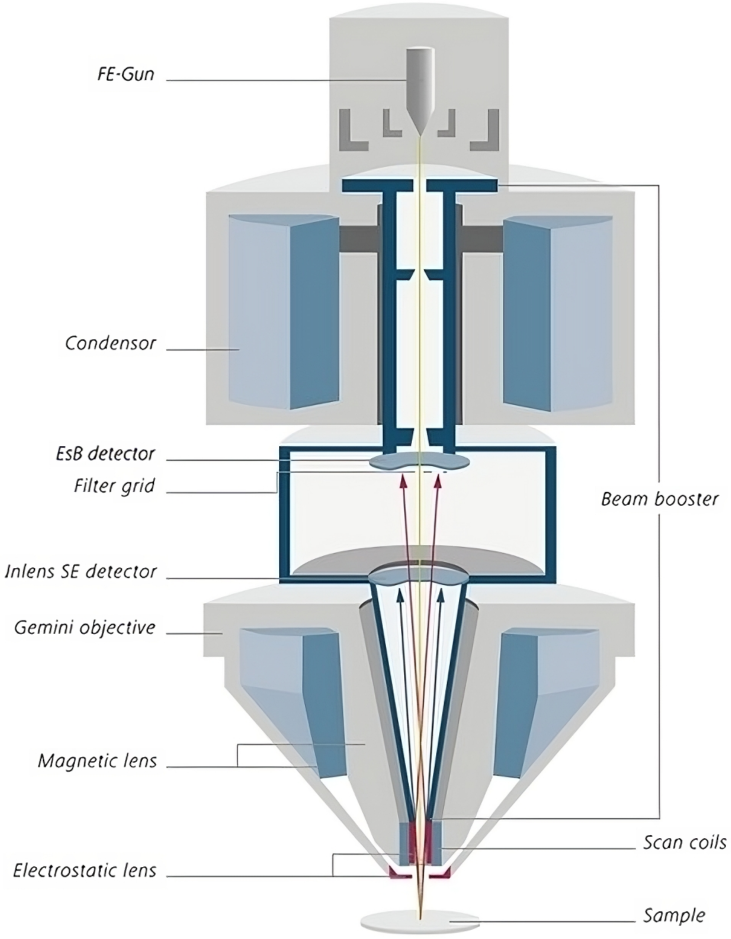

Figure 2.6: Diagram outlining the principles of scanning electron microscopy, adapted from [113]

In this thesis, for morphological analysis of the samples, we employed a Zeiss Merlin VP Compact Scanning Electron Microscope (SEM) located at the DiSTAR laboratory, Universita degli Studi di Napoli Federico II. This field-emission SEM was equipped with a Gemini II camera and operated using the FeSEM: SmartSem software controller.

The SEM system comprised three secondary electron detectors (SE2 for classic detection, VPSE for variable pressure, and InlensDuo for low voltage) and two backscattered electron detectors (AsB and InlensDuo). Additionally, the SEM was equipped with a charge compensation system and Oxford Instruments Microanalysis systems (EDS X-max 50 and WDS Wave).

Data processing was performed using two software packages: INCA version 4.081 (Oxford Instruments, 2006) for both EDS (Energy-Dispersive X-ray Spectroscopy) and WDS (Wavelength-Dispersive X-ray Spectroscopy), and Aztec for EDS analysis. SmartSem software was specifically used for image data acquisition from the SEM.

Before analysis, the samples were deposited onto glass supports with smooth and irregular surfaces using a drop-casting method. Subsequently, the samples were metalized with a thin layer of gold using a sputter coater.

2.4.6 X-ray Photoelectron Spectroscopy (XPS)

XPS is a powerful surface-sensitive technique that analyzes materials' elemental composition and chemical state. It works by bombarding a sample with X-rays, which cause electrons to be ejected from the atoms within the top few nanometers of the material. By measuring the kinetic energy of these photoelectrons, XPS provides a "fingerprint" of the elements present and their chemical bonding environment. Importance of XPS for Nanosheets XPS is an invaluable tool for nanosheets research, offering several key insights. XPS provides a quantitative analysis of the elements present on the surface of nanosheets. This helps verify the purity of the material and detects any contaminants or residues from the synthesis process [93], Figure 2.7 shows a schematic representation of X-ray photoelectron spectroscopy.

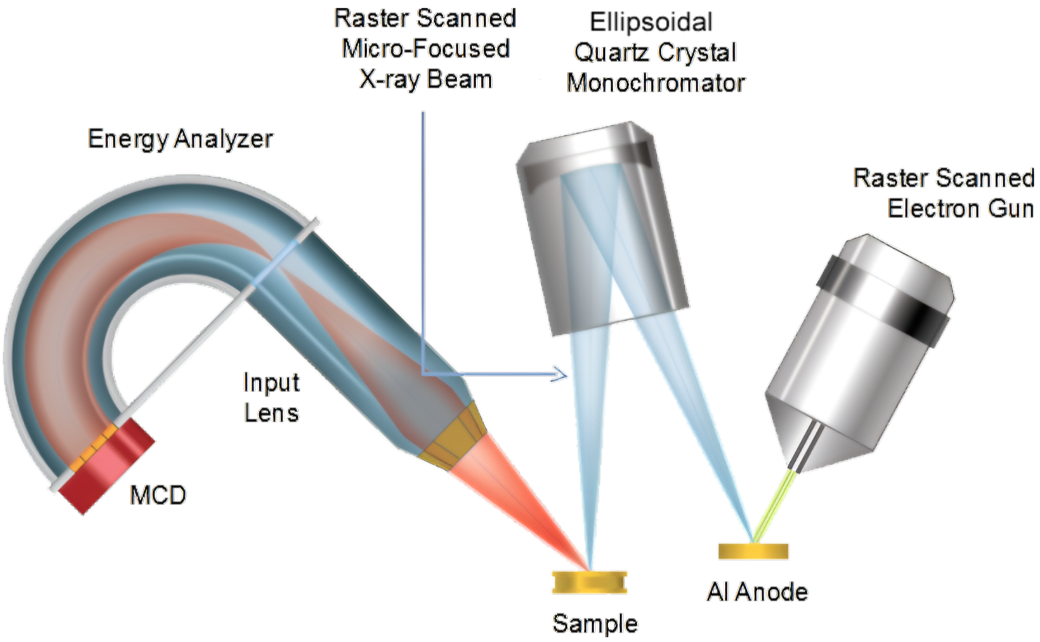

Figure 2.7: Diagram illustrating X-ray photoelectron spectroscopy, adapted from[114]

XPS can also help in chemical state and bonding; small shifts in the photoelectrons' binding energy reveal the elements' oxidation state and the nature of chemical bonds within the nanosheets. This information is vital for understanding nanosheets reactivity and how they might interact with other molecules [115]. XPS can also confirm the successful surface modification of nanosheets by detecting changes in elemental composition and identifying new chemical bonds formed after functionalization [111]. In some cases, XPS spectral analysis can provide insights into the nature and density of defects present in nanosheets, which strongly influence their properties [116].

In this thesis, X-ray photoelectron spectra (XPS) were acquired using a Versa Probe II XPS instrument (PHI, Chanassen, US) in large-area analysis mode. The analysis employed a monochromated Al Kα X-ray source (100 μm spot size) with a power of 100 W. The source was positioned normal to the sample surface and rastered over an area of 1400 μm x 300 μm. The analyzer was set at a 45° take-off angle relative to the sample surface.

Survey spectra were collected with an acquisition time of at least 20 minutes at a high pass energy of 187 eV. High-resolution spectra were subsequently acquired for elements of interest at pass energy of 11.7 eV. All XPS data were analyzed using Multipack software (PHI, Chanassen, US). Peak positions were referenced to the adventitious carbon (C 1s) peak at a binding energy of 284.8 eV.

Samples were prepared by drop-casting a suspension of MoS_2 nanoparticles in an aqueous medium onto a flat silicon substrate. The solvent was then evaporated in a vacuum chamber. XPS also analyzed the suspending aqueous medium to identify potential contaminants.

2.5 DLVO Theory

The Derjaguin-Landau-Verwey-Overbeek (DLVO) theory is a cornerstone of colloid science, providing a fundamental framework for understanding the interplay of forces governing the stability of colloidal dispersions. Developed collaboratively in the 1940s, the theory builds upon the independent contributions of Derjaguin and Landau, later refined by Verwey and Overbeek. This collaborative effort established a powerful tool for elucidating the intricate forces governing the behavior of charged particles in a liquid environment.

The DLVO theory integrates principles from physics and chemistry to explain the interplay between van der Waals attractive forces and electrostatic repulsive forces, thereby revealing the fundamental mechanisms that govern colloidal stability. This approach provides a robust framework for understanding the delicate balance between attraction and repulsion that determines the behavior of colloidal dispersions.

The foundational contributions of Derjaguin, Landau, Verwey, and Overbeek in developing the DLVO theory have revolutionized our understanding of colloidal phenomena. This theory's principles transcend disciplinary boundaries, impacting advancements in materials science, pharmaceuticals, and environmental engineering, by informing the manipulation and engineering of colloidal systems for diverse applications.

In the DLVO framework, the total interaction energy between nanosheets and bacteria arises from the summation of van der Waals and electrostatic forces. This energy can be expressed mathematically as:

$$V^{\text{tot}} = V^{EL} + V^{vw}, \tag{2.3}$$

Van der Waals forces V^{vw} arise from the fluctuations in electron distribution within molecules, resulting in temporary dipole moments and induced dipole interactions between adjacent particles. These forces contribute to the attraction between nanosheets and bacteria, particularly when they are in close proximity. The magnitude of van der Waals forces depends on factors such as the distance between interacting surfaces and their respective surface properties. And it is given by:

$$V^{vw} = -\frac{Aa_1a_2}{6d(a_1 + a_2)} \tag{2.4}$$

where A is the Hamaker constant that considers the van der Waals body-body interaction coupling.

Electrostatic forces V^{EL} stem from the presence of charged species on the surfaces of nanosheets and bacteria. These charges can be either positive or negative, leading to repulsive or attractive interactions between particles, depending on their relative charge and distance. The DLVO theory quantifies electrostatic interactions using the Poisson-Boltzmann equation, which accounts for the distribution of ions in the solution and the resulting electrostatic potential around charged particles. And it is given by:

$$\begin{aligned} V^{EL} = & \frac{\pi\epsilon a_1 a_2\left(\zeta_1^2 + \zeta_2^2\right)}{(a_1 + a_2)} \\ & \left\{\frac{2\zeta_1\zeta_2}{\zeta_1^2 + \zeta_2^2}\ln\left[\frac{1 + \exp(-kd)}{1 - \exp(-kd)}\right] + \ln[1 - \exp(-2kd)]\right\} \end{aligned} \tag{2.5}$$

where a_1 and a_2 are the average radii of the bacterium and nanoflakes, respectively; ζ_1 and ζ_2 are for zeta-potential of the bacterium and nanoflakes, respectively; d is the separation distance between the nanoflakes and the bacteria; ϵ is the permittivity of the solution; and k is a constant which is the inverse of Debye-H$\ddot{u}$ckel length λ_D.

2.6 Monte Carlo Simulation

Monte Carlo simulation is a powerful computational technique widely used in various scientific fields to simulate complex systems through random sampling. In the context of our study, we employed Monte Carlo simulation to model the transport of electrons and photons, crucial processes in understanding the interaction of radiation with matter.

The specific Monte Carlo code utilized in our calculations was derived from the renowned PENELOPE (PENetration and Energy Loss of Positrons and Electrons) code system.

Initially introduced by F. Salvat and colleagues, the PENELOPE code system represents a comprehensive tool for simulating the transport of electrons and photons in matter, particularly in low-energy regimes. The foundation of the PENELOPE code system is rooted in the seminal works by Salvat et al. The foundational paper by Salvat et al. in 2001 provides a comprehensive overview of the PENELOPE code system, detailing its capabilities in highly precise simulating electron and photon transport. Additionally, experimental benchmarks of the PENELOPE Monte Carlo code were conducted by Sempau et al. in 2003, further validating its accuracy and efficacy in simulating radiation transport phenomena [80, 81].

In our study, the Monte Carlo simulations based on the PENELOPE code system enabled us to investigate intricate interactions between radiation and matter, providing insights into various phenomena crucial to our research objectives. By leveraging the robust capabilities of Monte Carlo simulation and the established accuracy of the PENELOPE code system, we were able to model and analyze complex radiation transport processes with confidence and precision.

2.6.1 Monte Carlo Simulation Algorithm

- The Monte Carlo simulation algorithm used in our study follows a standard procedure for simulating radiation transport through matter. Key steps include:
- Generation of random initial particle states (position, energy, direction).
- Propagation of particles through the material, accounting for interactions based on the calculated cross-section.
- Sampling of interaction processes using probability distributions derived from the cross-section.
- Iterative advancement of particles until specified criteria (e.g., maximum distance traveled) are met.

These steps are repeated for many particles to represent the behavior of radiation within the material statistically.

Chapter 3 Intro: Modeling MoS_2 nanosheets-Bacteria Interactions

This chapter is based on the following published paper:

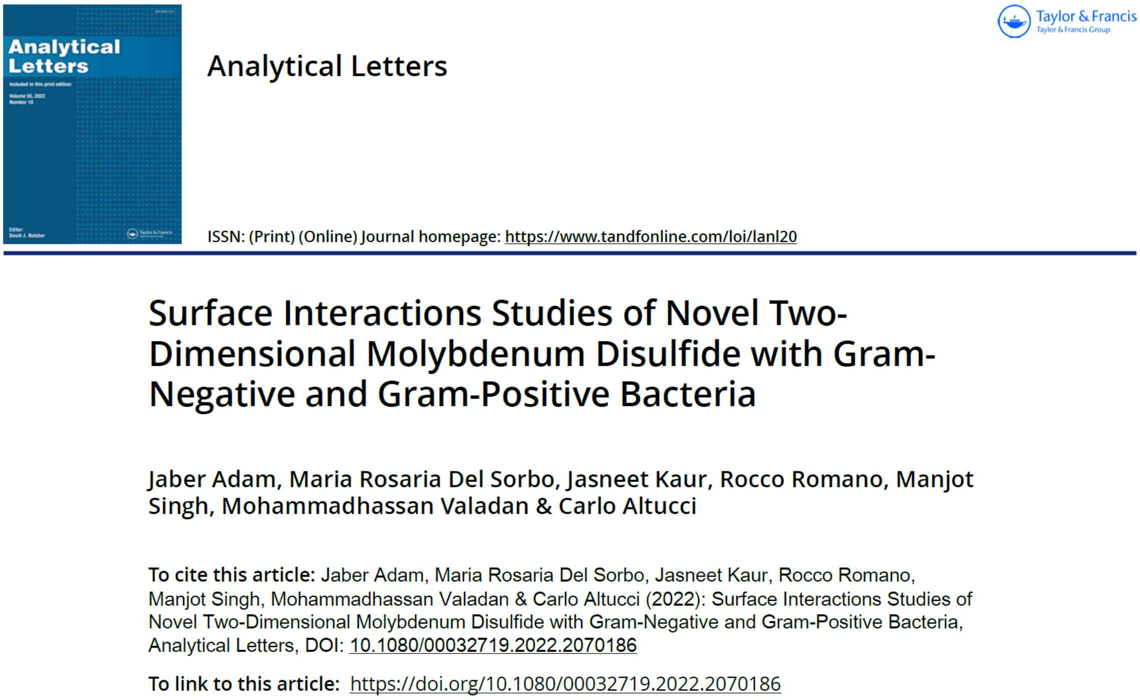

Analytical Letters

ISSN: (Print) (Online) Journal homepage: https://www.tandfonline.com/loi/lanl20

Surface Interactions Studies of Novel Two-Dimensional Molybdenum Disulfide with Gram-Negative and Gram-Positive Bacteria

Jaber Adam, Maria Rosaria Del Sorbo, Jasneet Kaur, Rocco Romano, Manjot Singh, Mohammadhassan Valadan & Carlo Altucci

To cite this article: Jaber Adam, Maria Rosaria Del Sorbo, Jasneet Kaur, Rocco Romano, Manjot Singh, Mohammadhassan Valadan & Carlo Altucci (2022): Surface Interactions Studies of Novel Two-Dimensional Molybdenum Disulfide with Gram-Negative and Gram-Positive Bacteria, Analytical Letters, DOI: 10.1080/00032719.2022.2070186

To link to this article: https://doi.org/10.1080/00032719.2022.2070186

This chapter introduces a theoretical framework, based on the extended DVLO model, for understanding the complex interactions between MoS_2 nanosheets and various bacterial strains in both water and cyrene solvents. These insights are crucial for developing MoS_2-based biomedical applications, such as antimicrobial coatings, by providing a way to predict nanosheets stability, potential adhesion, and even specificity towards specific types of bacteria.

Chapter 3

Surface Interactions Studies of Novel Two-dimensional Molybdenum Disulfide with Gram-Negative and Gram-Positive bacteria

3.1 Abstract

The interaction between two-dimensional nanoflakes and bacteria in water-based physiological liquids are a hot topic that unveils new types of phenomena and is fundamental to bioscience applications. In this work, we extend Derjaguin, Landau, Verwey, and Overbeek theory (DLVO theory) that describes the properties of nano-objects in solutions, to the case of two-dimensional nanoflakes interacting with bacteria cell membranes, both for Gram-positive and Gram-negative bacteria, acknowledging that their cell walls are primarily composed of peptidoglycans and lipopolysaccharides, respectively. We have studied the role of the bacterial shape, membrane potential, and two-dimensional nanomaterials nature showing the interplay of these parameters in determining whether the interactions are attractive or repulsive and whether electrostatic or van der Waals forces are dominant. We calculated the interaction distances at equilibrium for different bacterial species and hydrophobic nanomaterials such as MoS_2 in two environmentally friendly solvents, water and cyrene.

3.2 Introduction

From a general point of view, prokaryotic microorganisms are essential for humans and ecosystems. Specifically, bacteria have been studied in several contexts in literature because they can strongly interact with humans and the surrounding environment. For instance, *E. coli* bacteria caused a gastroenteritis outbreak in Germany in 2011, and there were more than 3816 cases, resulted in 64 deaths [117]. In such a context, the interactions of bacteria with biological membranes play an important role and hence is a well-studied topic [118] because it is crucial to unveil the specific surface characteristics that influence this adhesion [119]. The attachment of bacteria to surfaces can be affected by the surface characteristics of the bacteria (such as their surface charge) and the surface characteristics of the material [120].

The two-dimensional nanomaterials have become a focus of research in recent years because of their interesting physical and chemical properties and applications in many areas such as electronics and medical fields. The work on two-dimensional nanomaterials originates from the well-known and studied graphene. Its unique properties in terms of its electric and thermal conductivity [121];[122];[123] make it suitable for applications in medicine [124];[125] and optoelectronics [126]. Graphene and its applications triggered the search for other two-dimensional nanomaterials that led to the discovery of novel materials such as the transition metal dichalcogenides (TMDs) molybdenum disulfide (MoS_2) [127] and tungsten disulfide (WS_2) [128].

The unique properties of MoS_2, such as its thickness-dependent bandgap, large surface area, and easily functionalized surface sites [36], make it ideal for biosensing applications [35]. Zhu et al. used MoS_2 to detect DNA and small molecules [129], Our group took advantage of the photoluminescence properties of MoS_2 for biological applications related to ions [130], while other teams focused on applications of MoS_2 in the area of drug delivery [30];[131], biomedical imaging [132], and cancer treatment [133];[134];[135]. Among methods used for the production of the two-dimensional nanomaterials, one of the most widely used is liquid phase exfoliation (LPE) [136];[112] that involves sonication [47], shearing [92], or mixing of the two methods [137]. The solvent used in the process of exfoliation is one of the challenges to be addressed [91]. Organic solvents [52] used in the preparation have drawbacks such as high boiling point and toxicity. Therefore, the need for green and environmentally friendly solvents originates. In such context, water is the best solvent to produce two-dimensional nanomaterials [138]. Recently, cyrene appeared as a green solvent with excellent properties and good availability [85].

Interestingly, these nanomaterials interact with microorganisms, as titanium dioxide, (TiO2), zinc oxide (ZnO), and metal nanoparticles with bacteria [139]. For instance, [140] Syngouna and Chrysikopoulos (2017) demonstrated the inactivation onto bacteriophages by TiO2 nanoparticles and the influence of ambient light and quartz sand in this interaction [141];[142]. Gold nanoparticles adhere to bacteria may be used in biosensors and SERS [143];[144]. Inspired by studies directed to investigate the effect and interaction of two-dimensional nanomaterials with nanoparticles, in our previous work [145] we modeled the interaction of MoS_2 and graphene oxide with bacteria (*E. coli* and *S. aureus*) and viruses (Herpes simplex virus type-1, HSV-1) based on the Derjaguin–Landau–Verwey–Overbeek (DLVO) model that has been successfully used [146] to describe the interactions of graphene oxide nanoparticles with *Escherichia (E.) coli, Enterococcus (E.) faecalis, and Staphylococcus (S.) aureus* in water saturated porous media.

The flexibility of the DLVO model [147] and its friendly approach have been employed to describe quantitatively complicated interactions. Here we expand the investigation of the impact and interaction of MoS_2 two-dimensional nanomaterial to a vast range of bacteria, three Gram-positive (*Staphylococcus carnosus, Staphylococcus aureus,and Bacillus subtilis*), and three Gram-negative (*Stenotrophomonas maltophilia, Neisseria subflava, and Escherichia coli*) bacteria using the DLVO model Figure 3.1 presents the actual shapes of the bacteria as captured in SEM images [144]; [148]. It is important to acknowledge that bacteria possess a cell wall with varying compositions depending on their classification. Gram-positive bacteria have cell walls primarily composed of peptidoglycans, while Gram-negative bacteria have an outer membrane rich in lipopolysaccharides. These structural differences play a crucial role in the interaction between MoS_2 and bacterial cells. This extension of the model is certainly novel in addressing in a quantitative way the interactions of MoS_2 two-dimensional nanomaterials with a plethora of different microorganisms in solution in an environment closely resembling living matter. This extension is performed in a general context, so to treat with the same model and within a unified scenario interactions of nanomaterials with bacteria, with viruses and possibly even cells. Our model extension, in fact, leads to results that depend in a controlled and known way on the size and the shape of the considered microorganisms. In addition, the results depend upon intrinsic parameters that characterize the microorganism, such as its surface charge and Hamaker constant [149]. We also consider two-dimensional nanomaterials and not nanoparticles, with the chance to consider a nano-object having specific shapes with unbalanced aspect ratio between thickness and lateral size.

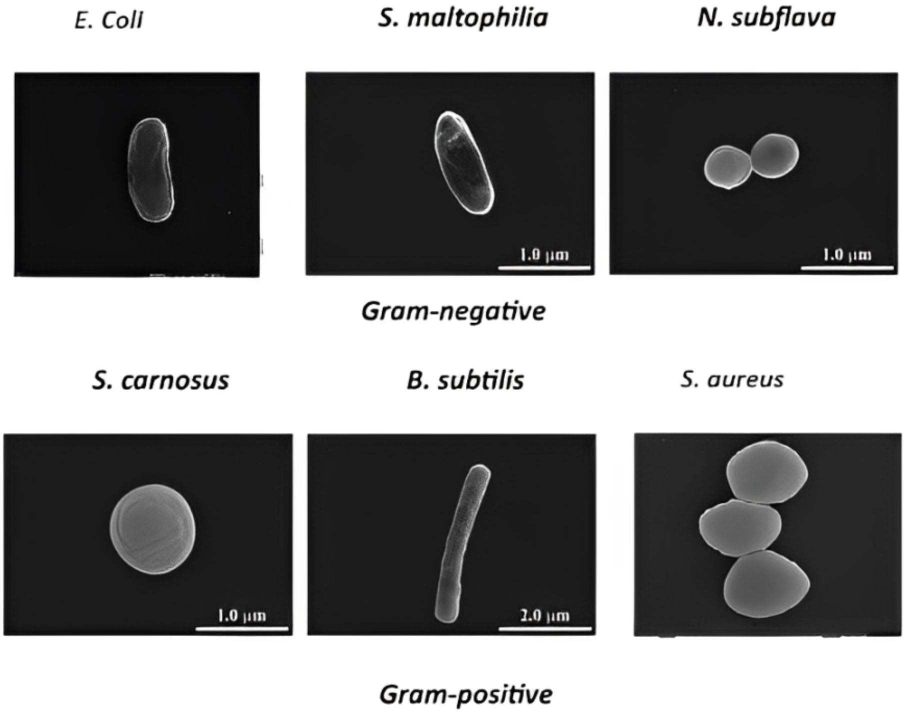

Figure 3.1: SEM images showing the actual shapes and surface structures of six bacterial species, including three Gram-positive and three Gram-negative strains.

The novel developed model is useful for bio-nanoscience applications because it is able to easily and quantitatively describe the interactions of nanomaterials with many microorganisms. In fact, the cases and experiments in the latest studies involve the interaction of nanomaterials a plethora of microorganisms at the same time in a context live or close to resemble the complexity of a real environment [147]. Additionally, we consider the effect of two green solvents, water and cyrene. Two interactions are considered in our model; Coulomb and van der Waals forces. As interesting results we stress the correlation between low charges surface density and the prevalence of the attractive van der Waals interaction in the singular case of *E. coli*. Hence, this paper then open a possible perspective in developing antibacterial action on distinct pathogens.

	Zeta-potential of the bacteria ζ_1(mV)	Radius of the bacteria a_1(nm)
B. subtilis (G+)	-41	520
S. carnosus (G+)	-37	440
S. aureus (G+)	-37.1	360
N. subflava (G-)	-30	400
S. maltophilia (G-)	-26	460
E. coli (G-)	-12.7	630

Table 3.1: Summary of bacteria characteristics (radius a_1, zeta-potential ζ_1).

3.3 Material and methods

The DLVO theory, which considers the attractive van der Waals and the repulsive electrostatic forces [150], is employed to compute the surface interaction energy between the bacteria and the nanoflakes. We used six bacteria strains *(Staphylococcus carnosus, Stenotrophomonas maltophilia, Neisseria subflava, Bacillus subtilis, Staphylococcus aureus and Escherichia coli*), with distinct characteristics such as their surface charges zeta-potential (ζ), shape, and average radius (a_1), the radii values are assumed to be as an average radius of a model spherical cell corresponding to the actual cylindrical/spherical bacterial shapes with the same volume (Table 3.1) [144]. MoS_2 nanoflakes are prepared in cyrene and water. The total interaction energy V^{tot} is described by:

$$V^{\text{tot}} = V^{EL} + V^{vw}, \tag{3.1}$$

as the sum of the electrostatic repulsive V^{EL} and attractive London-van der Waals V^{vw}. The interactions V^{EL} are given by:

$$\begin{aligned} V^{EL} = & \frac{\pi\epsilon a_1 a_2 \left(\zeta_1^2+\zeta_2^2\right)}{\left(a_1+a_2\right)} \\ & \left\{\frac{2\zeta_1\zeta_2}{\zeta_1^2+\zeta_2^2}\ln\left[\frac{1+\exp(-kd)}{1-\exp(-kd)}\right]+\ln[1-\exp(-2kd)]\right\} \end{aligned} \tag{3.2}$$

where a_1 and a_2 are the average radii of the bacterium and nanoflakes, respectively; ζ_1 and ζ_2 are for zeta-potential of the bacterium and nanoflakes, respectively; d is the separation distance between the nanoflakes and the bacteria; ϵ is the permittivity of the solution; and k is a constant which is the inverse of Debye-H$\ddot{u}$ckel length λ_D defined by:

$$k = \frac{1}{\lambda_D} = \sqrt{\frac{2z^2e^2n}{\epsilon_r\epsilon_0K_BT}} \tag{3.3}$$

where T is the absolute temperature of the solution, z the charge of the ion, e is $1.6 \times 10^{-19}C$ the elemental charge, n is the ion density, ϵ_r is the solvent relative permittivity, ϵ_0 is 8.85×10^{-12} C^2/Jm^2 the vacuum permittivity, and K_B is the Boltzmann constant. The Debye–H$\ddot{u}$ckel length λ_D is ≈ 2 μm for water, and ≈ 0.4 μm for cyrene, calculated as in the literature using Equation 3.3 [147]. The van der Waals interaction energy is described by:

$$V^{vw} = -Aa_1a_2/6d\left(a_1 + a_2\right), \tag{3.4}$$

where A is the Hamaker constant that considers the van der Waals body-body interaction coupling. For two nanosized objects interacting into a dispersion, this parameter is defined by [149]:

$$A = \left(\sqrt{A_1} - \sqrt{A_d}\right)\left(\sqrt{A_2} - \sqrt{A_d}\right), \tag{3.5}$$

where A_1 and A_2 are the Hamaker constants for the bacterium and the nanoflakes, respectively, in the absence of the solvent. We consider $A_1 = 5.2 \times 10^{-20}$ for the bacteria strains [151] and $A_2 = 29.6 \times 10^{-20}$ for MoS$_2$ [152]. For the solvent Hamaker constant A_d we find $A_d = 3.7 \times 10^{-20}$ for water [147] and for cyrene $A_d = 2.84 \times 10^{-20}$ where A_d is calculated by [147]:

$$A_d = \frac{3}{4}kT\left(\frac{\varepsilon_1 - \varepsilon_2}{\varepsilon_1 + \varepsilon_2}\right)^2 + \frac{3h\nu_e}{16\sqrt{2}}\frac{\left(n_1^2 - n_2^2\right)^2}{\left(n_1^2 + n_2^2\right)^{3/2}}. \tag{3.6}$$

where ε_1 and $\varepsilon_2 = 1$ are dielectric constants and n1 and n2 = 1 are the the refractive indices of water and cyrene [153] and air, respectively, and ν_e is the main electronic absorption frequency of the solvent in the ultraviolet, typically 3×10^{15} s^{-1} [147].

Another parameter that plays a role is the so-called critical volume r^3_{crit} defined to be the volume around the bacteria at which the net interaction bacteria-nanoflakes force is essentially attractive. At large d, the electrostatic repulsive term prevails, resulting in a positive interaction energy, whereas at small d values, the overall interaction energy is negative due to the dominant attractive van der Waals force. Hence, we use d_0 to define r^3_{crit}, where d_0 is the d value where the overall interaction energy changes its sign. Thus V_{tot} (d=d_0) = 0 and hence [145]:

Solvent	**Permittivity** (ϵ_r)	**Refractive index** (n_1)	**Hamaker constant** ($A \times 10^{-20}$)	**Hamaker constant** ($A_d \times 10^{-20}$)	**Radius of** $\mathrm{MoS_2}$ (a_2, **nm**)
Water	85	1.33	1.26	3.7	130
Cyrene	3.4	1.47	2.24	2.8	250

Table 3.2: Summary of $\mathrm{MoS_2}$ nanoflakes and solvent characteristics: permittivity (ϵ_r), refractive index (n_1), Hamaker constants (A and A_d), and radius (a_2, nm) of the nanoflakes.

$$r_{\text{crit}}^3 = (d_0 + a_1)^3 - a_1^3. \tag{3.7}$$

Table 3.1 summarizes the main characteristics of the bacteria (radius, ζ-potential) [119]; [144]; [145]. In Table 3.2, we summarize the main parameters of the solvents water and cyrene, permittivity (ϵ_r), refractive index (n_1), Hamaker constants (A and A_d) and the average radius of $\mathrm{MoS_2}$ nanoflakes, produced in that solvent [145]; [154].

3.4 Results

3.4.1 Interaction energy of the bacteria and the nanoflakes

Our results show the relationship between the total interaction energy described by DLVO theory and spacing d (nm) between the bacteria membrane and $\mathrm{MoS_2}$ nanoflakes. The total interaction energies in water and cyrene as shown in Figure 3.2. Figure 3.3 compares the total interaction energy (solid line), van der Waals interaction V^{vw}(dotted line), and electrostatic interaction V^{EL} (dashed line) as a function of the separation distance d for water (blue) and cyrene (orange). The *E. coli* shows the minimum energy, with *B. subtilis* the highest, and the values of *S. aureus* and *S. carnosus* are similar (Table 3.3).

Here below we summarize the main findings:

- Water-based solvent always showed higher interaction energy for all bacteria compared to in cyrene.
- The Gram-positive bacteria showed higher interaction energies than the Gram-negative bacteria.
- There is a nearly direct proportionality between the interaction energy and the negative ζ-potential for all bacteria (Figure 3.4).
- Among the investigated bacteria, *E. coli* behaves in a singular manner and exhibits by far the smallest energy barrier to pass for a $\mathrm{MoS_2}$ nanoflakes to approach its

membrane, both in water and cyrene. It is also characterized by the largest d_0 value (Table 3.7), which implies a much larger volume surrounding the bacterium where the nanoflakes are attracted to the membrane and eventually impact the bacterium.

- Interestingly, the critical volume is much larger in cyrene than in water and much larger in both solvents for *E. coli* than for the other bacteria.

3.4.2 Electrostatic, Van Der Waals interaction

In order to characterize the interaction between the attractive van der Waals and repulsive electrostatic forces for all bacteria and solvents, three separation distances$d$(0.1, 1, and 100 nm) were selected. These values represent a short distance (0.1 nm), an intermediate d value (1 nm), and a long value (100 nm). The electrostatics, van der Waals, and total interaction energies for $d=$ 0.1 nm, $d=$ 1 nm, and $d=$ 100 nm are summarized in Tables 3.4-3.6 for both solvents. The electrostatic interaction V^{EL} term is stronger in cyrene compared to V^{vw}. Additionally, in Table 3.7, the values of d_0 are reported for each case.

Bacteria	**Zeta-potential of the bacteria (ζ_1, mV)**	**Radius of the bacteria (a_1, nm)**	**Bacteria-MoS$_2$ Separation in Water (d_{water}, nm)**	**Bacteria-MoS$_2$ Separation in Cyrene (d_{cyrene}, nm)**	**Critical Volume for Water (r^3_{critw}, nm^3)**	**Critical Volume for Cyrene (r^3_{crit}, nm^3)**
B. subtilis (G+)	-41	520	120	98.98	3.44×10^5	1.14×10^7
S. carnosus (G+)	-37	440	68	97.98	2.20×10^5	8.49×10^6
S. aureus (G+)	-37.1	360	69	97.98	1.48×10^5	5.71×10^6
N. subflava (G-)	-30	400	33	102.98	1.88×10^5	8.26×10^6
S. maltophilia (G-)	-26	460	43	11.98	2.98×10^5	1.28×10^7
E. coli (G-)	-12.7	630	629	238.98	3.40×10^7	8.86×10^7

Table 3.3: Summary of bacteria-MoS$_2$ separation (d, nm) corresponding to the maximum total interaction energy, critical volume for the two solvents used (r^3_{critw} for water, r^3_{crit} for cyrene), and basic characteristics of the bacteria (zeta-potential ζ_1 and radius a_1).

3.5 Discussion

Bacterial interactions with their environment mostly involve the cell wall biomolecules and nanomaterials. Hence, the surface chemistry of the bacterial cell wall has importance in governing and determining the nature of these interactions, given that two-dimensional materials have intriguing antimicrobial properties which plays a key role in utilizing these novel materials in a vast number of applications. In fact, two-dimensional MoS$_2$ nanoflakes, are semiconductors with interesting anti-microbial properties [155]; [156]; [157]; [79]. In the current study, we aimed at simulating in a general way using our DLVO-based model the interactions between nanoflakes and bacteria, also taking into account the role played by green solvents. Thus, the impact of pure water and cyrene (employed for MoS$_2$ exfoliation) is analyzed upon three Gram-positive and three Gram-negative bacterial strains, to understand the change in the total interaction energy between the bacteria and two-dimensional MoS$_2$ nanoflakes.

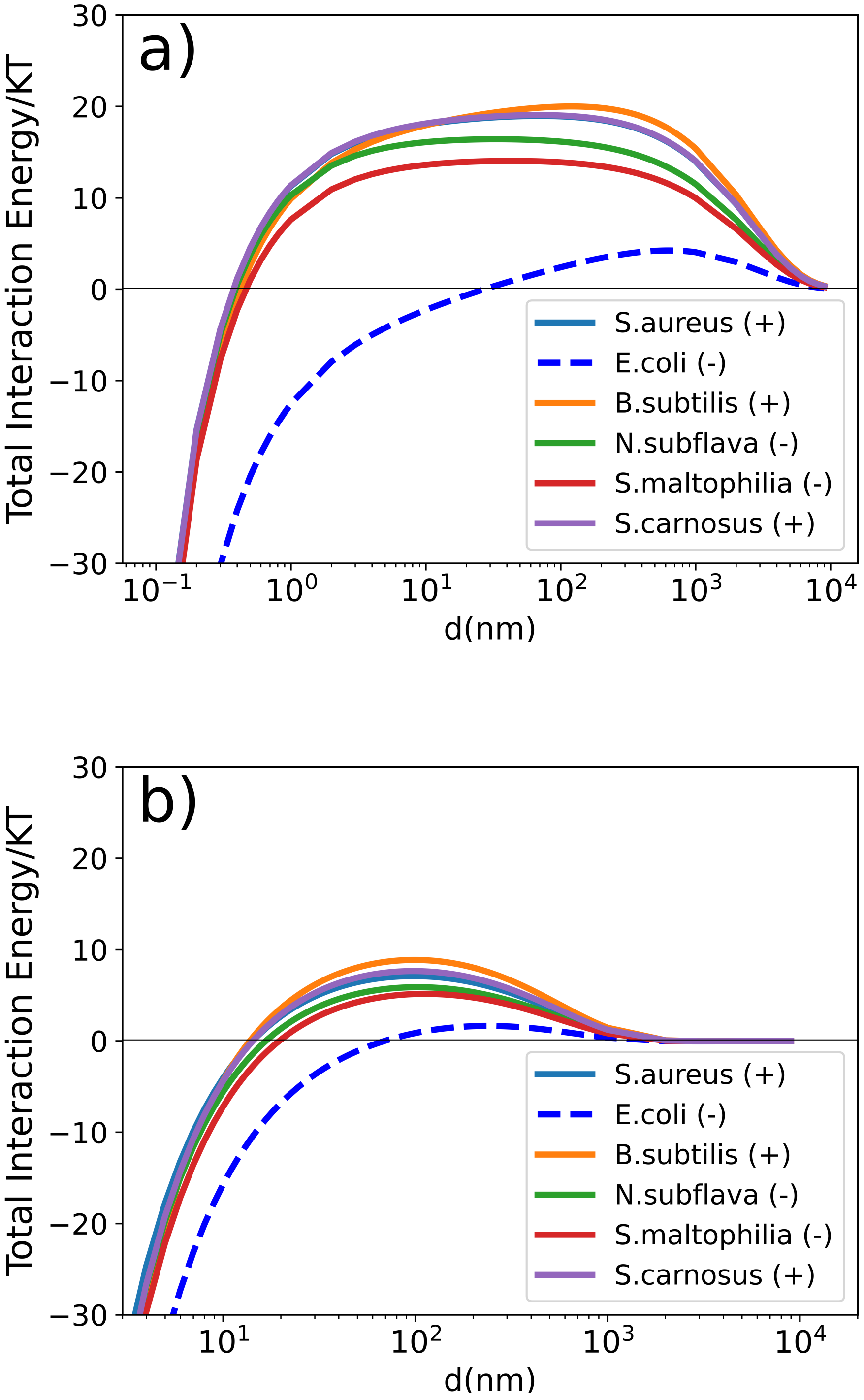

Figure 3.2: (a) Total interaction energies of the bacteria-MoS_2 nanoflakes for (a) water and (b) cyrene.

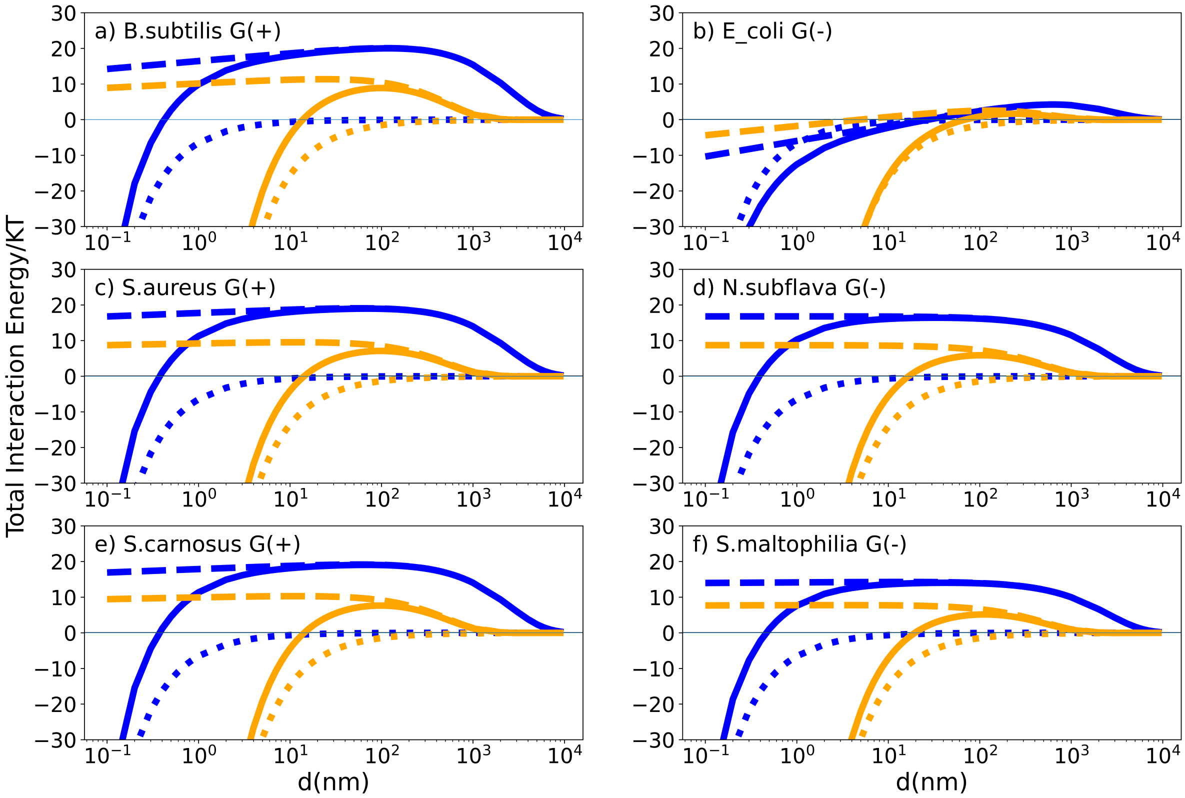

Figure 3.3: Water (blue) and cyrene (orange) MoS_2-bacteria total interaction energies (solid lines), van der Waals interaction energies (dotted lines), and electrostatic interaction energies (dashed lines for (a) *B. subtilis*, (b) *E. coli*, (c) *S. aureus*, (d) *N. subflava*, (e) *S. carnosus*, and (f) *S. maltophilia*.

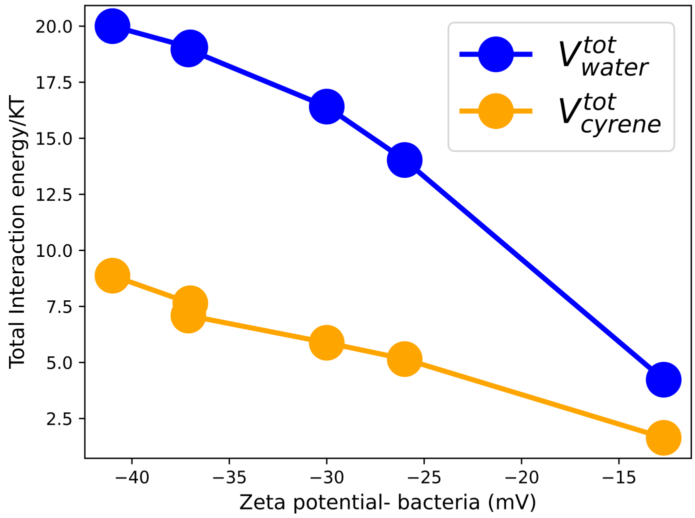

Figure 3.4: Total interaction energies as a function of the zeta-potential of the bacteria in water (blue) and cyrene (orange).

Gram-positive and Gram-negative bacteria have different cell membrane functional groups, which are responsible for their active binding with the foreign particles. Moreover, two-dimensional MoS_2 nanoflakes exhibit interesting Mo and S chemistry upon which exfoliation provides an active binding site for the pathogens to interact. Also, the exposed sulfur layers of transition metal dichalcogenides (TMDs) provide a strong affinity toward metal ions. The oxidative dissolution of exfoliated two-dimensional TMDs in aqueous media results in a slower sedimentation of the inorganic material [158]. This, in consequence may increase the time window useful for nanoflakes-bacteria interactions. Moreover, the exposed high surface area to volume of two-dimensional TMDs accounts for the exposable cytotoxicity because of the membrane stress produced. As for the solvent role, the exposed cytotoxicity of two-dimensional TMDs is due to the dissolution in that specific solvent where there is a considerable mismatch between solvent and nanoflakes in their surface tension.

As for the two-dimensional nanoflakes, several factors affect their interactions with bacteria, such as the aggregation of the dispersed material, the thickness of two-dimensional nanoflakes and their morphology, and the surface potential [152]. All of these effects motivate a study of the nanoflakes-bacteria interaction taking into consideration different types of membranes and solvent frames, underlying the need for a general prospect.

The DLVO theory analyzes nanoobjects-bacteria interactions considering two main forces: the van der Waals (V^{vw}) attractive force and the electrostatic component (V^{EL}), typically repulsive. The former, which has a short range of action, depends on the transitional medium and on the intrinsic properties of the material, whereas, the latter, having a much longer range, depends on the environmental parameters such as electrolyte types, concentration of ionic species in the aqueous medium, surface charge and radius of the bacteria membranes and the two-dimensional nanoflakes. In the current study, apart from the pure water as a solvent, a new green solvent, cyrene, has been investigated for the first time in order to study the solvent-based surface interaction of two-dimensional transition metal dichalcogenides with the bacteria. Cyrene is a dipolar aprotic solvent and represents the results of dehydrogenation of levoglucosenone by means of palladium-catalyst [159]. The thermodynamical properties of cyrene provides a good reason to use it for the exfoliation.

In this work, as a result of the many factors influencing the bacteria-nanoflakes interactions, we calculate the maximum interaction energies and critical volumes. Table 3.5 shows that van der Waals attractive forces dominates at short distances whereas the electrostatic repulsion is stronger at longer ranges in Table 3.4. Moreover, while vander-Waals forces smoothly depend on the solvent through the Hamaker constant, the electrostatic repulsion strongly depends on the solvent through both the electric permittivity,ϵ, which determines the energy scale of the interaction, and the k constant, the inverse of Debye-H€uckel length. As a result, the energy scale of the overall interactions energy is different between water and cyrene, being more than twice as high in the former compared to the latter. Additionally, since the solvent strongly influences only the electrostatic repulsion, while having a milder effect on the van-der-Walls attraction, the overall resulting energy barrier, through which nanoflakes must pass to approach the bacteria membrane, is different in the two solvents. For water, the barrier is higher and thicker than for cyrene, suggesting a more likely bacteria-nanoflakes interaction for the latter medium.

	Electrostatic interaction in water $\left(V^{EL}/\mathrm{kT}\right)$			Electrostatic interaction in cyrene $\left(V^{EL}/\mathrm{kT}\right)$		
	$d = 0.1$ nm	$d = 1$ nm	$d = 100$ nm	$d = 0.1$ nm	$d = 1$ nm	$d = 100$ nm
B. subtilis	14.209	16.438	20.047	8.905	10.145	10.421
S. carnosus	16.913	17.879	19.071	9.432	9.934	9.111
S. aureus	16.762	17.746	18.978	8.715	9.193	8.45
N. subflava	16.78	16.784	16.212	8.716	8.708	7.296
S. maltophilia	13.982	14.141	13.949	7.673	7.75	6.622
E. coli	-10.365	-5.976	2.461	-4.391	-1.784	2.506

Table 3.4: Comparison between the electrostatic interaction $\left(V^{EL}\right)$ for three separation distances ($d = 0.1, 1,$ and 100 nm) in water and cyrene.

	van der Waals interaction in water $(\mathrm{V^{vw}/kT})$			van der Waals interaction in cyrene $(\mathrm{V^{vw}/kT})$		
	d = 0.1 nm	d = 1 nm	d = 100 nm	d = 0.1 nm	d = 1 nm	d = 100 nm
B. subtilis	-65.572	-6.557	-0.066	-1554.494	-157.02	-1.554
S. carnosus	-65.282	-6.528	-0.065	-1467.844	-148.267	-1.468
S. aureus	-64.869	-6.487	-0.065	-1358.467	-137.219	-1.358
N. subflava	-65.096	-6.51	-0.065	-1416.521	-143.083	-1.417
S. maltophilia	-65.364	-6.536	-0.065	-1491.337	-150.64	-1.491
E. coli	-65.852	-6.585	-0.066	-1647.913	-166.456	-1.648

Table 3.5: Comparison of the van der Waals interaction $(\mathrm{V^{vw}})$ in three separation distances ($d = 0.1, 1,$ and 100 nm) for water and cyrene.

As for the negative surface charge that characterizes the six bacteria strains, resulting in negative value of the ζ-potential, this may be ascribed to the presence of specific charged and polar groups on the bacterial membrane of the considered species. The high negative ζ-potential of Bacillus subtilis and other two Gram-positive bacterial strains is because of the presence of anionic phosphate groups in the glycerol phosphate repeating units of teichoic acids on the peptidoglycan layers of the cell wall of the bacteria [119]; [160]; [161]; [162]. It is important to distinguish between the cell wall and the cell membrane. The cell wall, composed primarily of peptidoglycans in Gram-positive bacteria, provides structural support and protection. In contrast, the cell membrane, lying beneath the cell wall, is a lipid bilayer responsible for regulating the passage of substances into and out of the cell. On the other hand, the negative ζ-potential of *E. coli* and the other two Gram-negative strains may be due to the presence of phosphate and hydroxyl groups in the lipopolysaccharides across the outer layer of the bacteria [163]; [164];[165]; [166].

Figure 3.3 shows that all Gram-positive strains behave in a similar manner in terms of their interaction energy with two-dimensional $\mathrm{MoS_2}$ nanoflakes. These Gram-positive bacteria experience a strong repulsive force with a higher maximum interaction energy in pure water, $\approx$ 20 KT, compared to that in cyrene, $\approx$ 10 KT. Higher ζ-potentials in the three Gram-positive bacterial strains results in a strong repulsion with the two-dimensional nanoflakes because of the presence of different acidic functional groups. As a consequence, in water the Gram-positive bacteria have a mild interaction with two-dimensional nanoflakes, since they are unlikely to pass the large repulsive energy barrier

	Total interaction energy in water (V^{tot}/kT)			Total interaction energy in cyrene (V^{tot}/kT)		
	0.1 nm	1 nm	100 nm	0.1 nm	1 nm	100 nm
B. subtilis	-51.363	9.881	19.982	-1545.589	-146.874	8.866
S. carnosus	-48.37	11.351	19.005	-1458.412	-138.333	7.643
S. aureus	-48.107	11.26	18.913	-1349.751	-128.026	7.092
N. subflava	-48.316	10.275	16.146	-1407.805	-134.375	5.88
S. maltophilia	-51.382	7.605	13.884	-1483.664	-142.891	5.131
E. coli	-76.217	-12.561	2.395	-1652.304	-168.24	0.858

Table 3.6: Comparison between the total interaction energy (V^{tot}) in three separation distances ($d = 0.1, 1,$ and 100 nm) for water and cyrene.

to approach the membrane. In case of cyrene, this barrier is significantly reduced, both in height and distance extension, making a more significant impact upon the bacteria surfaces. In support of this statement, the critical volumes increase by more than ten times, from water to cyrene, passing from (1.5–3.4) $\times 10^5$ nm^3 to $(6–11.5)\times 10^6$ nm^3: Among the Gram-negative bacteria, *E. coli* exhibits a singular behavior. As a general feature, as shown in Figure 3.3b, *E. coli* shows a lower repulsion toward the two-dimensional nanoflakes, together with much smaller energy barriers to pass and larger critical volumes. The other two Gram-negative strains, *N. subflava* and *S. maltophilia* (Figures 3.3d and 3.3f) closely match the behavior of the Gram-positive bacteria.

We highlight, first, that *E. coli* is unique in its low (negative) ζ-potential, indicating a significantly lower surface charge than onto the other five strains, and large size, having the highest average radius.

	Separation value d_0(nm) when $V^{tot} = 0$ in water	Separation value d_0(nm) when $V^{tot} = 0$ in cyrene
B. subtilis	0.42	13.67
S. carnosus	0.38	14.03
S. aureus	0.38	14.13
N. subflava	0.39	16.53
S. maltophili	0.47	19.53
E. coli	27.34	67.03

Table 3.7: Separation distance d_0(nm) at which the total interaction energy vanishes and van der Waals attraction compensates for electrostatic repulsion.

Certainly, the unique structure of the *E. coli* membrane and the chemical nature of its functional groups also play an important role in explaining its singular behavior. The difference in the *E. coli* interaction curve is significant compared with the two other Gram-negative species. *E. coli* has capsular polysaccharides outside of the cell membrane, which may result in a stronger attraction toward two-dimensional nanoflakes, while *N. subflava* and *S. maltophilia* contain fewer capsular polysaccharides which provides additional carboxylic acid groups across their surfaces, possibly resulting in a reduced efficiency in surface contact [167]. We stress here that the unusual behavior forecasted for *E. coli* on the base of our model is in agreement with what recently was observed in the literature

[145], where *E. coli* growth in pure water was significantly inhibited more than *S. aureus* growth following treatment with two-dimensional MoS_2 nanoflakes. This indicates a stronger interaction with MoS_2 nanoflakes in water with *E. coli* than for *S. aureus.*

3.6 Conclusion

In order to investigate the interactions between three types of Gram-positive and three types of Gram-negative bacteria with MoS_2 two-dimensional nanoflakes, we used an extended version of the Derjaguin-Landau-Verwey-Overbeek (DLVO) model to consider the influence of solvents. We considered when bacteria and two-dimensional nanomaterials are placed into pure water and when a green solvent cyrene was employed. Our model considered the interplay of two interaction forces: the electrostatic repulsion between two-dimensional nanoflakes and bacteria membranes and attractive van der Waals interactions. While the former is a long-range repulsion, the latter represents a short-range attraction that dominates the nearby bacterial membrane. The Gram-positive bacteria have a larger repulsive interaction energy than Gram-negative bacteria and therefore have a larger energy barrier for the two-dimensional nanoflakes to overcome to approach bacterial membranes. Interestingly, the Gram-negative *E. coli* exhibits singular behavior compared to all the other bacterial strains. In fact, for *E. coli*, the electrostatic repulsion from nanoflakes is strongly reduced which implies a more effective interaction and a longer-range attraction. We attributed these features mostly to its lower ζ-potential with respect to the other strains. This phenomenon is likely due to the structure of its membrane, where capsular polysaccharides, outside of the cell membrane, are more abundant than in other strains. Additionally, other solvents, though both biocompatible, have different effects in mediating the bacterium-nanoflakes interaction. Indeed, the highly polar water solvent enhances the electrostatic interaction and its repulsive effects compared to cyrene, which is a more viscous dipolar aprotic liquid with lower dielectric constant than water. The proposed model is a general tool that may be utilized to investigate the interaction of all bacteria with other nanomaterial species in many solvents. The generalization of our model to consider other types of nanomaterials is easily performed by tuning the geometrical parameters of the nanostructure yielding different average radii or by introducing possible form factors to more specifically account for the nanostructure aspect ratio. Moreover, the electric interactions may also be finely controlled and tuned by modulating the ζ-potential of the nanostructure.

Chapter 4 Intro: Biocompatible Exfoliation of MoS_2 and WS_2 Nanosheets

This chapter is based on the following published paper:

International Journal of
Molecular Sciences

MDPI

Article

The Effectiveness of Cyrene as a Solvent in Exfoliating 2D TMDs Nanosheets

Jaber Adam [1,†], Manjot Singh [2,3,†], Avazbek Abduvakhidov [4], Maria Rosaria Del Sorbo [5], Chiara Feoli [2], Fida Hussain [1], Jasneet Kaur [1], Antonia Mirabella [2,6], Manuela Rossi [7,8], Antonio Sasso [1], Mohammadhassan Valadan [2,3], Michela Varra [4], Giulia Rusciano [1,*] and Carlo Altucci [2,3,9,*]

This chapter explores the use of cyrene, a biocompatible solvent, for the fabrication of high-quality defects-free MoS_2 and WS_2 nanosheets through liquid-phase exfoliation (LPE), specifically using ultrasonication. The impact of cyrene's properties on nanosheets characteristics is investigated through detailed characterization, including zeta potential, DLS, AFM, Raman, SEM, and UV-vis. These experimental findings are supported by DLVO modeling. Expanding biocompatible fabrication routes is essential for TMDs use in biomedical applications, such as drug delivery or developing new antimicrobial strategies.

Chapter 4

The Effectiveness of Cyrene as a Solvent in Exfoliating 2d TMDs Nanosheets

4.1 Abstract

The pursuit of environmentally friendly solvents has become an essential research topic in sustainable chemistry and nanomaterial science. With the need to substitute toxic solvents in nanofabrication processes becoming more pressing, the search for alternative solvents has taken on a crucial role in this field. Additionally, the use of toxic, non-economical organic solvents, such as N-methyl-2 pyrrolidone and dimethylformamide, is not suitable for all biomedical applications, even though these solvents are often considered as the best exfoliating agents for nanomaterial fabrication. In this context, the success of producing two-dimensional transition metal dichalcogenides (2D TMDs), such as MoS_2 and WS_2, with excellent captivating properties is due to the ease of synthesis based on environment-friendly, benign methods with fewer toxic chemicals involved. Herein, we report for the first time on the use of cyrene as an exfoliating agent to fabricate monolayer and few-layered 2D TMDs with a versatile, less time-consuming liquid-phase exfoliation technique. This bio-derived, aprotic, green and eco-friendly solvent produced a stable, surfactant-free, concentrated 2D TMD dispersion with very interesting features, as characterized by UV–visible and Raman spectroscopies. The surface charge and morphology of the fabricated nanoflakes were analyzed using ζ-potential and scanning electron microscopy. The study demonstrates that cyrene is a promising green solvent for the exfoliation of 2D TMD nanosheets with potential advantages over traditional organic solvents. The ability to produce smaller-sized WS_2—as demonstrated in our study compared to MoS_2—and mono/few-layered nanostructures with higher negative surface charge values makes cyrene a promising candidate for various biomedical and electronic applications. Overall, the study contributes to the development of sustainable and environmentally friendly methods for the production of 2D nanomaterials for various applications.

4.2 Introduction

From the past decade, it is clear that nanoscience has played a significant role in revolutionizing the discovery of novel materials with unique properties and vast application areas. Since the discovery of graphene [121]; [168], two-dimensional nanomaterials (2DMs), such as graphene [169], transition metal dichalcogenides (TMDs) [170] and other nanomaterials (NMs) [171], have attracted enormous enthusiasm due to their astonishing physical and chemical properties. Due to their unique characteristics, 2DMs are suitable for a wide range of applications in electronics/optoelectronics [20], energy storage [172] and biological systems [173]; [174]. Among 2DMs, TMDs, such as MoS_2 [175] and WS_2 [176], have become promising substitutes for graphene due to their high conductivity, exceptional catalytic abilities, high charge-density-wave transition and good biocompatibility [176]; [177]. It has been found that 2D TMDs exhibit a band gap of around 1–3 eV that becomes layer-dependent: for example, MoS_2 exhibits an indirect band gap in the form of a bulk-layered structure that transforms into a direct band gap of 1.8–1.9 eV [178] when it is machined in the form of nanosheets (NSs), becoming a semi-conducting layered material held together by weak van der Waals forces. Hence, the electronic structure of these materials can be tailored by machining their thickness in terms of the layer number of the fabricated NSs. This feature provides a unique and flexible platform to explore the potential of these NMs in view of diverse applications, such as, for WS_2 NSs, in environmental remediation, energy conversion and nano-theranostics [179].

Exfoliation of various 2D TMDs with high surface-to-volume ratios has remained a challenge for material scientists until now because many of the physicochemical processes involved in their fabrication in a given solvent context are still unknown. Generally, the fabrication of NMs is categorized into two approaches: bottom-up and top-down. The former utilizes the chemical reactions between atoms/ions or molecules and is based on various techniques, such as hydrothermal and chemical vapor deposition [134], whereas the latter is based on mechanical methods that break the bulk into nanoparticles by overcoming the van der Waals interlayer forces. In the top-down approach, the NMs' exfoliation is based on mechanical [41], solvent-assisted [180], chemically assisted [181] and electrochemical approaches [50].

Among these techniques, mechanical exfoliation results in high-quality monolayers, but it cannot be used at a large scale and does not allow systematic control over flake thickness and lateral dimensions. In the solvent-assisted approach, liquid phase exfoliation (LPE) is the most promising fabrication technique to date, as it allows production of large quantities of exfoliated NSs with good control over flake size and thickness, along with other advantages, such as the ease of producing composites and hybrid films (by just mixing two dispersions) [182]; [183]. The solvent plays a crucial role in this process, as it can affect the properties of the resulting materials, including their crystallinity, thickness and structural defects [184]. One of the ways to choose the best possible solvent is by matching its surface tension to that of the material [185]. This makes it possible to obtain higher stability for the fabricated dispersion.

Traditional solvents, such as N-methyl-2 pyrrolidone (NMP) and dimethylformamide (DMF), have been considered as the best solvents to exfoliate high-quality 2D NSs, but, on the other hand, these so-called “best” organic solvents are highly toxic; not environment friendly; very expensive compared to other commonly used organic solvents, such as NMP and DMF; and extremely difficult to post-process for applications. Additionally, these solvents are not at all suitable for sustainable chemistry processes, which has boosted the quest for potentially green novel NMs [186].

In this context, new aprotic, organic, green and eco-friendly solvents have been introduced into the scientific community for many applications [187]. Among these solvents, cyrene (known as 1S,5R)-6,8-dioxabicyclo [3.2.1]octan-4-one dihydrolevoglucosenone) is a pale yellow, dipolar, aprotic, green solvent with a mild ketonic odor derived in two simple steps from cellulose-containing biomass (cellulose to levoglucosenone and then to cyrene) [188]. It has been considered as the best-performing solvent in terms of toxicity [85], environmental persistence [189] and biocatalysis [187]. With physical properties such as high viscosity (14.5 cP at 25 °C), higher than that of NMP (1.67 cP at 25 °C) and DMF (0.92 cP at 25 °C), it plays an important role in exfoliating high-quality 2D TMD nanoflakes with fewer defects. Thus, inspired by these promising properties, several studies have shown the successful exfoliation of graphene in cyrene with high concentrations and better flake quality in terms of fewer defects [190], reporting the use of cyrene in the implementation of biocompatible inkjet printing and IoT applications [137]. As shown in one of our studies, the interaction of MoS_2 with cyrene can be modeled using the DLVO, a simple approach that easily allows the optimization of the fabrication parameters of the NMs [191]. In the current article, we highlight—to the best of our knowledge, for the first time— the fabrication of MoS_2 and WS_2 NSs directly in cyrene using a modified LPE technique. This was achieved by pretreating the solution, using bath sonication and then, finally, exfoliating with probe sonication for a longer time. We analyzed the behavior and the quality of the 2D NSs produced in this extremely viscous solvent. The synthesized 2D TMDs were characterized using various techniques, including ζ-potential, UV–visible and Raman spectroscopies and atomic force (AFM) and scanning electron (SEM) microscopies. The results of these analyses were used to evaluate the effectiveness of the LPE method using cyrene as a solvent in the preparation of high-quality MoS_2 and WS_2 2D flakes. The findings of this study demonstrate the potential of using cyrene as an effective solvent for the synthesis of high-quality MoS_2 and WS_2 2D NMs with minimal environmental impact and its potential usefulness as a green solvent in biomedical applications.

4.3 Results and Discussion

4.3.1 Exfoliation of MoS_2 and WS_2 NSs

One of the bottlenecks that needs to be overcome at this stage of nanoscience is achieving sustainable production of high-quality 2D materials, such as MoS_2, WS_2, graphene and its analogues, to make them available at a large scale. To achieve this aim, LPE is considered as one of the best routes, being easily accessible and capable of harnessing the potential of solvents used to disperse various classes of 2DMs [192]. Various factors play an important role in deciding the quality of exfoliated products, such as the type/quality of the pristine material, the exfoliation efficiency, the dispersibility of the solvent and post-processing fabrication steps [184]; [193]. To date, NMP is recognized as the most efficient organic solvent for the dispersion of various 2DMs, but it is neither sustainable nor suitable for up-scaling production due to its adverse impact on the environment [194].

In the current study, we explored the potential of cyrene for the exfoliation of 2D-MoS_2 and 2D-WS_2 nanosheets under optimized sonication conditions [195]. So far, cyrene has only been used to exfoliate graphene for bio-inkjet and IoT applications, for which optimized fabrication conditions were utilized to obtain high-quality 2D graphene nanosheet dispersion [137]; [65].

Here, inspired by our previous study, we employed a modified LPE technique to fabricate MoS_2 and WS_2 nanosheets in cyrene [145]. The present case setup operated under controlled temperature during sonication, which made it possible to obtain very stable and concentrated samples of 2D TMD dispersions.

4.3.2 Optical Characterization: UV–Vis Spectra

LPE will always produce polydisperse nanosheets including both small- and largesized 2D nanosheets. This also means that the final dispersion will contain 2D NSs of varied thicknesses, which can be separated in accordance with their size and thickness upon liquid cascade centrifugation. In this context, the acquisition of UV–Vis spectra is a quick approach to evaluate the average number of layers <N>, average size <L> and average concentration <C> for the exfoliated dispersion [145]; [91]; [196]; [197]. Indeed, within one sample/dispersion, UV spectra show characteristic, size-dependent spectral changes originating mostly from the absorbance and scattering components of the extinction, as the optical extinction spectra of small and large nanosheets include contributions from both the edge and basal plane effects, respectively [90]; [198].

Pure cyrene is not UV-transparent (Figure A.1); therefore, the UV–Vis analyses of the exfoliated MoS_2 NSs were performed by diluting the initial samples with water or methanol to reduce the strong solvent background in the 200–400 nm range. All the extinction bands in the UV–Vis profiles of the MoS_2/cyrene: water mixture (1:1 *v*:*v*) had very low intensity and were hardly detectable at their maximum values (Figure A.2). After decreasing the ratio of MoS_2/cyrene:water down to 1:20, the resulting UV spectra showed significant decreases in all the extinction bands, which became no longer identifiable (Conversely, the UV–Vis profiles of the MoS_2/cyrene: methanol 1:1 (*v*:*v*) mixture showed well-defined exciton bands (exciton A at 669 nm and exciton B at 610 nm; Figure 4.1A,B), which made it possible to calculate <N> for the production (N = 5.6; see Table A.1 for more details) [199].

Furthermore, at around 345 nm, the minimum for the UV profiles of MoS_2 NS dispersions generally appears [92], and the extinction spectrum at this wavelength, dominated by NS absorption phenomena, was used to calculate the NS average lateral size <L>. Nevertheless, the UV–Vis profiles of the MoS_2/cyrene: methanol 1:1 mixture were still partly affected by the cyrene absorption background, with this minimum shifting from

345 to 334 nm (Figure 4.1C). The <L> value calculated for MoS_2 from the absorption at 334 nm by using Equation 4.1 below [200] resulted in (121 ± 3) nm:

$$\mathrm{L}(\mu\mathrm{m}) = \frac{3.5\mathrm{Ext_B}/\mathrm{Ext_{334}} - 0.14}{11.5 - \mathrm{Ext_B}/\mathrm{Ext_{334}}} \tag{4.1}$$

where L is the average lateral size of the 2D NSs, Ext_B is the extinction value of exciton B in the UV–Vis spectra of the 2D TMD NSs and Ext_{334} is the extinction value at $\lambda_{min} = 334$ nm (in our results). This equation works well for nanosheets in the 70 nm < L < 350 nm size range, which is the typical size range for nanosheets produced by liquid-phase exfoliation.

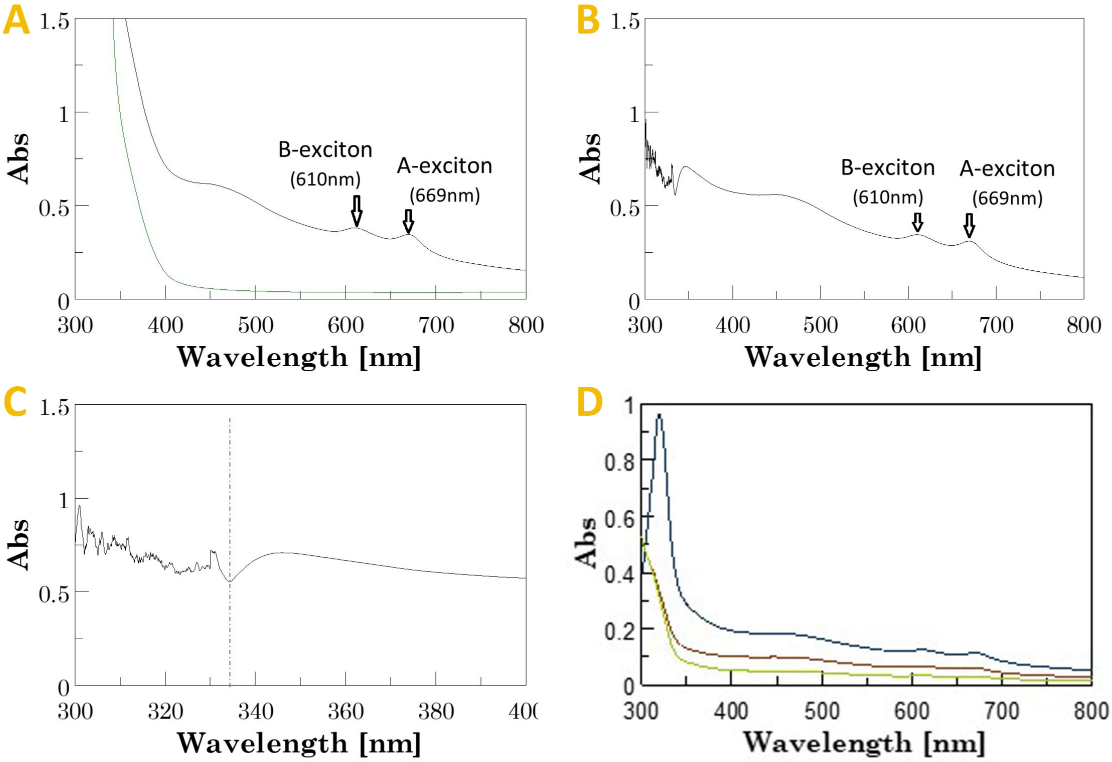

Figure 4.1: (A) UV spectra for cyrene (green line) and MoS_2/cyrene dispersion (blue line), both diluted with methanol (1:1; *v*:*v*). (B) Difference spectrum for 1:1 MoS_2/cyrene: methanol and 1:1 cyrene: methanol (*v*:*v*). (C) Enlargement of the difference spectrum highlighting the position of the minimum at 334 nm. (D) Difference spectra for MoS_2/cyrene: methanol and cyrene: methanol at dilution levels of 1:5 (blue line), 1:9 (red line) and 1:17 (green line). Inset shows the zoomed spectral region from 600 to 800 nm exhibiting the excitonic features of 2D-MoS_2 NSs.

However, as the transmittance of UV radiation at this wavelength was still significantly low due to the cyrene absorption, we also measured UV spectra using 5:1, 9:1 and 17:1 methanol: MoS_2/cyrene mixtures (Figure 4.1D). Herein, the transmittance became acceptable, but the convolution of the UV bands and the reduction in their intensity due to dilution caused the minimum in the 300–400 nm region to be no longer detectable. Therefore, we used the deconvolution function [201] (the Gaussian full width at halfmaximum (FWHM) function) in Spectra Analysis (Jasco software, Spectra manager, version 2.15.01), which enabled detection of the minimum (Figure A.3). In the case of the 5:1 methanol: MoS_2/cyrene mixture, this minimum was detected at 336.0 nm, whereas, when using 9:1 or 17:1 methanol: MoS_2/cyrene dilution levels, a very slight blue shift occurred (336.6 nm), thus suggesting that the cyrene background did not interfere with the UV absorption of MoS_2 at these two dilution levels. The <L> values obtained using the parameters from the latter two deconvoluted UV spectra were in the 165–179 nm range. No UV bands were observed in the UV profiles of the WS_2–cyrene dispersion diluted in water or methanol, which also used a final ratio between WS_2–cyrene and water or methanol of 2:1. The results obtained from previous studies suggested that the exfoliation procedure adopted gave rise to the formation of WS_2 quantum dots, for which confinement effects and a band gap transformation from indirect to direct occurred [202]. However, the use of cyrene, also in methanol-diluted mixtures, prevented the detection of the exciton edge band at 243 nm. Notably, differently from MoS_2–cyrene, the WS_2–cyrene mixture appeared transparent, similar to a solution rather than a suspension.

4.3.3 Microscopic Characterization: AFM

WS_2- and MoS_2-based nanoflakes produced by exfoliation in cyrene were also characterized by AFM according to the protocol described in the Section 3. Figure 4.2A,C show representative AFM scans for WS_2 and MoS_2 nanoflakes, respectively, together with selected flake height profiles. Both images clearly reveal the presence of few-layer flakes. From the analysis of numerous AFM scans, the thickness distributions of both the WS_2 and MoS_2 nanosheets were obtained, as shown in Figure 4.2B,D, respectively. Notably, in both cases, a lognormal distribution was observed (highlighted by the fit curves of the histogram data), as expected for exfoliated nanoflakes [203].

In the case of WS_2, the lognormal distribution peaked around 3 nm, and more than 50% of the observed nanoflakes had thicknesses $<$ 4 nm, confirming the effectiveness of our approach in producing few-layer flakes.

For the MoS_2 flakes, the fitted curve peaked around 4 nm but was much wider, with most flakes (∼35%) exhibiting thicknesses in the 4–8 nm range. Such a feature could have been due to somewhat incomplete exfoliation of the flakes with the employed protocol parameters. However, ∼25% of the obtained flakes exhibited thicknesses $<$ 4 nm, and ∼60% of them were thinner than 8 nm; therefore, they are reasonably suitable for numerous bio-related applications.

4.3.4 Spectroscopic Characterization: Raman Spectra

Finally, the exfoliated materials were investigated using Raman analysis, a quite common and effective tool for the characterization of 2D materials, due to the quite rich chemical and structural information provided by their Raman spectra. In particular, in layered TMDs, the E^1_{2g} and A_{1g} modes undergo a blue and a red shift, respectively, when

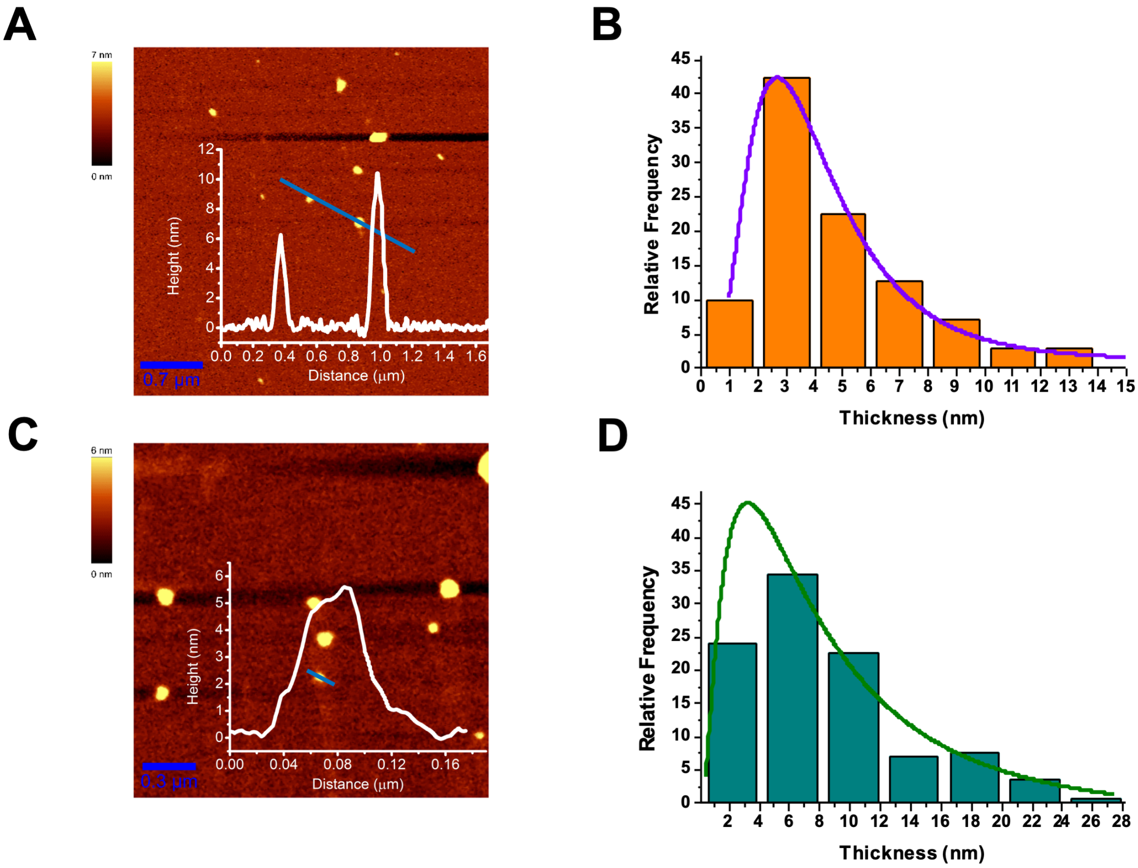

Figure 4.2: Typical AFM images of WS_2 (A) and MoS_2 (C) nanoflakes acquired in intermittent-contact mode. The two insets correspond to the height profiles across the blue lines shown in the respective topographies. (B,D) Analysis of flake thickness for WS_2 and MoS_2 nanoflakes, respectively. In both cases, the fitting curves of the data with a lognormal distribution are also shown.

passing from bulk crystals to monolayers flakes. This feature has been widely used in previous investigations to identify the number of layers in single exfoliated flakes [100]; [99]; [97]. In the present investigation, as the average nanoflake size was smaller than the spatial resolution of our system (in-plane and axial resolutions (PSF HWSHM) of ∼0.3 and ∼0.1 m, respectively), it was not possible to assign the acquired spectra to single nanoflakes, nanoflake groups or clusters, and the obtained information had to be averaged in accordance with the confocal detection volume.

In Figure 4.3, we show the mean Raman spectra for WS_2 (A) and MoS_2 (B) nanoflakes obtained by averaging 10 spectra acquired from different points of the samples. In the same figure, we also show the fitting curves for the Raman spectra using multipeak Gaussian functions. In particular, in the case of MoS_2, the fitting was performed using two Gaussian peaks featuring the characteristic E^1_{2g} and A_{1g} bands. As is well-known, the frequency shift $\Delta\nu_{MoS_2} = \nu_{A_{1g}}$ - $\nu_{E^1_{2g}}$ between these modes can be used to identify the number of layers in the nanoflakes. In our case, the Gaussian fitting allowed an accurate estimation of the peak's centers (∼0.1 cm^{-1} error), which finally provided a $\Delta\nu_{MoS_2}$ of ∼24.6 cm^{-1}, corresponding to nano-structuring spanning three to four layers. This outcome was consistent with the range of nano-structuring indicated by UV-Vis extinction spectroscopy.

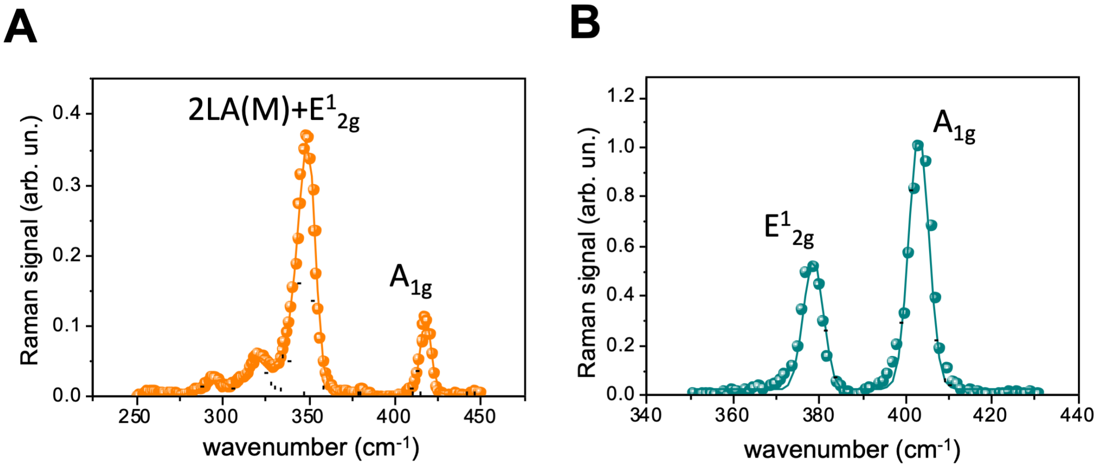

Figure 4.3: Raman spectra of WS_2 (A) and MoS_2 (B) nanoflakes using 532 nm laser excitation. For both spectra, colored dots correspond to experimental data points, while solid lines correspond to curves fitted with a multipeak Gaussian function. Finally, the single Gaussian peaks are indicated by black dotted lines.

Similar considerations could not be easily extended to the case of the WS_2 flakes. As is clearly visible in Figure 4.3A, the WS_2 Raman spectrum exhibited a complex pattern of overlapping peaks. This was partially due to a resonance effect for Raman excitation at 532 nm [204], which leads to complete overlapping of the 2LA(M) and E^1_{2g} modes. For this case, following the indications reported in [205], the WS_2 spectrum was fitted using five Gaussian peaks. As can be seen, the fit quality was relatively high. Nevertheless, a wide error (∼3 cm^{-1}) was obtained for the position of the overlapping peaks in the 325 cm^{-1} - 360 cm^{-1} spectral region. This intrinsically hindered the determination of the number of layers in the WS_2 flakes on the basis of the shift between the E^1_{2g} and A_{1g} modes. Nevertheless, some conclusions could be drawn on the basis of the spectral position of the A_{1g} band only. In particular, previous investigations with few-layer WS_2 flakes [204]; [205] found resonant Raman spectra exhibiting an A_{1g} band at 416.7 cm^{-1}, which was consistent with the frequency of A_{1g} (∼417.0 cm^{-1}) for the spectrum in Figure 4.3A. Notably, this was also in agreement with the AFM-based outcomes, which revealed the few-layer character of the produced WS_2 flakes.

4.3.5 Morphological Characterization: SEM

We further proceeded to characterize the main morphological features of the produced 2D NSs in cyrene using SEM. We highlight that the cyrene matrix context of our nanosheets, which were indeed embedded into a cyrene film, formed several different structures in a single image. These structures could be viewed at a large spatial scale (100 m steps in Figure 4.4A). Once diverse smaller domains with different features were identified within a single large domain, we zoomed into the identified smaller domains of interest to characterize different subsets of deposited NSs in each smaller domain (e.g., 100 nm and 200 nm steps in Figure 4.4B–F).

The SEM analyses were carried out with the MoS_2 and WS_2 NS flakes absorbed in the cyrene solid solution drop-casted on regular (Figure 4.4A–F) and irregular (Figure 4.5A–D) glass supports. These investigations allowed us not only to characterize the dimensions of the MoS_2 and WS_2 flakes but also to see how they were dispersed inside the cyrene solution. Therefore, we could observe the different textural and morphological features of the cyrene film with MoS_2 and WS_2 NSs, as below described. Visualizing the NSs in their solvent matrix context was important in view of the possible bioapplications of our liquid dispersion, mostly in the case of the cyrene solvent, which, though organic, is nevertheless biocompatible [195] and thus promising in this direction.

In Figure 4.4A–F, we report the characterization of 2D-MoS_2 and 2D-WS_2 NSs exfoliated inside cyrene and deposited onto a very regular silicon substrate. In Figure 4.4A, which shows the overall film texture and morphology, the presence of 2D-MoS_2 NSs can be seen in the cyrene at the rim and at the core of the drop-casted and subsequently dispersed solid solution on the regular glass support. At the rim, the cyrene film was thicker, folded and wrinkled, showing an irregular texture. In proximity to the rim, there were many coffee rings of different sizes. The irregular texture at the rim was linked to the presence of MoS_2 NSs totally absorbed in the cyrene film with very different lateral sizes, the mean being $<L> = 122 \pm 44$ nm from 30 single measurements (Figure 4.4C) scattered in a chaotic way.

At the core of the drop-casted and subsequently dispersed solid solution and at the center of the coffee ring structure [206], the film layer thickness was lower and the texture was more homogeneous (Figure 4.4E). The cyrene film rarely showed folds and wrinkles and the presence of coffee rings was reduced, but there were fractures. Here, the flakes had very small <L> values, the mean being $<L> = 26 \pm 7$ nm over 30 single measurements. However, nearby, we found domains where <L>, calculated from the flakes present in these domains, was even lower than 20 nm and at the threshold for nanoflakes to be considered as quantum dots. The flakes at the core of the cyrene film appeared as

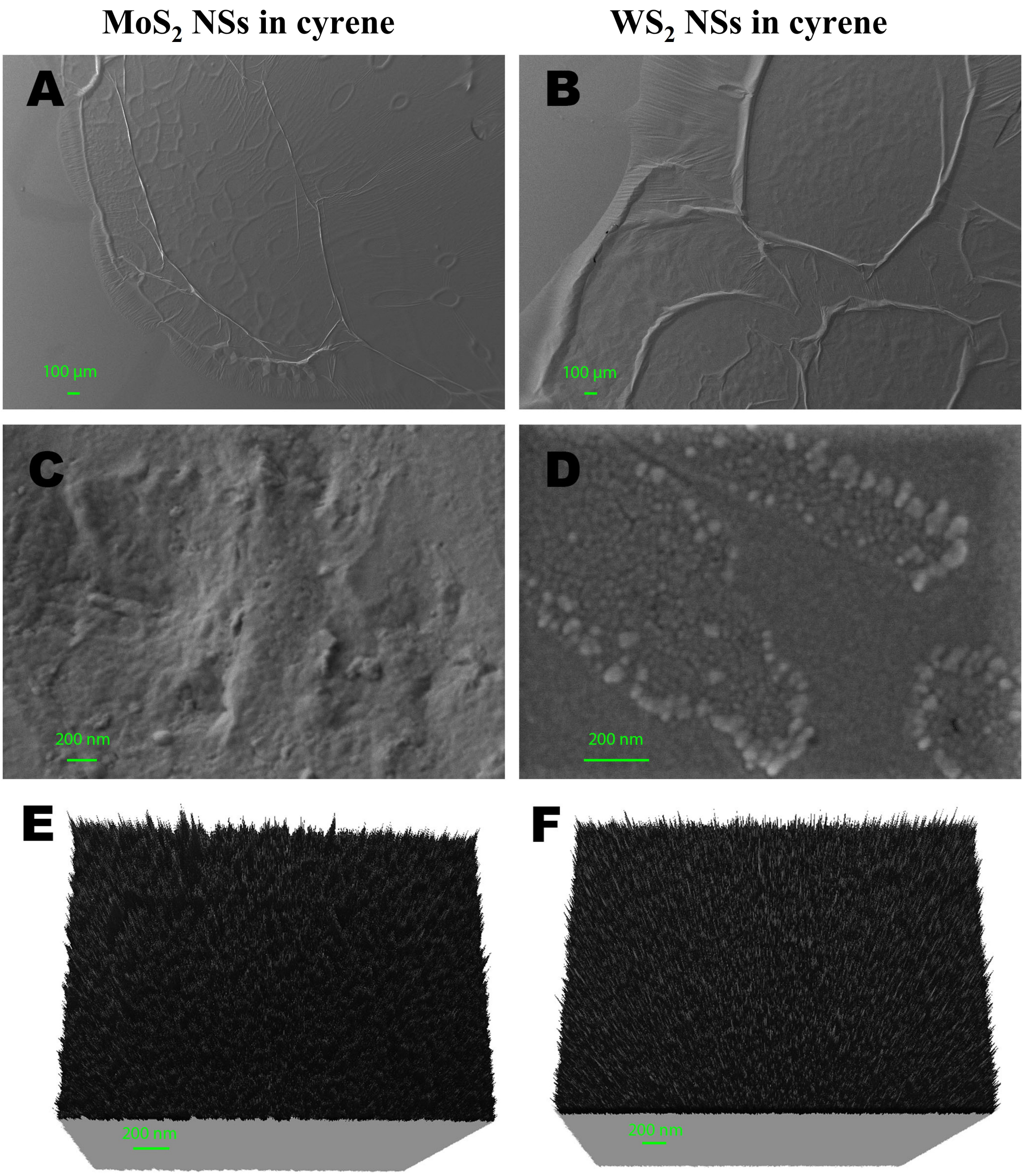

Figure 4.4: (A) MoS_2 NSs deposited over the silicon substrate absorbed by cyrene at the rim and center of the solid solution. Some coffee ring structures are also visible. (B) MoS_2 NSs chaotically absorbed under the cyrene film at the rim of the solid solution. (C) WS_2 NSs deposited over the silicon substrate absorbed by cyrene on the rim (green arrows) with the largest coffee ring. (D) A detailed SEM image of the area with imperfections in the cyrene film. The image shows the presences of WS_2 NSs arranged in a line and mostly presenting a specific oval-shaped pattern at the periphery. (E,F) Three-dimensional (3D) maps on a regular surface film (far from the rim) of the MoS_2 and WS_2 NSs in cyrene, respectively.

isolated and/or grouped, but they were more evenly distributed than at the rim. The intensity of the 2D-MoS_2 NS signal was quite low in comparison to that obtained from deposition in other dipolar aprotic solvents (details in Table 4.1), as the high viscosity of cyrene hindered the visualization of morphology, even after diluting the dispersion.

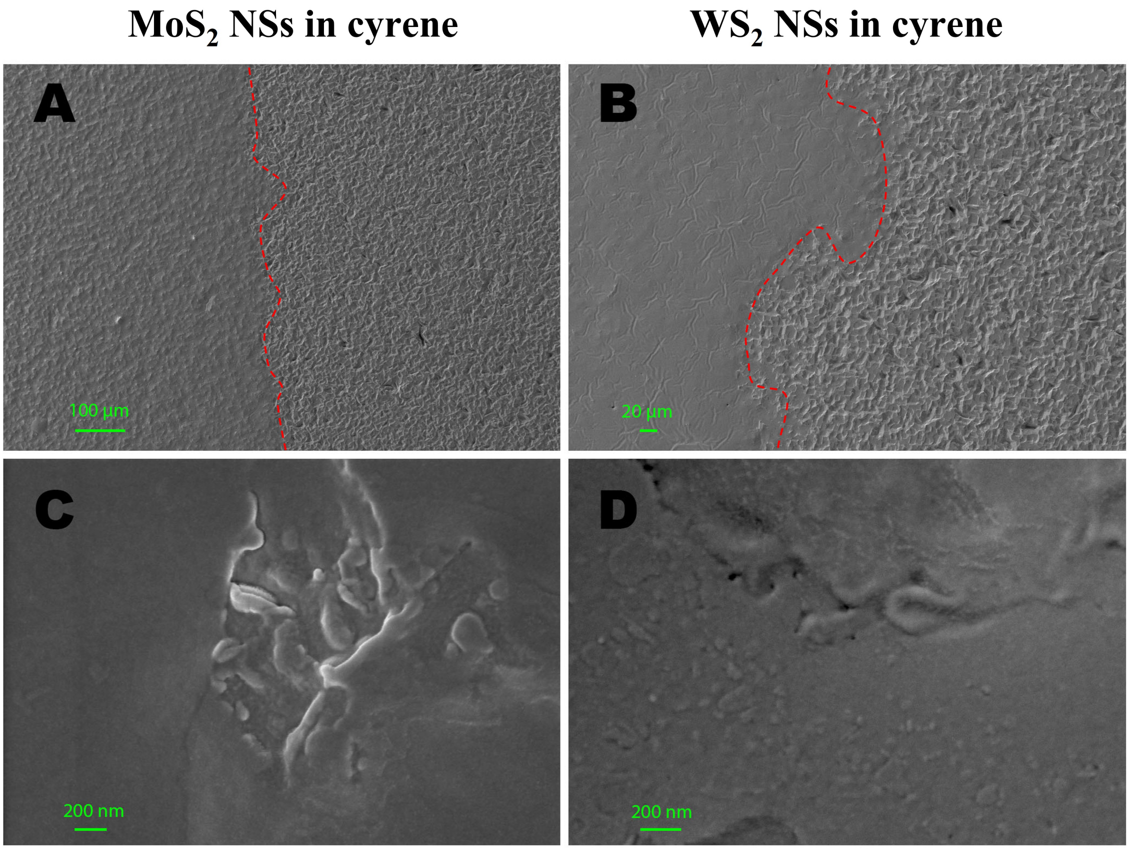

Figure 4.5: (A) Morphological features of MoS2 NS film dispersed in cyrene (left) on an irregular glass substrate (right). (B) Morphological features of WS2 NSs exfoliated in cyrene film (left) on an irregular glass substrate (right). (C) Two-dimensional (2D) MoS2 NSs deposited and partially absorbed on the irregular surface of the cyrene film. (D) Two-dimensional (2D) WS2 NSs in the proximity of the irregular surface of the cyrene film.

It is important to note here that, in Table 4.1, we report the 19–38 nm values as the minimum and maximum 2D-MoS_2 NS lateral sizes, respectively. This range of sizes was only ascribed to the cluster of 2D-MoS_2 NSs dispersed and deposited onto the core of the glass substrate for SEM measurements and not to the entire production of NSs. To clearly visualize the morphology of the 2D nanoflakes dispersed in cyrene, we measured deep into the thin film deposited onto the substrate by analyzing the nanomaterial in the specific regions of the core and rim (Figure 4.4). In contrast, $<L> = 121$ nm represents the overall average size for the production as estimated from the UV–Vis absorbance of the whole dispersion.

The NSs appeared to be non-homogeneously distributed only in the SEM images shown in Figure 4.4C. In total, the morphology of the thin film was homogeneous at the core and irregular at the rim; additionally, small conchoidal fractures appeared in the same image. The flakes not only showed different sizes but were differently dispersed at the rim and the core of the drop-casted solid solution.

As shown in Figure 4.4B, the 2D-WS_2 NSs in cyrene film turned out to be more homogenous than in the case of the 2D-MoS_2 NSs. Here, we also observed the formation of a thin film for the solvent, which was less folded and wrinkled near the rim. The coffee rings were larger than those for the 2D-MoS_2 NSs. The surface of the thin film looked homogeneous right at the center of the regions forming coffee rings, the only irregularities being the folds near the rim, the roughness profile and the punctual defects observed far from the rim film. The texture showed strong regularity in the dispersion of flakes both at the rim and the core in comparison to 2D-MoS_2 NSs. The irregular texture was due to the presences of punctual defects, where the flakes showed different sizes and were stacked on the defect surface. In this area, shown in Figure 4.4D, it was possible to observe the presences of WS_2 NS aggregates with average lateral sizes $<L> = 43 \pm 16$ nm. The size ranged between 29 nm and a maximum of 69 nm. The flakes were only partially absorbed in the cyrene layer coming up over the film surface.

Finally, at the core of the solid solution and in the center of the coffee ring, the film had a regular texture and the WS_2 NS flakes were homogeneously distributed and absorbed in the thin cyrene layer (Figure 4.4E). The sizes of the nanoflakes here were between 11 and 21 nm, and they rarely formed aggregates. Statistical sampling of 30 detected single nanoflakes resulted in an average $<L> = 13 \pm 5$ nm, which definitely indicated the presence of many 2D-WS_2 quantum dots in the preparation. The morphology of the thin film was more homogeneous both at the core and the rim compared to what was observed for the MoS_2 NS cyrene solution; additionally, small conchoidal fractures did not appear. The coffee ring showed a larger size, whereas the flakes showed different sizes, being differently arranged near punctual defects.

In Figure 4.5A–D, we report the characterization of 2D-MoS_2 and 2D-WS_2 NSs exfoliated in cyrene and deposited onto an irregular glass wafer, highlighting the influence of the different substrates, in terms of material and surface properties, on the type of cyrene matrix imaged for the analyzed preparation.

Figure 4.5A,B present the morphological analyses of MoS_2 and WS_2 NSs exfoliated in cyrene film and deposited on an irregular glass substrate support, with the images showing large-scale regions (100 μm in Figure 4.5A and 20 μm in Figure 4.5B, respectively) at the border of the deposited drop-glass substrate: the left side shows the drop-casted sample and the right side the glass substrate separated by a red dashed line following the border. It is evident that the film of WS_2 in cyrene completely filled all the cavities in the glass support, forming a continuous and homogeneous surface (Figure 4.5B); this only took place partially with the MoS_2 sample (Figure 4.5A). In fact, the surface of the MoS_2 film showed many irregularities that followed the morphology of the glass support, whereas, in the case of WS_2, only locally were parts of the glass support visible that were not completely covered by the film. The nanoflakes were homogeneously distributed and absorbed in the cyrene layer both for MoS_2 and WS_2 and visible only in proximity to deep holes present on the thin film surface (Figure 4.5C,D).

It important to stress that, as found from our analyses based on AFM for the thickness of the NSs and on SEM for <L>, as a general feature for LPE in cyrene, the MoS_2 NSs were bigger than WS_2 NSs both in thickness and in lateral size. This important finding was ascribed partly to the different pristine bulk sizes of the two materials but could also have been affected by the different intrinsic properties of the crystals.

In fact, ultra-sonication is a relatively high-energy process resulting in sonicationinduced scission during NS exfoliation. This scission effect is actually very important in defining NS dimensions because it plays an important role in reducing the flake size and thickness [207];[208]. In our case, we observed larger lateral sizes and thicknesses in 2D-MoS_2 NSs than in WS_2 NSs fabricated under comparable exfoliation conditions. The fact that larger flakes tend to be thicker reflects the fact that more energy is required to exfoliate larger-area nanosheets of a given thickness compared to smaller ones [207];[209]. This held true in our case because the initial MoS_2 bulk size (6 μm) was larger than the WS_2 bulk size (2 μm) as obtained from the producer.

Additionally, there were differences in the intrinsic properties of the MoS_2 and WS_2 bulk crystals that might have affected the final <N> and <L> values of the two materials independently of the solvent choice and exfoliation conditions. Normally, interlayer spacings of 0.615 nm and 0.618 nm exist between the two adjacent layers in MoS_2 and WS_2 NSs, respectively, which are connected with weak van der Waals forces [210]. There is also a difference of about 5% between the binding energies of 2D-MoS_2 and WS_2 NSs (-0.216 eV and -0.226 eV, respectively), as reported in a recently published study, which is due to the different spatial extensions of the excitons in the intra- and interlayer configurations [211]; [212].

A parameter that was considered as an indicator to evaluate the ease of exfoliation using LPE was the L/N ratio [207]; [213]. The higher the L/N ration is, the easier it is to obtain high-quality 2D NSs using LPE from pristine bulk materials. For LPE in ethanol, L/N = 11.3 and 10.2 has been measured for the mode values of the parameters for MoS_2 and WS_2 and <L>/<N> = 7.1 and 6.9 for the average values for MoS_2 and WS_2, respectively [199]; [200]; [207], where L is expressed in nm. In cyrene, we can confirm from our experiments that MoS_2 was easier to successfully exfoliate compared to WS_2, though the latter certainly showed more indications of the acquisition of quantum dots via LPE. In fact, we estimated that <L>/<N> = 6.5 and 4.3 for MoS_2 and WS_2, respectively. We noticed that the <L>/<N> value obtained in cyrene was, however, significantly smaller than that reported in ethanol for the same TMDs.

To conclude this section, the SEM analyses showed the different morphological and textural features of the cyrene film with 2D-MoS_2 and WS_2 NSs. The MoS_2 in cyrene film appeared irregular both in morphological features and in the dispersion of nanoflakes, while the WS_2 NSs in cyrene film appeared more regular both in morphology and in the dispersion of nanoflakes, as highlighted in Figure 4.4E,F, showing the experiment with a regular glass support, and in Figure 4.5A,B, showing the experiment with an irregular glass support.

Solvents	Surface Tension (mNm^{-1})	2D Material	Stability (Days)	Lateral Size (nm)	Thickness (nm)	Surface Charge (mV)	References
NMP	40.1	MoS_2	21	340	1-4.5	-32.1	[214], [215]
		WS	14	390-500	2-5	-41.1	
DMF	37.1	MoS_2	-	220-340	3-7	-	[216], [217]
		WS_2	21	1-2	$\sim$10	-	
Ethanol-H_2O	32.98	MoS_2	$\sim$21	130-150	1-3	-22.5	[179], [218]
		WS_2	30	$\sim$100	$\sim$3-4	-32	
H_2O	72	MoS_2	30	150-250	1-3.5	-27	[196], [219]
		WS_2	7	700-800	4.56	-	
Porcelain	38	MoS_2	$\sim$7	$\sim$2.5	4-5	-	[220]
		WS_2	$\sim$7	$\sim$1-2	<5	-	
Cyrene	33.6	MoS_2	>30	19-38	0.9-1.5	-50.4	Present work
		WS	>60	11-21	0.5-0.9	-86.5	

Table 4.1: Exfoliation of 2D TMDs in organic solvents in comparison with Cyrene: main characteristics of the obtained nanoflakes in terms of the principal parameters of the production.

4.3.6 TMD Exfoliation in Cyrene as Compared to Other Solvents: A Comparative Analysis of the Nanoflakes' Typical Parameters

In Table 4.1, we report a comparison of the main parameters related to other commonly used organic solvents with those of cyrene in terms of the exfoliation of the most used 2D TMDs: MoS_2 and WS_2.

As we can see in Table 4.1, the thickness, lateral size and stability of the produced NS dispersions were at quite an acceptable comparative level, making cyrene a potential candidate for the exfoliation of 2D TMDs for various biomedical and electronic applications. Moreover, the stability time of the 2D TMDs exfoliated in the current work in cyrene was longer than with the other reported solvents. This is also a very interesting finding in view of performing various biomedical assays, which require long stability times for a given nanomaterial dispersion.

Furthermore, the thickness of the 2D TMDs exfoliated in cyrene (in the range of 0.7–1.5 nm) was the lowest, resulting in monolayer and few-layered structures. This is also very interesting, making cyrene the most suitable solvent to obtain the highest possible surface-to-volume ratio, a fundamental parameter in many nanoscience and nanotechnology studies and applications.

Finally, the highest negative surface charge values for both the TMDs were found in cyrene as compared to the other more spread-out solvents. Such values lead to stronger edge-dangling bond interaction compared to the other solvents reported in Table 4.1 and could be a very useful feature in view of the NSs' functionalization with other chemical molecules or assembly with specific chemical groups.

4.3.7 Surface Charge Analysis: ζ-potential

Colloidal dispersions are generally stabilized through electrostatic repulsions [221]. In the case of 2DMs, dynamic interactions between the NSs and their electrostatic stabilization play a fundamental role in anticipating the stability of liquid dispersions. MoS_2 NSs are generally neutral but acquire negative or positive charges upon adsorption of a particular solvent or ionic surfactant [222]; [223]. Depending on the ionic strength of the solvent or the surfactant, the ζ-potential can be measured by assuming the distribution of the ions in the solution. As a consequence, the increase or decrease in the electrostatic potential from the surface of the 2D NSs can be estimated by using well-established equations and physical models, such as the Poisson–Boltzmann equation and the Debye–Hückel model [222]; [224]; [225]. In the present scenario, we observed high surface charge densities for MoS_2 and WS_2 NSs exfoliated in cyrene.

The ζ-potential values were measured three times for each scan, and the total number of runs was set to 100. Bulk MoS_2 exhibits high hydrophobicity and, upon exfoliation, the contact angle of the bulk material decreases; after further centrifugation steps, the angle is reduced further and the material will transform from a hydrophobic material to a hydrophilic material in a given solvent [222]. Normally, when exfoliated in pure water, MoS_2 and WS_2 NSs exhibit surface charges in the range of -26 mV to -32 mV, which provides a stable dispersion and sufficient electrostatic repulsive forces to avoid the aggregation of dispersed 2D TMDs [145]; [197]; [219]. Interestingly, we found that the ζ-potential values were significantly more negative in cyrene than those obtained with water for both materials, WS_2 being significantly more negative than MoS_2 with values of -86.5 ±1.5 and -50 ±3, respectively.

Thus, both MoS_2 and WS_2 exhibited high surface charge values. One possible reason for the strong polarity is the formation of hydrophilic groups during the exfoliation process between the 2D NSs and between the polar groups of cyrene and the 2D TMDs. The 2D-MoS_2 and 2D-WS_2 NSs were functionalized by ionizable groups (-SH and –HSO_3) formed during exfoliation and, as a result, the MoS_2 and WS_2 NSs became negatively charged by dissociating protons (H^+). Ultrasonic cavitation not only overcomes interlayer van der Walls interactions to produce thin NSs but is also involved in the process of fragmentation of large flakes into smaller ones. The latter process breaks Mo-S bonds and introduces large amounts of edge-attached dangling bonds, which further react with the solvent molecules. Therefore, cyrene can readily interact with the dangling bonds available on the edges of 2D-MoS_2 and 2D-WS_2 NSs, imparting high surface charge density to the dispersion.

On the other hand, the average lateral size of 2D NSs plays an important role in defining the ζ-potential of dispersed NSs. As can be seen from Table 4.1, the comparison of the different characteristics of cyrene-dispersed 2D NSs with those of other solvents, the average flake size and the viscosity of the solvent affect the ζ-potential of the NS dispersion. The large proportion of dangling bonds on the edges of the 2D-MoS_2 and WS_2 NSs dominate over the surface charge of the 2D NSs. The smaller the average flake size, the larger the edge effect is, strengthening the ζ-potential of the dispersed 2D NSs with greater electrophoretic mobility [222]; [224]. Solvent viscosity and permittivity, in connection with the exfoliation mechanism, impart stability and effective scission to 2D NSs. The 2D-MoS_2 and WS_2 NSs added to the viscosity of cyrene and imparted more energy to the suspension, which, via the cavitation effect, delaminated the material. In this respect, cyrene, being a highly viscous solvent, can efficiently transfer the force between the regions of the MoS_2 and WS_2 NSs, leading to effective size delamination. Of course, the initial bulk size and centrifuge steps also play equally important roles in defining the final average flake size [226].

4.3.8 Modeling the Interaction between 2D NSs and Cyrene: DLVO Theory

In order to obtain a picture of the interaction between the nanoflakes in cyrene during their fabrication, we used the modified DLVO theory [147] to work out an estimate for the total interaction energy between the nanosheets. We thus calculated the total interaction energy V^{tot} using the following equation:

$$V^{\text{tot}} = V^{EL} + V^{vw}, \tag{4.2}$$

where V^{vw} and V^{EL} are the van der Waals and the electrostatic interaction energies, respectively. The attractive van derWaals interaction energy was calculated as follows [191]:

$$\mathrm{V}^{\mathrm{vw}} = -\mathrm{Aa}/12\mathrm{d}, \tag{4.3}$$

where $\mathrm{A} = (\sqrt{\mathrm{A}_{\mathrm{nano}}} - \sqrt{\mathrm{A}_{\mathrm{cyrene}}})^2$ is the Hamaker constant [191] relative to the nanosheets machined into cyrene solvent, d is the nanosheets' reciprocal distance and a is the effective radius of theNS [225]. Basedon the values foundin the literature,we assumed that $\mathrm{A}_{\mathrm{nano}} = 29.6 \times 10^{-20}$ and 32×10^{-20} for MoS_2 and WS_2, respectively, and $\mathrm{A}_{\mathrm{cyrene}} = 2.84 \times 10^{-20}$ [191];[145]; [152]. The electrostatic repulsive energy V^{EL}, as a function of d, is given by:

$$\begin{aligned} V^{EL} &= \pi\epsilon a\left(\zeta^2\right) \times \\ &\left\{\ln\left[\frac{1+\exp(-kd)}{1-\exp(-kd)}\right] + \ln[1-\exp(-2kd)]\right\} \end{aligned} \tag{4.4}$$

where ζ is the zeta potential of the nanosheets, is the dielectric permittivity of the solution and k is the inverse of the Debye–H$\ddot{u}$ckel length λ_B, which depends on the temperature and on the ion concentration in the solution and can be calculated as $\approx 1/0.4$ μm for cyrene at room temperature [147]. In our case, we measured the values given in Table 4.2 for a, ζ.

Two-Dimensional (2D) TMDs	a (nm)	$\zeta(mV)$
MoS_2	26	-50.4
WS_2	13	-86.5

Table 4.2: Measured values of a, ζ for the calculation of the total interaction energy between 2D NSs

Based on the above model, we could calculate the total interaction energy between nanosheets in cyrene versus the separate nanosheets, as shown in Figure 4.6. Thus, the DLVO theory predicts a similar trend for the two nanomaterials, the reciprocal force of interaction between nanoflakes being repulsive with large separations and attractive for small distances at $d < d_{WS_2} = 13.5$ nm and $d < d_{MoS_2} = 35.8$ nm, respectively, with d_{WS_2} and d_{MoS_2} being the zeros of the curves, respectively, where the sign of the mutual force reverses. Interestingly, we noticed that these two zero values matched well with the measured <L> for the two materials. The agreement was perfect for WS_2 (13.5 nm vs. 13 nm) and still quite fair for MoS_2 (35.8 nm vs. 23 nm). We interpreted this finding as showing that the d_{WS_2} and d_{MoS_2}—the zero values where the NS reciprocal interactions change from attractive into repulsive—could give at least an indication of the lateral size of single nanoflakes obtained in the fabrication, these mutual forces becoming strongly repulsive at $d < d_{WS_2} = 13.5$ nm and $d < d_{MoS_2} = 35.8$ nm, thus setting an onset for the minimum possible size of a single nanoflake.

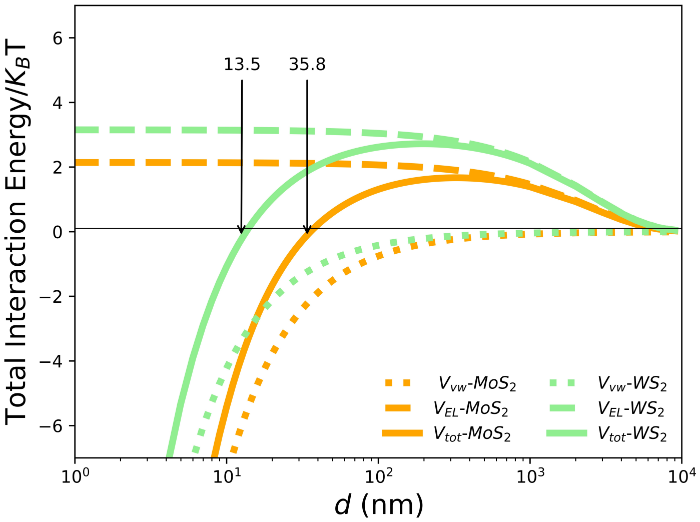

Figure 4.6: The total interaction energy between nanosheets in cyrene normalized to the thermal energy K_BT resulting from the sum of the van der Waals (dotted) and electrostatic (dashed) interaction energies (green for WS_2 and orange for MoS_2).

We also noticed that the barrier energy for transiting from repulsion to attraction was higher and wider for WS_2 as compared to MoS_2, which could explain the stronger tendency for MoS_2 to form aggregates during the fabrication, as observed in the AFM and SEM characterizations.

4.4 Material and methods

4.4.1 Exfoliation and Size Selection

The initial commercialized bulk molybdenum disulphide (MoS_2) powder (Sigma- Aldrich, Darmstadt, Germany, 69860, particle size: 6 μm, 99%, density: 5.06 g/mL at 25 °C) and tungsten disulfide (WS_2) powder (Sigma-Aldrich, Darmstadt, Germany, 243639, particle size: 2 μmm, 99%, density: 7.5 g/mL at 25 °C) were exfoliated in cyrene as a solvent (Sigma-Aldrich, 807796, molecular weight: 128.13 g/mol, flash point: 108 °C, density: 1.25 g/mL). The materials were dispersed in cyrene at an initial concentration of 5 mg/mL. The solution was pretreated with bath sonication for 15 min. Then, LPE was executed using tip sonication with a Bandelin Ultrasound SONOPLUS HD3200, Berlin, Germany (operating frequency of 20 kHz and maximum power of 200 W) tip sonicator equipped with a probe (KE-76). The pretreated solution was exfoliated for a further 2 h at 60% amplitude using pulse mode (10 s on, 10 s off) in a quartz bottle. To avoid the production of high heat and temperature due to the collision of cavitation bubbles, sonication was performed using an ice bath and the operating temperature of the device was set at 15 °C. Simultaneously, the output power was calculated, and it was consistent throughout the sonication period, resulting in a homogeneous dispersion of the given material. After sonication, the dispersion was centrifuged (Megafuge^{TM} 16 Centrifuge, Thermo Scientific^{TM}, Waltham, MA, USA, equipped with a rotating angle rotor) at room temperature at 300 rpm for 60 min and the sediment containing the un-exfoliated part of the material was discarded. The supernatant was moved to 5000 rpm, after which the sediment was discarded in the last step. The supernatant was stored at 4 °C for further use.

4.4.2 Characterization: UV–Vis

To characterize the resulting 2DMs, we used a range of techniques, including ultraviolet– visible (UV–Vis) spectroscopy, Raman spectroscopy, ζ-potential, scanning electron microscopy (SEM) and atomic force microscopy (AFM). These techniques allowed us to assess the thickness, shape and concentration of the resulting materials, as well as their optical properties. The UV–Vis spectroscopy measurements were performed using a Jasco-700 UV–Vis spectrophotometer, Italy, with a 1 cm thick quartz cuvette and a spectral range of 200–800 nm to determine the exfoliated MoS_2/WS_2 absorption spectra.

4.4.3 Characterization: Raman and AFM

Measurements of Raman spectra were conducted using the commercialWiTec Alpha 300 confocal micro-Raman system. This system is composed of an inverted confocal Raman microscope and an atomic force microscope (AFM) placed on top of the inverted confocal microscope. This latter is equipped with a 532 nm probe generated with a frequency-doubled Nd-YAG laser and a 1800 grove/mm grating, assuring a spectral resolution of

$\sim$1.5 cm$-$1. Raman spectroscopy was used to assess the exfoliated materials' quality by investigating the exfoliated flakes' structural properties. AFM was used to measure the flake thickness and to investigate the NSs' surface topography. For this purpose, flake suspensions were first diluted in methanol (1:4 ν/ν) and then 50 μL portions of these suspensions were spun on a clean SiO2/Si substrate at 3000 rpm for 60 s. Finally, the substrates were washed with acetone and dried with a gentle N_2 flux. This last step was performed to reduce the embedding of flakes in the cyrene films, which clearly would have prevented the observation of the thinner flakes and the correct evaluation of flake thickness. AFM analysis was performed in intermittent contact mode to avoid the perturbation of flakes' adhesion to the substrate. For the AFM characterization, nanoflake suspensions were drop-cast on glass coverslips and stored for 48 h at room temperature to allow complete cyrene evaporation. Measurements were performed using a 100 infinite-corrected objective, which provided in-plane and axial resolutions (PSF-HWHM) of $\sim$0.3 and 1 μm, respectively.

4.4.4 Surface Charge and Average Lateral Size Measurement: ζ-otential

Electrostatic stabilization is an important parameter to analyze the stability of liquid exfoliated dispersions. The surface charges generated during the exfoliation can be attributed to electrophoretic mobility (μ). The ζ-potential measurements were performed using a Malvern Zetasizer Nano system, United Kingdom (UK) with a He-Ne laser as the excitation source. The ζ-potential measurements were performed to determine the charge on the surface of the exfoliated NMs. All the measurements were carried out at 25 °C.

4.4.5 Morphological Measurements: SEM

A Zeiss Merlin VP Compact SEM apparatus (DiSTAR laboratory, Università degli Studi di Napoli Federico II) was used for morphological analyses of the samples. The Zeiss Merlin VP Compact field-emission electron microscope was equipped with a Gemini II camera and FeSEM: SmartSem software controller. The SEM was composed of three secondary electron detectors (SE2 (classic detector), VPSE (variable pressure) and InlensDuo (low voltage)) and two backscattered electron detectors (AsB and InlensDuo). The SEM was equipped with a charge compensation system and with Oxford Instruments Microanalysis (both EDS X-max 50 and WDSWave). Data processing was undertaken using INCA version 4.081 (Oxford Instruments (2006): INCA—The microanalysis suite issue 17a C SP1—Version 4.08. Oxford Instr. Anal. Ltd., Oxfordshire, UK); (EDS and WDS) and Aztec (EDS). The Software for data imaging of FeSEM is SmartSem. The samples were placed on a glass support with both smooth and irregular surfaces with an appropriate droplet drop-casting method; then, they were metalized with gold using a sputter coater.

4.5 Conclusion

This study reports the very first experimental characterization of the exfoliation of MoS_2/WS_2 nanosheets in cyrene, a dipolar, aprotic, green solvent. Liquid-phase exfoliation, which is the most accessible and reproducible fabrication route for large-scale production of nanosheets, was, in our case, employed with some novel steps, such as a pre-treatment phase of bath sonication lasting 15 min, in order to produce smaller-sized and mono/few layered nanostructures. Consequently, we also observed an enhancement in the efficiency of exfoliation when visualizing the stability of the dispersion for more than a month, which is very meaningful and possibly crucial for various biomedical tests and assays.

UV–visible extinction spectroscopy results showed very clear corroborations with the Raman spectra and Raman mapping of the exfoliated 2D TMD nanosheets when observing the most significant features of the mono/few-layered nanostructures.

SEM morphological analysis revealed peculiar behavior for the nanometric production in cyrene, which was likely due to the high viscosity of the solvent. As a result, a thin, wrinkled, folded and fractured film composed of nanosheets embedded into the solvent was observed with SEM for the 2D-MoS_2 nanosheets, whereas the 2D-WS_2 nanosheets showed a very thin film that was less wrinkled and folded and had no fractures, demonstrating a regular morphology. The 2D NSs showed variations in the lateral size according to the film texture. The 2D-MoS_2 NSs obtained had 122 ±44 nm of irregular texture and 26 ±7 nm of regular texture, whereas the 2D-WS_2 NSs had 43 ±16 nm of irregular texture and 13 ±5 nm of regular texture.

The AFM spectra revealed that the thickness of the mono- and few-layered nanostructures were in perfect agreement with the absorbance and Raman spectra.

The ζ-potential characterization of the obtained products revealed that the nanoflakes were negatively charged for both MoS_2 and WS_2, with the latter being more negative. For both materials, the absolute value of the measured potential was significantly higher than that typically reported in water exfoliation.

Cyrene, being very viscous and having a high boiling point, posed some serious issues during the exfoliation, post-exfoliation and sample preparation steps for various characterizations, which need to be studied in further detail. Our study, however, demonstrated that the final quality of the nanoflakes in terms of thickness and lateral size was high and comparable (if not even higher, such as for the lowest possible number of layers) with that obtained by using other organic solvents. Considering the supposed green nature of the cyrene solvent, our results indicate it as a potential candidate for numerous biomedical applications involving liquid large-scale production of nanoflakes.

Chapter 5 Intro:Gamma Radiation and MoS$_2$ nanosheets: Effects and Analysis

This chapter investigates the effects of gamma radiation on water-dispersed MoS$_2$ nanosheets, prepared via liquid-phase exfoliation (ultrasonication). Changes in the nanosheets are analyzed experimentally through centrifugation and a suite of characterization techniques, including zeta potential, DLS, AFM, Raman, SEM, and UV-vis. Monte Carlo simulations further explained the underlying mechanisms. These observed radiation-induced changes offer potential for controlled, radiation-mediated modification of MoS$_2$ properties, opening opportunities in targeted drug delivery systems or as radiosensitizers for innovative cancer therapies.

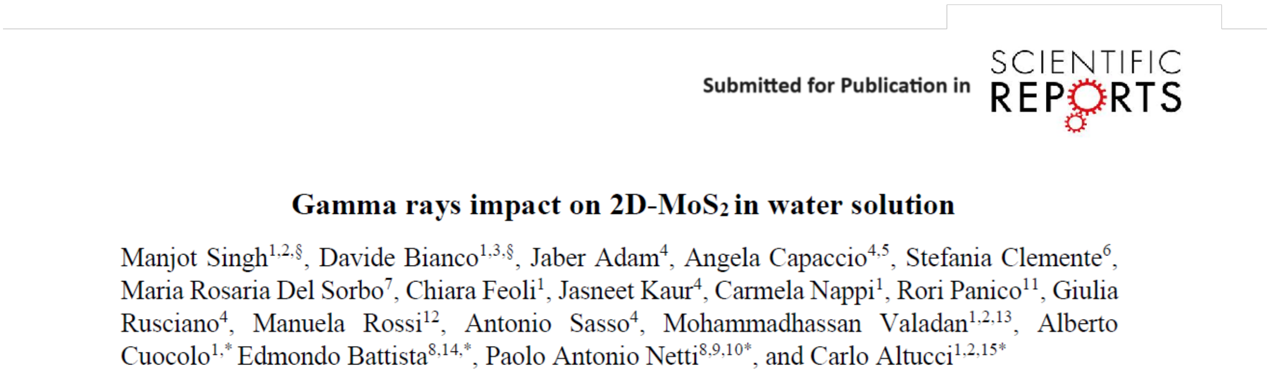

Submitted for Publication in SCIENTIFIC REPORTS

Gamma rays impact on 2D-MoS$_2$ in water solution

Manjot Singh[1,2,§], Davide Bianco[1,3,§], Jaber Adam[4], Angela Capaccio[4,5], Stefania Clemente[6], Maria Rosaria Del Sorbo[7], Chiara Feoli[1], Jasneet Kaur[4], Carmela Nappi[1], Rori Panico[11], Giulia Rusciano[4], Manuela Rossi[12], Antonio Sasso[4], Mohammadhassan Valadan[1,2,13], Alberto Cuocolo[1,*] Edmondo Battista[8,14,*], Paolo Antonio Netti[8,9,10*], and Carlo Altucci[1,2,15*]

Chapter 5

Gamma rays impact on 2D-MoS_2 in water solution

5.1 Abstract

Two-dimensional transition metal dichalcogenides, particularly MoS_2, are interesting materials for many applications in aerospace research, radiation therapy and bioscience more in general. Since in many of these applications MoS_2-based nanomaterials can be placed in an aqueous environment while exposed to ionizing radiation, both experimental and theoretical studies of their behaviour under these conditions is particularly interesting. Here we study the effects of tiny imparted doses of 511 keV photons to MoS_2 nanoflakes in water solution. To the best of our knowledge this is the first study in which ionizing radiation on 2D-MoS_2 occurs in water -. Interestingly, we find that, in addition to the direct interaction between high-energy photons and nanoflakes, reactive chemical species, generated by γ-photons induced radiolysis of water, come into play a relevant role. A radiation transport Monte Carlo simulation allowed determining the elements driving the morphological and spectroscopical changes of 2D-MoS_2, experimentally monitored by SEM microscopy, DLS, Raman and UV-vis spectroscopy, AFM, and X-ray photoelectron techniques. Our study demonstrates that radiolysis products affect the Molybdenum oxidation state, which is massively changed from the stable +4 and +6 states into the rarer and more unstable +5. These findings will be relevant for radiation-based therapies and diagnostics in patients that are assuming drugs or contrast agents containing 2D-MoS_2 and for aerospace biomedical applications of 2DMs investigating their actions into living organisms on space station or satellites.

5.2 Introduction

Nanomaterials often exhibit noticeable properties strongly related to their fabrication and changes in their bulk counterparts, offering unique physical, chemical, and biological features. Given that, graphene and two-dimensional nanomaterials (2DMs) have gained an increased attention in past decades [227, 228, 169]. Within the family of novel nanomaterials, 2D transition metal dichalcogenides (2D-TMDs), such as MoS_2, WS_2, $MoSe_2$, and WSe_2, have enticed significant research activities due to the remarkable tunability of their electronic band structure [229, 230] and confined dimensionality, offering a broad range of unique electrical, optical, chemical and mechanical properties [231, 232]. In this scenario, 2D-TMDS are considered as the most promising candidates in various applications [233, 234, 235], including radiotherapy and cancer theranostics, through labelling with radionuclides [236, 237, 238] and long-distance quantum communication [239, 240, 241].

The study of the interactions between ionizing radiation and 2DMs has emerged as an important field of research, accounting for the modification in the structure and properties of these novel materials. Impact of radiations on the electrical properties of graphene has been extensively studied, but little is known about their effect on the properties of 2D-TMDs and other novel NMs [242] One of the most evident consequence of irradiation is the induction of defects, an adverse effect compromising the normal operation of 2DMs-based devices [243, 244, 245, 246].

Herein we present the first study, to the best of our knowledge, of the effect of 2D-MoS_2 irradiation in water. Irradiation was performed through 511 keV photons resulting from the annihilation of positrons arising in beta decay of ^{68}Ga, a radionuclide which has gained attention in the field of oncology and in the clinical application of targeted imaging of various receptors, enzymes, antigens related to diagnosis and discrimination of inflammation and infection diseases22

The motivation for this investigation is relevant and evident: the behaviour of nanomaterials in liquid water is intrinsically connected to their interaction in living matter [196, 145, 197, 191, 247] Particularly, 2D-MoS_2 irradiation in water well describes the physiological context occurring in ionizing radiation therapies accompanied by the delivery of 2DMs-based contrast agents or drugs21. For instance, nano-carriers are used for the delivery of therapeutic radioisotopes into tumours, or of chemotherapeutic drugs for synergistically combined chemo-radiotherapy[247]. Moreover, the results of our study are also relevant in the field of ionizing radiation dosimetry, where 2D materials and more in general nanocomposites and nanomaterials have found lately massive use to achieve enhanced sensitivity of many dosimetric systems while still achieving tissue equivalency [248].

Finally, a deeper insight on the effect of radiations on 2DMs in a water context surely is greatly impacting on all the possible bio-applications in space, like for example experiments carried on space stations or satellites on biosensing in plants or living organisms or drug delivery to living cells and organisms [249].

Among the peculiar features resulting from the water-based environment, the production of highly reactive chemical species produced by energetic photons such as hydronium ion, H_3O^+, hydroxyl radical and hydroxide surely plays a crucial role31. As a matter of fact, the formation of these species is almost absent for irradiation of nanoflakes in air, where it derives from the presence of tiny vapour layers on nanomaterials, as reported in references [243, 244]. In addition, the density of the surrounding medium in water is a thousand times higher than in air: this makes the effects of the ionizing radiation treatment on 2DMs quite relevant even at radiation doses much lower than that required to observe analougue impacts in air[250].

The effect of the irradiation on 2D-nanoflakesNSs is studied globally by analysing the shifts of selected Raman features, whereas Atomic Force Microscopy (AFM) is utilized to study the induced structural changes by probing the morphology of targeted and non-targeted 2D-MoS_2 nanoflakes. In addition, X-ray Photoelectron Spectroscopy (XPS) is exploited to analyse the generation of defects looking at the significant peak changes in the Mo and S inner shell spectra. The scientific outcomes are supported by a Monte Carlo simulation, describing the interactions between 511 keV photons and MoS_2 nanoflakes in water environment. In this way, we gained a deeper insight on the physical mechanism for indirect action onto nanoflakes by radical species induced in water by γ-irradiation.

5.3 Results

The aim of the present paper consists indeed in studying the impact of gamma-ray irradiation on 2D-MoS_2 nanoflakes, produced with a modified liquid-phase exfoliation (LPE) process, in water solution, which represents a novel and very important surrounding context as compared to previous experiments reported for air in the literature.

5.3.1 Sample production and Irradiation

LPE being a very versatile fabrication route gives several opportunities to obtain high quality 2D nanoflakes of varied materials. Compared to other chemical routes of exfoliation, LPE offers an environment friendly and commonly suited synthesis technique with a wide range of solvents resulting in defect free 2D nanoflakes. In the current study, a single step fabrication approach was adopted with a careful optimization of pre- and post-sonication parameters to obtain a stable 2D-MoS_2 dispersion in liquid water (see Materials and Methods section). Before irradiation, MoS_2 NSs were subjected to analyse the UV-Vis absorbance spectra in order to extract the basic information on the physical parameters of the exfoliated 2D NSs such as the average lateral size, average final concentration and the average thickness of the 2D NSs (shown in Figure B.1).

Following the fabrication and post fabrication steps, MoS_2 nanoflakes were subjected to irradiation through 511 keV photons resulting from the annihilation of positrons arising in the beta decay of the ^{68}Ga radionuclide.

A scheme of the experimental set-up exploited for irradiating 2D-MoS_2 dispersion is shown in Figure 5.1. A vial containing a pharmaceutical radiolabelled with ^{68}Ga, on the left, has been clamped with a vial containing the water solution of 2D-MoS_2 nanoflakes in a face-to-face configuration. The concentration reached through the exfoliation and centrifugation processes was equal to 50 μg/mL. ^{68}Ga decays with a half-life of 67.7 min, through positron emission, to the stable isotope zinc-68 (68Zn) with a 82-89% yield and an energy spectrum ranging from 242 keV to 1892 keV [251].

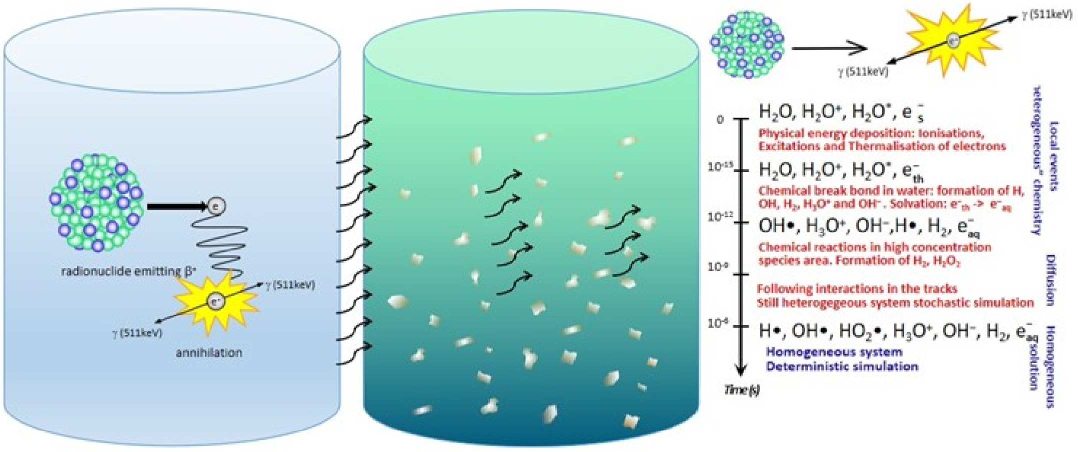

Figure 5.1: Sketch of the experimental set-up. ^{68}Ga solution and 2D-MoS$_2$ dispersion were kept separated to study the interactions with produced 511 keV photons and radiolysis products in a water environment.

Water solution determines a fundamentally different irradiation condition with respect to the context [246, 250]. Positrons themselves cannot reach the second vial, because of their short range in water and glass. Considering, for instance, the semiempirical approach discussed in [252], we calculated the mean and maximum positron range in both media by:

$$R_{\text{mean}}(\text{cm}) \approx \frac{0.108[E_\beta^{\max}(\text{MeV})]^{1.14}}{\rho(\text{mg cm}^{-3})}; \tag{5.1}$$

$$R_{\max}(\text{cm}) \approx \frac{412[E_\beta^{\max}(\text{MeV})]^{n}}{\rho(\text{mg cm}^{-3})}; \quad 0.01 \leq E \leq 2.5 \text{ MeV} \tag{5.2}$$

where the exponent n is given by

$$\text{n} = 1.265 - 0.0954 \ln E_\beta^{\max}(\text{MeV}) \leq 2.5 \tag{5.3}$$

Assuming ρ=1 g cm^{-3} for water and ρ=2.7 g cm^{-3} for glass, we obtained the mean and maximum values of the positron emitted by ^{68}Ga, reported in Table B.2. In our set-up positrons should travel at least 5 mm of glass before reaching the solution of the second vial containing MoS$_2$ nanoflakes, considering the minimum possible crossed thickness of glass (the sum of the wall thickness of the two vials). Therefore, the irradiated vial is only reached by 511 keV photons and lower energy photons originating in Compton scattering, the dominating process in water at this energy.

In order to assess the radiation field experienced by nanoflakes, we performed a simulation of the two-vial experimental set-up with the Geant4 toolkit [253, 254], aiming at determining the characteristics of the secondaries originating from the photon irradiation. In our calculations, we employed at a first glance the low-energy, analytical cross-section derived from the re-engineering of the PENELOPE (PENetration and Energy Loss of Positrons and Electrons) Monte Carlo code [80, 81]. In fact, the associated photon interaction model is known to be reliable for photon energies above 100 keV, while allowing a considerable saving of computational time [255]. Consequently, in the first calculation 10^9 were easily employed. A second simulation, giving access to a reliable nanometric representation of the secondaries has been run exploiting Geant4-DNA [254] and 10^6 photons

5.3.2 Monte Carlo simulation

5.3.2.1 Morphological effects

Following the Monte Carlo simulations of the radiation transport in our experimental set-up, we could figure out the effects of the radioactive ^{68}Ga decay on MoS_2 nanoflakes through the deriving high-energy annihilation photons.

Photons in the considered energy range interact, in water, mainly through Compton scattering. The counterpart to the relatively few, uniformly distributed scattering events originating directly from photons is the interaction pattern of the energetic electrons (delta rays) resulting in ionization events typical of inelastic photon scattering.

Figure 5.2 reports for both cases, water and air surrounding environments, the simulated energy spectrum of the electrons directly ionized by photons in the nanoflakes vial, Fig. 5.2(a), whose integral divided by mass is referred to as KERMA (Kinetic Energy Released in Matter) in radiation physics. The energy spectrum of the associated Compton photons is shown in, Fig. 5.2(b), where the contribution of the initial 511 keV photons, representing about half of the available primaries, has not been reported for illustration purposes.

The spectra of Figure 5.22 exhibit the typical behaviour of the incoherent Compton scattering, with the characteristic cut-off-like feature of the scattered secondary photon falling at about 1/3 of the primary 511 keV photon energy, 29% in this specific case, regardless the nature of the particular medium, water or air, where the scattering process occurs as predicted by the photon energy differential cross-section for Compton scattering [256].

A first clear difference between spectra calculated in water and air is the amount of Compton-generated electrons and secondary photons, larger in water with respect to air because of the much higher probability for the interaction of the primary photon to occur in the dense water medium compared to air, according to the interaction probabilities per unit path length ratio, approximately scaling as ρ_{water}/ρ_{air}.

A second very clear distinction is that both electron and photon energy spectra of Figure 5.2 shows two significantly different shapes: as a matter of fact, the electron

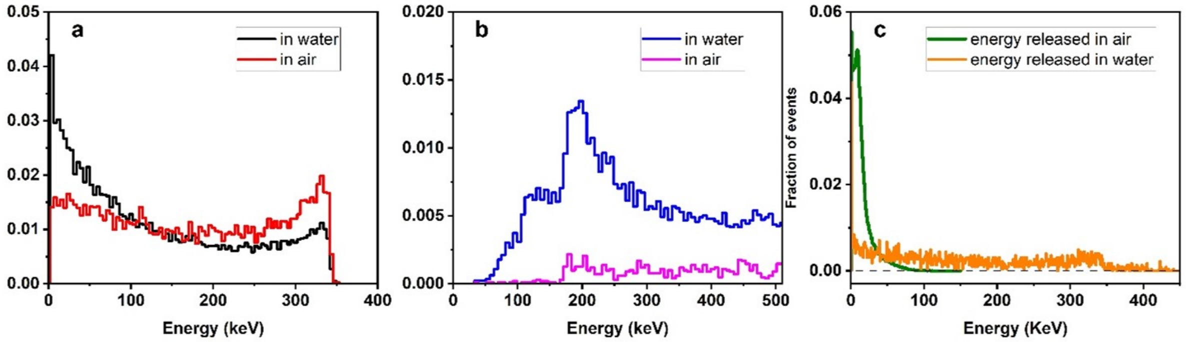

Figure 5.2: Energy spectrum of electrons ionized by primary photons in air and water medium. a. Energy spectrum of electrons directly ionized by primary photons in water (black), and air (red) originating either in positron annihilation; b. Photon energy spectrum of the Compton scattered component in water (blue) and in air (pink). c. Spectral distributions of energy released in air (black) and water (red) by each interacting photon

energy spectra in water there exhibit a much stronger component in the low energy ($<$ 50 keV) region of the spectrum as compared to air, whereas the secondary photons in water exhibit a consistent shoulder at around 150 keV, which is nearly absent in air. It is worthy noticing that while in a the areas under the black and the red curves are the same since they refer to overall number of secondary electrons emitted in both media, once a single Compton scattering event took place, in b the area under the blue curve in water is much bigger than the area under the pink curve in air since the number of photons that undergo Compton scattering in water is much bigger than in air.

Additionally, in our experiment the radiation interacting with nanoflakes, given their tiny concentration, is almost exclusively composed by secondaries produced in water by the 511 keV primaries and the lower energy photons originated in Compton incoherent scattering.

A quantitative determination of the radiation damage is generally given in terms of macroscopic dose to the irradiated sample. We have calculated the dose imparted to the vial containing the MoS_2 nanoflakes for comparing with what reported in [250], where a similar irradiation was performed in air ambient. Exploiting the Monte Carlo calculation a mean energy release per photon in the irradiated vial has been determined as

$$\overline{E}_{evt} = 3.4 \quad \text{KeV} \tag{5.4}$$

with a standard deviation $\sigma = 28.8$ keV. Considering a total number of decays N

$$N = \int \frac{dN}{dt} dt = \int A(t) dt = \tilde{A} = A_0 \tau \tag{5.5}$$

where A(t) indicates the activity at time t, A_0 the activity at t=0 and τ the radioactive decay time constant of the Gallium isotope, the mean energy, following all the decays, is given by

$$\overline{E} = \overline{E}_{evt} \,.\, A_0 \,.\, \tau \tag{5.6}$$

Considering that the vial has a volume V=1.96 cm^3, the mean energy released corresponds to a mean dose per event $\overline{D}_{evt}$ =2.78 × 10^{-13} Gy, that implies a mean dose, $\overline{D}_{evt}$ imparted to the nanoflake vial:

$$\overline{D}_{evt} = 0.484 \quad \mathrm{Gy} \tag{5.7}$$

The final imparted dose in air released by the same amount of energy would have been three orders of magnitude smaller, due to the density difference with water.

The differences occurring in the two media can also be understood looking at the distributions in Figure 5.2-c, where the spectrum of the energy released, respectively, in air and water by each interacting photon has been reported. Photons in water are much more likely to release more energy with respect to air. Photons also have a larger probability of interacting in water, due to its higher density.

Due to the very different mechanism of energy release in the two media, induced interactions with nanoflakes and consequent morphology of the induced damages turns out to be peculiar to the environment medium.

5.3.3 Nanoscopic analysis – AFM:

In order to analyse the nanoflakes morphology and possible modifications induced by direct and/or indirect interactions with ionizing radiations, Atomic Force Microscopy (AFM) was also employed. AFM measurements were performed in AC mode, so that in each scan both phase and morphological (height) maps were acquired. A typical outcome of AFM analysis is shown in Figure 5.3 for untreated and treated samples.

The main qualitative features of the acquired maps have been coupled with a quantitative analysis performed over AFM images. As found in AFM images [see Figure 5.3 d and e] and also in SEM images (Figure 5.6 of the following Section), structural damage over the edges, with holes and bulging of the edges, can be clearly appreciated.

In order to point out differences between irradiated and non-irradiated samples, a statistical analysis of morphological images has been performed on 2D flakes for each sample. The solidity, namely the ratio of a nanoflake area over its convex hull area, the perimeter, and the area for each nanoflake, automatically segmented with the procedure implemented in ImageJ software package, were extracted. Figure 5.4 reports the resulting statistical distributions (percentage of the total number of analysed nanoflakes of Solidity (a) and Form Factor (b) are reported, the latter being defined as (4 π × Area)/$(\mathrm{Perimeter})^2$ and measuring how much the shape of a nanoflake can be defined as circular. As revealed by this figure, nanoflakes Solidity and Form Factor are differently

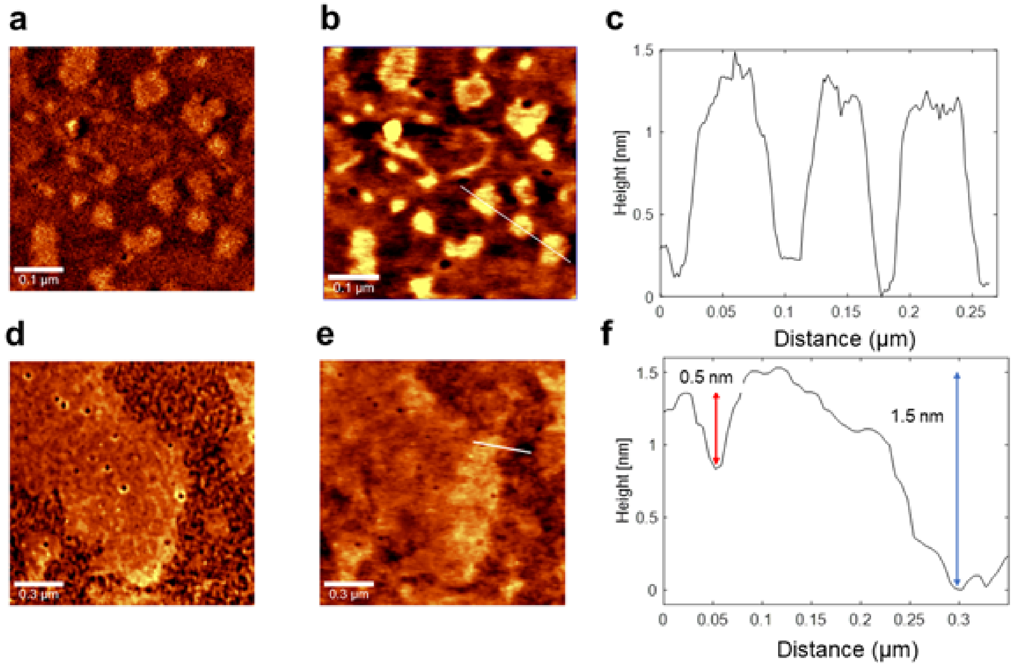

Figure 5.3: AFM analysis of untreated a-c and treated d-f 2D-MoS_2 nanoflakes deposited on a Si/SiO2 substrate. In particular, panel a,d report typical phase maps, while panel b,d report the corresponding height maps. Finally, panel c,f report the height profiles as read along the white line highlighted in b and e, respectively.

distributed in treated and untreated samples. the value of the main statistical parameters for the measured distributions are reported in Table B.3.

Intriguingly, both Solidity and Form Factor increase after irradiation, passing from 0.6 to 0.8 and 0.3 to 0.5, respectively. This suggests a more circular shape and larger convex hull area of the nanoflakes after treatment. This could be explained by the break and removal of the sharpest edges and corners of the nanoflakes because of high-energy radiation treatment at the most likely regions of the nanoflake to be fragmented by ionizing impact.

In order to characterise the impact of ionizing radiation also on the thickness of the 2D-nanoflakes, we have investigated their roughness by analysing the height parameter maps, i.e. the nanoflake thickness, from the AFM topographical images, before and after irradiation. To this purpose, based on the ImageJ software package (Details reported in Methods), we have analysed the statistical variable constituted by the average of the peak-to-valley height per each nanoflake of the probed population, named as the arithmetical mean deviation (Ra), which is a positive variable by definition. Histograms of the measured Ra are plotted in Figure 5.4-c, for treated and untreated cases, whereas we report in Table B.4 the related retrieved statistical parameters. The 100% "0 nm" statistical class of the untreated case indicates that our nanoflake production is fully flat, i.e. nanoflakes have the same thickness over their entire surface, with a 0-nm peak-to-valley value, which is an indication of the high quality of our LPE production resulting in a cut of the nanoflakes along a single crystallographic plane in the production process. Out of this 100% about 75% of the nanoflakes that are treated remains flat with 0-nm Ra value, whereas the residual 25% increases its average peak-to-value because of the impact with ionizing radiations.

Specifically, being the thickness of the MoS_2 single layer nanoflake ≈ 0.9 nm, we can deduce that most of the induced peak-to-valley excursion is in the range of 1-, 2- or 3-layer thickness. Just a few nanoflakes have a higher Ra value, between 7 and 9 nm, likely due to a possible little aggregation after irradiation, giving rise to a higher Min-Max excursion.

5.3.4 Microscopic analysis- SEM

The impact of irradiation in water onto MoS_2 nanoflakes morphology has been also analysed by means of Scanning Electron Microscopy (SEM). In Figure 5.5 a comparison of SEM images of treated and untreated MoS_2 samples is provided, showing significant differences. Panels a and b represent the distribution, with an irregular concentration of untreated 2D-MoS_2 nanoflakes deposited over a silicon substrate, b being the magnified (X 10) image of the rectangular area marked in a by a yellow border. The observed nanoflakes exhibit a typical sharp-edged appearance due to the exfoliation process, distorted rectangular shapes, coherently with the scientific literature [257, 258, 259]. The size of the nanoflakes is highly variable, ranging within 33 nm and 1333 nm. Panels c and d refer to irradiated specimen, where d represents the magnified image (X 10) of the rectangular area marked in c by a yellow border. Two are the main morphological modifications due to irradiation: i) the appearance of bulged rims together with the disappearance of the sharpest edges in the nanoflake borders and ii) the appearance of little holes on the nanosheet surface. The first modification implies an increase of the roundness in the flake border shape, in full agreement with the increase in the Form Factor reported in Figure 5.4. The second modification implies an increase of the nanoflake mean porosity and would also imply a decrease of the Solidity for the irradiated nanoflakes compared to the non-irradiated case, but its effect is counterbalanced and overtaken by the former modification that, besides the border shape, also affects the Solidity, implying a larger average convex area for the treated nanoflakes, because of the corners removal, in agreement with what observed in Figure 5.4. The size of nanosheet is highly variable, ranging within 33nm and 1000nm.

Morphology is, somehow, a low-accuracy tool for inspecting damages, since it does not evidence the driver of the changes underwent by the nanoflakes. So, to investigate the chemical nature of the modification induced with the irradiation, we carried out semi-quantitative EDS-WDS chemical analyses on untreated and treated 2D-MoS_2 nanoflakes. For treated nanoflakes EDS-WDS data indicate, for 15 analysis points out of 20, a higher Mo content together with a minor S content, with a crystal-chemical formula not corresponding to the starting MoS_2.Five nanoflakes of the analysed sample have regular chemical composition (not altered, in Table B.5) whereas fifteen nanoflakes have anomalous chemical composition. Two different reaction mechanism produce the effect of a higher content of Mo together with a lower of S: i) the molybdenite undergoes a structural modification and a vacancy is created in the S site; ii) the irradiation causes a chemical alteration of the molybdenite forming MoO_3 and SO_2 in an oxidizing

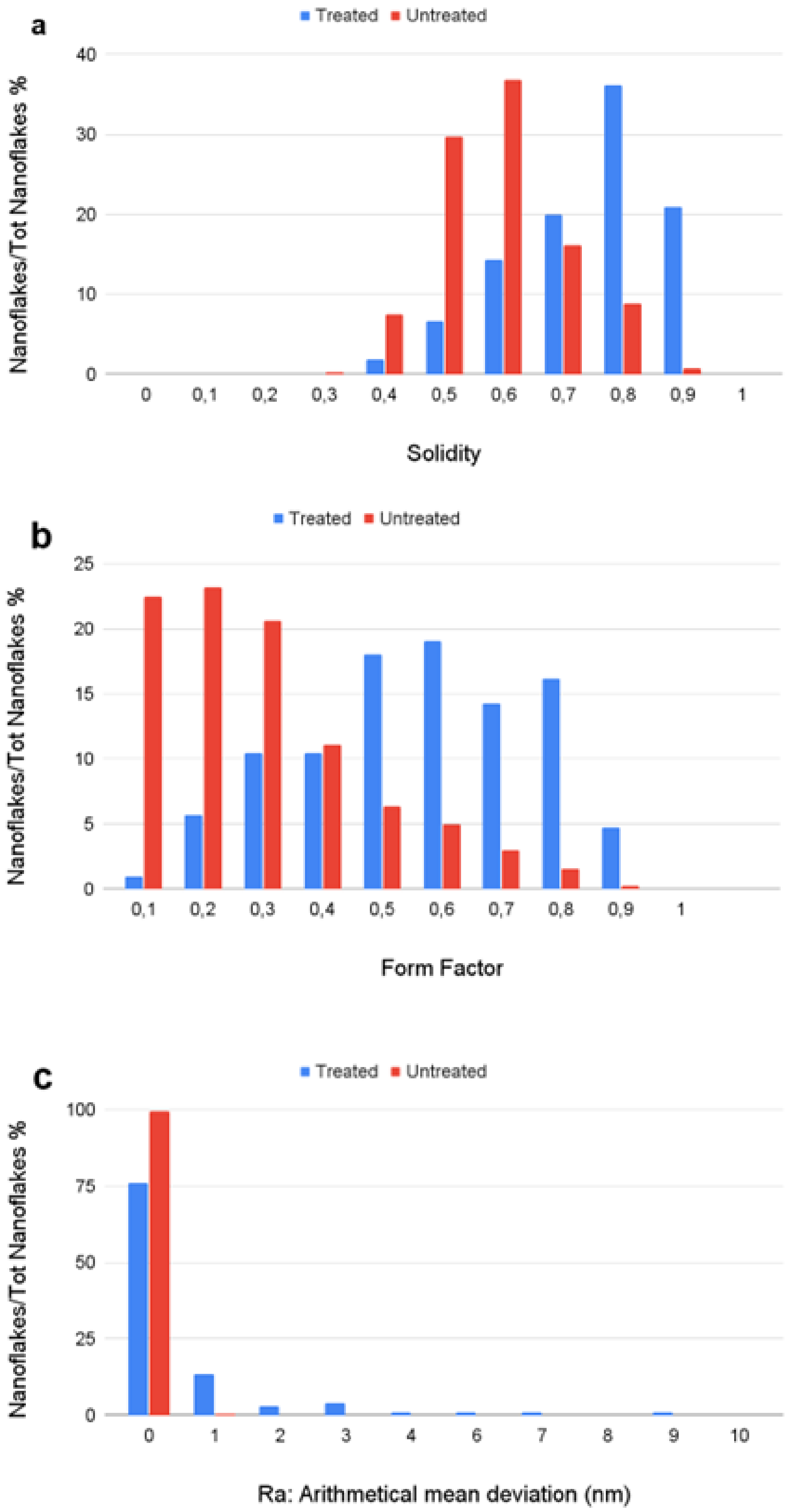

Figure 5.4: Statistical distribution of a Solidity and b Form Factor for untreated and treated cases. c. Histogram graph reports the distribution of the arithmetical mean deviation (average peak-to-valley per nanoflake) Ra values for untreated and treated cases.

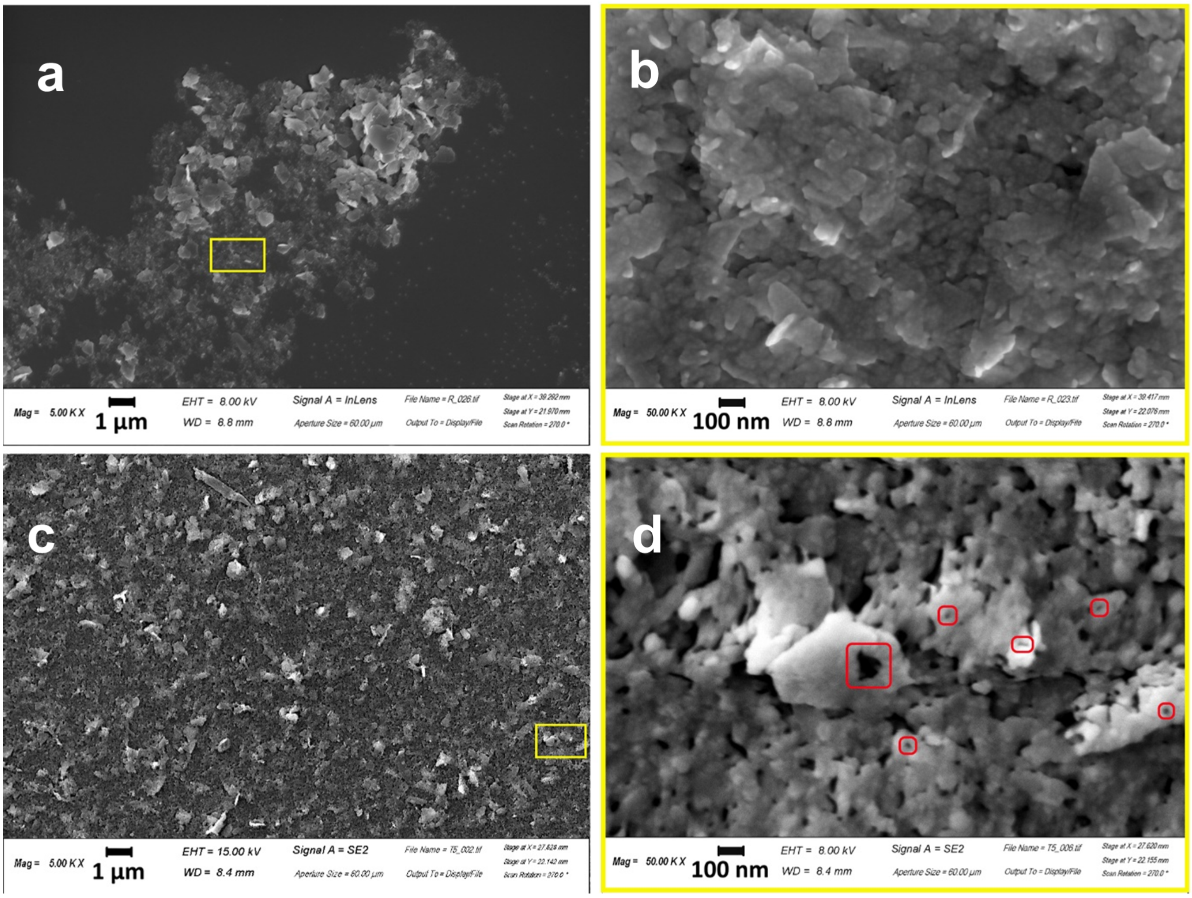

Figure 5.5: SEM morphological analyses of treated and not treated MoS_2 NSs. a-b. Represents the morphology of non-irradiated but exfoliated MoS_2 nanoflakes, b is the magnified (X 10) image of the rectangular area in a, marked by a yellow border and shows a pristine surface of flakes. c-d. Represent the irradiated MoS_2 sample with some structural damage, d being the magnified (X 10) image of the rectangular area in c, marked by a yellow border. In d rectangular regions indicated by red borders show details of irradiated samples enlightening the appearance of pores into the nanosheets, induced by radiation treatment.

atmosphere. Both mechanisms contribute to the observation, since ionization is known to produce atomic vacancies in crystalline structures, as discussed in the following, and the water solvent is mutated into a highly oxidised environment by the irradiation. The stoichiometric effects of both mechanisms on treated nanoflakes are reported in Table B.5.

5.3.5 Spectroscopy findings

5.3.5.1 Raman Spectroscopy:

Figure 5.6 compares selected Raman spectra obtained for untreated (trace a) and treated (trace b) flakes. Trace a clearly exhibits the E^1_{2g} and A_{1g} modes, which dominates the 250-500 cm^{-1} spectral region of 2D-MoS_2

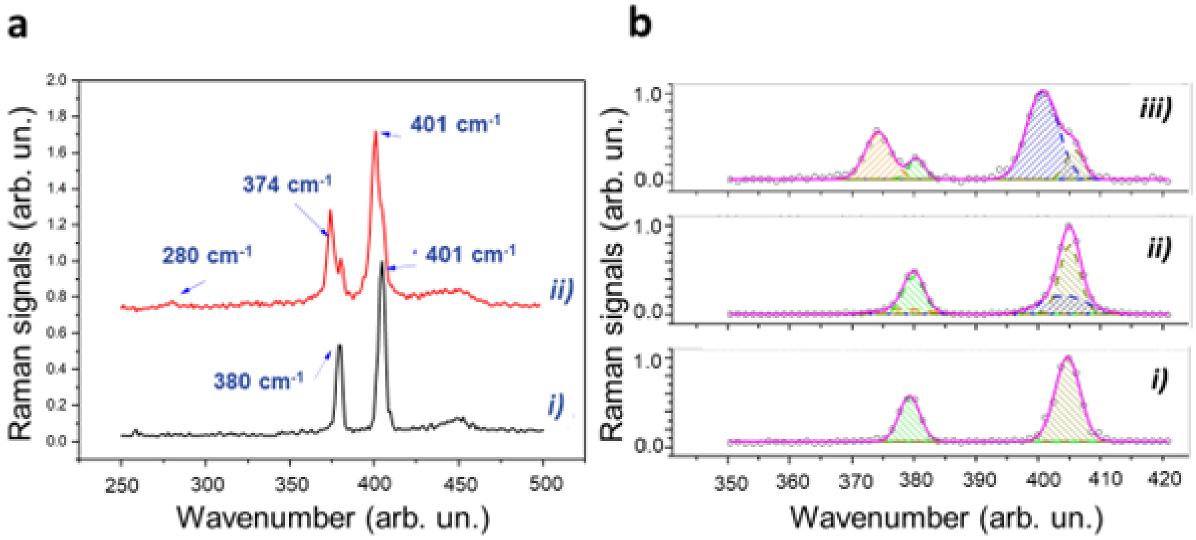

Figure 5.6: Characteristic Raman spectra of exfoliated treated and not treated MoS_2 NSs. a Comparison of selected Raman spectra obtained for not irradiated (trace i) and irradiated (trace ii) flakes. b: Outcomes of the fitting procedure of 2D-MoS_2 bands in the 350-420 cm^{-1} spectral region. In particular, panel i) corresponds to the spectrum from untreated flakes, while panel ii) and iii) correspond to spectra obtained from irradiated flakes acquired in the inner areas of the flakes (panel ii) and near the border (panel iii). In all the cases, the solid pink lines correspond to the fitted curves, while dashed areas highlight the contribution of the different peaks.

Our Raman analysis revealed that following irradiation, significant changes took place in our nanoflake sample. The most relevant change relies on the apparent splitting of both E^1_{2g} and A_{1g} modes, resulting by the rise of new, red-shifted peaks. Moreover, the rise of a new feature around 280 cm^{-1}, ascribed to the E1g mode, can also be appreciated as well as a slight broadening of the band around 450 cm^{-1}, due to a combination of a longitudinal acoustic mode (LAM) and an optical mode (A2u) [260]. Intriguingly, although such spectral changes exhibit strong point-to-point variations, they are clearly correlated, so that the peak at 280 cm^{-1} is observed when the wider splitting is present.

In particular, the most relevant spectral changes are usually found at the flakes (or flake cluster) border, while far from the border only a slight asymmetry of E^1_{2g} and A_{1g} modes can be seen, what confirms the observation reported in AFM and SEM sections concerning the strong impact of the treatment right on the border of the nanoflakes. To quantitatively describe these changes, Raman spectra corresponding to these conditions were analyzed by a multi-peak fitting in the 350-420 cm^{-1} spectral range. The outcomes of this analysis are shown in Figure 5.6-b.

Here, panel i) reports the fitting of the two E^1_{2g} and A_{1g} bands by two Gaussian curves for of the Raman spectrum corresponding to the untreated sample, while in panels ii) and iii) fitting was done with four Gaussian peaks of spectra acquired in irradiated samples at the center (panel ii) and at the border (panel iii). The main features emerging from this analysis can be summarized as follows.

- Spectra of irradiated samples can be described as overlapping contributions of unaffected E^1_{2g} and A_{1g} modes and red-shifted E^1_{2g} and A_{1g} modes. In particular, a red-shift of 4.2 and 4.0 cm^{-1} was estimated for the E^1_{2g} and A_{1g} peaks, respectively, for the spectrum in panel c), while a reduced shift of 1.5 and 1.2 cm^{-1} was estimated for the case in panel ii);
- The FWHM corresponding to shifted modes is more than doubled with respect to unaffected modes;
- The relative strength of the two initial peaks is roughly conserved for red-shifted modes.

In order to understand the sample modification induced by γ-rays irradiation at the basis of the observed spectral changes, some relevant issues have to be highlighted.

First of all, according to literature, both induced strain and doping are mirrored by spectral shift of E^1_{2g} and A_{1g} modes. In particular, if the changes are induced by strain, the two modes shift in the same direction, with compressive strain causing a blue shift and tensile strain a red shift [261]. On the other hand, doping mainly causes changes for the A_{1g} mode, while E^1_{2g} mode mode is much less affected. As a matter of facts, p-doping leads to a blue-shift A_{1g} mode and an increase of its FWHM, while a red shift and a spectral narrowing is associated to n-type doping [262].

Gamma irradiations of 2D-TMDs has been previously investigated in air for both MoS_2 and WS_2 flakes. In the first case, authors observed a red shift of both E^1_{2g} and A_{1g} modes, which increases with radiation dose. Notably, a ~ 3 cm^{-1} and ~ 3.5 cm^{-1} was observed at a 1000 kGy irradiation dose. Such outcome was ascribed to an increase of interlayers spacing (as confirmed by XRD and TEM analysis), leading to a weakening of the van der Waals interlayer interaction and therefore to a softening of the two Raman modes [263]. On the other hand, it was reported that γ-irradiation of monolayer WS_2 leads to a blue shift of the A_{1g} peak and an increase of the intensity ratio between A_{1g} and E^1_{2g} modes, interpreted in terms creation of vacancies and effective induction of p-doping [262].

However, more complex and intriguing phenomena can take place for MoS_2 irradiation in water, due to the presence of γ-generated ROS species, as discussed in the Conclusions. From our Raman data, although it is not possible to exclude some contributions from doping (e.g. electron doping), it turns out that irradiation leads to a significant weakening of interlayer van der Wall interaction. It is worth noticing that the observed effect is much more pronounced with respect to γ-irradiation of dry sample reported in [263]. A reasonable cause of that could be related to the intercalation of γ-generated species, eventually recombining in the interlayer space. It is, in fact, well assessed that ions are able to intercalate into the van der Waals gap through the edges of the 2D flake, causing wrinkling and distortion. Recently, it was also demonstrated that ions can also intercalate through the top surface of few-layer MoS_2, even reversibly. Previous investigations demonstrated the possibility to check 2D-MoS_2 intercalation by monitoring the frequency shift of E^1_{2g} and A_{1g} modes bands. Particularly, it was proved [264] that O_2 intercalation in MoS_2, obtained by a soft-plasma treatment, leads to a weakening of these modes. A red-shift of 0.7 and 0.2 cm^{-1} was observed on average for E^1_{2g} and A_{1g} bands, respectively, although strong fluctuations are present in the acquired spectra. In that case, authors speculated that oxygen molecules may be formed in the interlayer space after O_2^+ ions intercalation, being successively stabilized via the van der Waals interaction with the adjacent MoS_2 monolayers. A similar intercalation mechanism can likely take place in our experimental condition, considering the large amount of oxygen ions produced by γ-irradiation of water (see Monte Carlo Simulations and Conclusion section). In this frame, the relevant broadening of red-shifted peaks could reflect the heterogeneity of the process occurring in our case. Clearly, ions interaction with MoS_2 also introduce a certain amount of structural disorder, that are mirrored by the appearance of the E_{1g} mode (forbidden in back-scattering experiments) and the broadening of the band at 450 cm^{-1}.

5.3.5.2 X-ray Photoelectron Spectroscopy (XPS)

The energy provided to MoS_2 samples through sonication and subsequent irradiation with γ-photons produces changes in the chemical composition of surfaces as assessed by XPS. In Figure 5.7, we report XPS spectra of the Mo 3d band [Figure 5.7-a for untreated sample and treated] and the S 2s band [Figure 5.7-b for untreated and treated sample]. The process of sonication itself, indeed, proved to produce a certain degree of oxidation registered as changes both in the Molybdenum and in the Sulphur spectra [265]. After deconvolution the Mo 3d spectra of non-irradiated pristine bulk powder consists of one singlet and one doublet in which S 2s, $3d_{5/2}$ and Mo $3d_{3/2}$ photoelectron lines corresponds to Mo^{4+} an S^{2-} environment. The binding energies (BE) of the pristine bulk powder samples are 226.83, 229.51, 232.64 eV [250], Further values are reported in Table B.6 together with the quantitative (percentage) surface composition of samples after deconvolution of the S and Mo envelops, separately normalized into the 159-173 eV - graphs a and b - and 225-239 eV.

As seen in Figure 5.7, after irradiation, a general important finding is the change in the observed BE, which corresponds to the higher shift in the deconvoluted spectra maintaining Mo^{4+} environment. In case of Mo, the shift in the BE can be attributed to the displacement of S atom because of the direct interaction of incoming γ-photons or the generated electrons after their absorption which, of course, comes mostly under the category of Compton scattering of γ-photons. Moreover, our experimental setup, in a water environment, implies an enormous amount of oxygen presence resulting in the oxidation of Mo 3d orbitals with a considerable change. The MoS_2 sample displays the typical peaks of Mo IV, with a characteristic 3d doublet at 229.5 and 232.6 eV, respectively, across all samplings (see Table B.6).

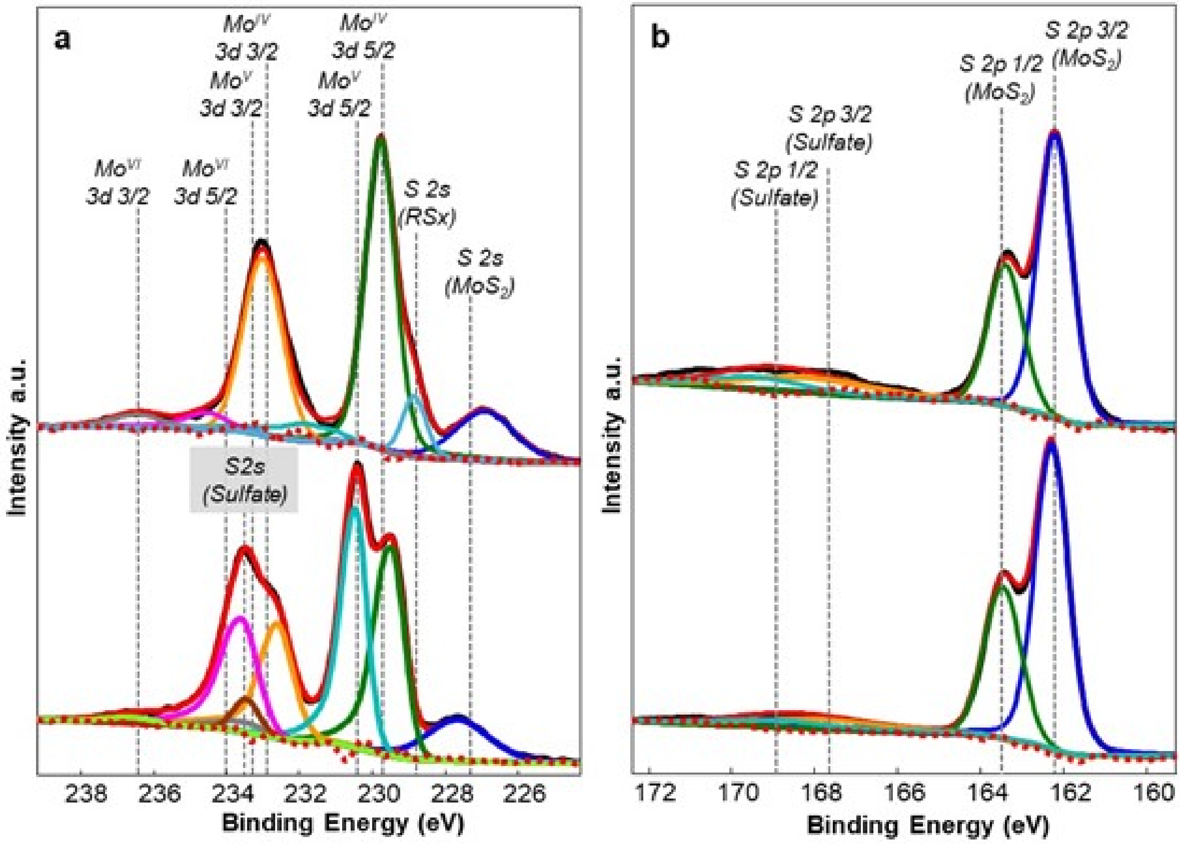

Figure 5.7: XPS spectra of MoS_2 exhibiting different oxidized species of Molybdenum and Sulphur atoms. a. Mo 3d band for the untreated case, Mo 3d band per the treated case, b. S 2p band for the untreated case, S 2p band for the treated case.

The current exfoliation process generates oxidized species on the surface of the material under examination. In fact, the sonication process introduce $(SO_4)^{-2}$ resulting in the decrease of the percentage of MoS_2 from 66.67 to 61.75 as reported in Table B.6. The sulfate accounts for 4.91% of the whole composition, which increases after the irradiation to 6.51% (Table B.6) [266]. The formation of oxysulfide clusters ($Mo_{IV}S_yO_x$) is due to the air contamination and exfoliation process [267] producing peaks that can be attributed to Molybdenum VI MoO_3 (above 232 eV and 235 eV). Upon inducing oxygen defects Mo6+ ions are reduced to Mo5+ confirming the formation of MoO_3 [268, 269]. Indeed, reducing the size to the nanometric level, during sample fabrication, induces vacancies within the crystal lattice, resulting in edge effects and discontinuities that are more susceptible to oxidation [270, 271]. Additionally, species with a BE around 228.47 eV, in Figure 5.7-a, are attributable to the adsorption of organosulfur molecules grafted by the exfoliation process. These are identified as interfering species that form in materials subjected to high kinetic energy processes [250].

Regarding the sulfur signals, the S 2p signals of the present MoS_2 are recognizable as a doublet around 163 eV across all sampling as shown in Figure 5.7-b while an S 2p fraction of sulfate above 168 eV is recognizable as an effect of oxidation attributable both to the fabrication process and radiolysis. The S 2p spectrum of nonirradiated MoS_2 consists of a single doublet, in which the S $2p_{3/2}$ and S $2p_{1/2}$ photoelectron lines depict the S^{2-} sulfide environment of MoS_2 as shown in Table B.6. The irradiated sample shows another doublet at higher BE in which the S $2p_{3/2}$ and S $2p_{1/2}$ photoelectron lines depict the corresponding values at 162.4 and 163.5 eV as shown in Figure 5.7-b. The reason for this shift at higher BE could be due to the formation of organosulfur species having specific bonds with Oxygen and Carbon atoms that can be ascribed to a decrease in the kinetic energy of the S atoms in the given medium relating it to the formation of bonds with Oxygen and Carbon. The new action mechanism of bond formation with the O and C atoms results in an enhancement of effective nuclear charge over the Mo and S atomic orbitals, whereby reducing electron density in the S atom. The observed BEs for S 2p orbitals are in good agreement with the literature because the thiol and aliphatic sulfide species exhibit BEs in the 162-164 eV range. Interestingly, after irradiation with the given dose, the BE of S 2p orbital increases by few eVs which could be related to the effect of generated radical species such as OH, H_3O^+, and H_2O_2 as discussed in the following, facilitating the oxidation of S atoms to produce SO_4^{2-}species.

As the most striking novel finding resulting from XPS analysis we observe that radiolysis occurring in our experimental setup, produces the massive appearance of the oxidized Molybdenum V fraction. Molybdenum V, which an unstable oxidation state of Molybdenum and is fully absent in the samples before irradiation, exhibits after irradiation a new characteristic big doublet peaked at 230.45 eV - 25.37% of the entire surface composition in the Mo spectral band- and at 233.58 eV - 17.0% of the entire surface composition- as shown in Figure 5.7-a. The presence of MoV in previous experiments of Mo nanoflakes exposed in air ambient was much lower and ascribed to the action of residual humidity in air [267] or to a treatment with an excess of H_2O_2. Thus, for the first time to the best of our knowledge the change of the oxidation state of Mo to the unstable MoV into Molybdenum-based nanomaterials is induced by irradiation of samples with γ-photons, the mechanism of which, by the way, agrees with what found in [272], where this is due to the presence of a high concentration of hydrogen peroxide. Peculiar to our experiment is that the high concentration of H_2O_2 is due to the action of γ-photons onto the water ambient. Thus, nanoflakes subjected to irradiation present a distinctive subdivision of the Mo fraction into MoIV and MoV species. As also indicated by EDX measurements, the surface is not homogeneous and two distinct populations of MoIV and MoV are evident, while the MoVI fraction becomes less significant. The peak at a BE of 233.45 eV is also noteworthy, which is to attribute to Sulfur 2s as sulfate, likely due to some sulfate ions remaining, coordinated, or trapped in the lattice of the nanoflakes surface as shown in Figure 5.7-a. The atomic surface composition in weight% for pristine MoS_2, MoS_2 sonicated 2D-nanoflakes, and treated 2D-nanoflakes is reported in Table B.7.

5.4 Discussion

Using the radiochemistry models in Geant4 [273, 274], we made some quantitative evaluations concerning the production of species associated with water radiolysis, affecting the nanostructures during and after the so-called "chemical stage" of the irradiation, lasting from 1 ps up to 1 μs after the physical interaction. We calculated the time-dependent radiolytic yields G(t), defined as the number of molecules produced for a given radiolysis species, at a given time, and normalized to 100eV of imparted energy:

$$G = \frac{N(t)\,.\,100}{E\,(eV)} \tag{5.8}$$

In Figure 5.8, the time evolution between 1 ps and 1 μs of the radiolytic yields is shown for six different species originating in water radiolysis, namely H_3O^+, OH, eaq, H_2O_2, H and OH^-. Literature dealing with oxidation processes in MoS_2 [234] suggests that among these the two most active species in changing the chemical nature of the compound adding oxygen could be the hydroxyl radical, OH^-, extremely reactive and immediately affecting the MoS_2 nanostructures, and the hydrogen peroxide, H_2O_2, more stable although spontaneously dismutating to produce oxygen and water. Then, the indirect effect of the irradiation on the nanoflakes would likely consist of an oxidation of their surfaces.

The most interesting feature to observe in Figure 5.8 is the evolution of G(t) for H_2O_2. At later times, from ns to μs, we calculate a massive formation of hydrogen peroxide mainly due to the interaction of generated lower energy electrons with water. This is shown by the behaviour of the green, blue, yellow, and magenta curves in the H_2O_2 plot, with energy comprised in the 0.3 – 1.5 keV window. At these later and therefore final stages of radiolysis, the H_2O_2 G value reached by these lower energy electrons is about double than that reached by the higher energy electrons of the cascade radiolytic process. This implies a very important difference in the radiolysis induced by 511 keV γ-photons in water from that induced in air ambient. In fact, in Figure 5.2-a our calculation shows a much higher production of lower energy electrons in water rather than in air, due to radiolysis of the surrounding medium. These combined calculations

imply the production of a very much higher concentration of H_2O_2, as a result of the irradiation in water as compared to air context, with consequent specific oxidation mechanisms of MoS_2 nanoflakes

5.5 Conclusion

The interactions of gamma photons, originated from positron annihilation, on 2D-MoS_2 nanoflakes dispersed in water have been carefully and deeply studied. Very interestingly, our findings demonstrate that in addition to the direct interaction between high-energy photons and nanoflakes, the indirect interactions between nanoflakes and radiolysis prod-

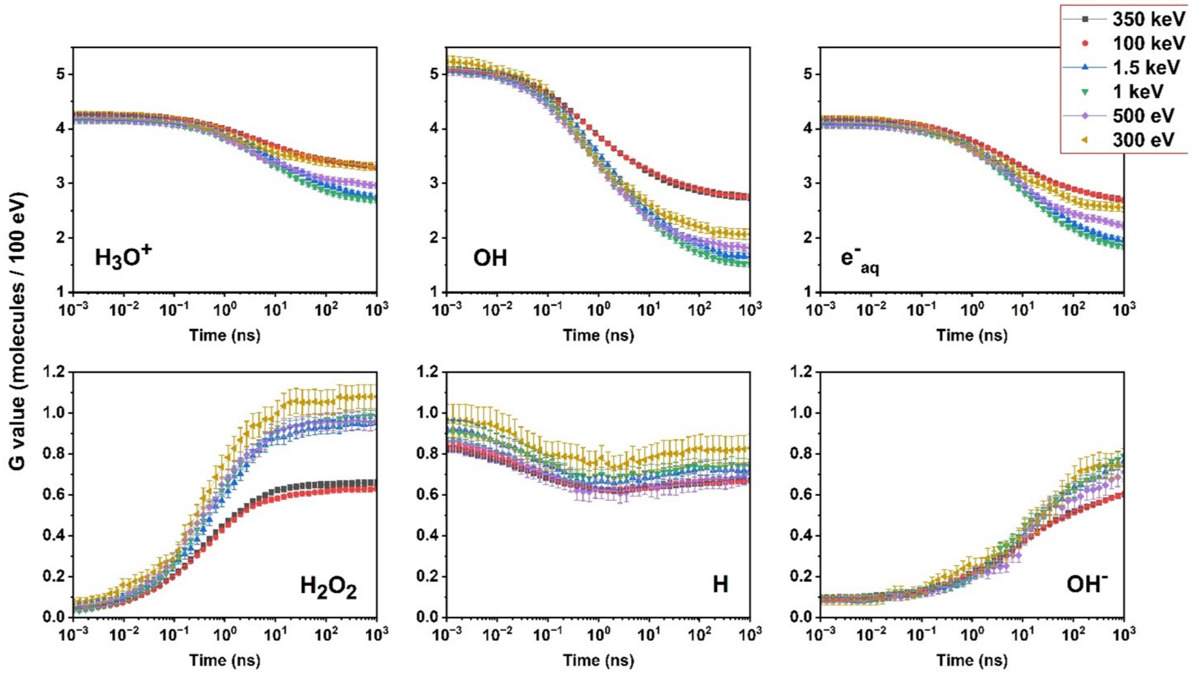

Figure 5.8: Calculated G factor evolution in time for the main hydrolytic species (indicated in each panel), between 1 ps and 1 μs, reported along with its standard deviation for each calculated point.

ucts generated in water by γ-photons play a fundamental role, which is novel and peculiar to the water environment. The interacting photons induce the generation of various reactive oxygen species in water solution exhibiting a very interesting radiochemistry that affect the MoS_2 nanoflakes. The key factor for the structural modification of the MoS_2 nanoflakes is to be found in the species formed in water through radiolysis, that are extremely reactive and can induce oxidation onto the exposed surface of the flakes. In fact, ionizing radiation in air can similarly induce the formation of reactive species, but their oxidative power is by far smaller than that associated with radicals found in water, for both their resulting concentration and chemical nature.

A radiation transport Monte-Carlo simulation, developed for our experimental conditions, allowed determining the main mechanisms driving the morphological and spectroscopical changes of the irradiated nanoflakes.

Raman spectroscopy analysis of the samples, exhibiting new vibration modes, suggest the role of oxygenated species, originated by massive water radiolysis, in the impact on the irradiated samples. The significant changes observed in the treated samples, giving rise to new red-shifted peaks around 280 cm^{-1} which is ascribed to E_{1g} mode, supports the fact that irradiation of 2D-MoS_2 nanoflakes resulted in significant weakening of interlayer van der Walls interactions. AFM and SEM-EDS analysis clearly showed some structural damage over the edges and significant change in the chemical composition of the Mo and S species. On the other hand, XPS analysis strongly supports and corroborates the whole characterization analysis by evidencing the peculiar effect of irradiation on 2D nanoflakes. XPS analysis indicates that in water environment a massive presence of oxygen coupled to the treatment with 511 keV photons results in a considerable oxidation of Mo 3d.

Ther AFM and SEM analysis of the treated nanoflakes reveals that the treatment induces in 2D nanoflakes vacancies within the crystal lattice, resulting in edge effects and discontinuities that are more susceptible to oxidation. These effects are clearly confirmed by XPS corroborating an oxidation of the Sulfur signals that exhibit a higher shift in the BE of S 2p orbital. A deep morphological and statistical analysis of the treated versus the untreated nanoflakes reveal a more circular shape and larger convex hull area of the nanomaterials after treatment. As a particularly novel and intriguing finding, peculiar of the irradiation of samples in water environment, XPS and SEM observations coherently demonstrate that, mostly because of the indirect interactions with the new chemical species formed under water radiolysis, the Molybdenum oxidation state into the nanoflakes is massively changed from the stable +4 and +6 state into the rarer and more unstable +5.

Hence, our results open up a very exciting route to explore the effect of high-energy irradiations on the liquid phase exfoliated 2D materials dispersed in water, in view of their intriguing applications in the field of radiotherapy and oncology. Our findings are particularly relevant for many types of applications of 2D-MoS_2 from biological and medical studies, where they highlight possible consequences of radiation-based therapies and diagnostics in patients who are assuming drugs or contrast agents containing 2D-MoS_2, to aerospatial biomedical applications of 2DMs taking place on space station or satellites.

5.6 Material and methods

5.6.1 Exfoliation of MoS_2 powder

The starting commercialized bulk MoS_2 powder (Sigma Aldrich, 69860, particle size 6 μm, density 5.06 g mL^{-1} at 25 °C) was exfoliated in pure water as a solvent using a tip sonicator (Bandelin Ultrasound SONOPLUS HD3200, maximum power 200 W, working frequency 20 kHz, KE-76 probe, with an ice-water bath controlling the temperature of the dispersion.

The experimental procedure was adopted from our previous studies but with a little modification [145]. MoS_2 bulk powder with initial concentration of 5 mg/mL was pre-treated by manual grinding with a pestle-mortar for 50 minutes. After then, it was exposed to high frequency ultrasonic waves in a tip sonicator and exfoliated for 210 minutes with a running amplitude of 40% and with pulse mode 10 s On and 10 s Off. Before the sonication step, the immersion of the colloid was done in a broad quartz glass bottle with flat end to maximize the interaction of high sonic jets and bubbles with the stacked bulk MoS_2 material. Santos et al. has nicely explained the concept of dead zones for an efficient exfoliation which in our case was very helpful in choosing a particular shape of the glass tube for the sonication purpose. The larger the contact area of the probe with the material the more effective the exfoliation and the transfer of acoustic energy and ultrasonic intensity through the probe [275]. The obtained polydisperse 2D-MoS_2 dispersion was separated into fractions with varying <L> and <N> by controlled centrifugation step. The post sonication step, which is the liquid cascade centrifugation, was employed to obtain the 2D nanosheets with controlled size and thickness [196, 275]. Successive stepwise controlled centrifugation steps were carried out (Megafuge 16 centrifuge, a swinging bucket rotor centrifuge device) at 100 g and 1000 g for 60 minutes each to analyse the supernatants. The as obtained 2D MoS_2 NSs was first centrifuged at 100 g for 60 minutes and the resulting sediment was discarded because of the mostly unexfoliated material and the supernatant is shifted to higher centrifuge step of 1000 g for 60 minutes. After this step, the final supernatant was stored at 4° C, used for further characterizations and for the Irradiation purpose.

5.6.2 Description of the vial with Ga86 radiation source preparation

68Ga-chloride has been eluted directly from a germanium-68 (^{68}Ge) /gallium-68 (^{68}Ga) generator (Eckert and Ziegler Radio pharma GmbH) with a 270.93-day half-life of the parent nuclide ^{68}Ge. The ^{68}Ge/^{68}Ga generator is designed to elute all of the available ^{68}Ga activity in a vial with a volume of 5 ml of sterile ultrapure 0.1 mol/l hydrochloric acid. Eluted activity has been measured right after elution with Capintec^{TM} Dose Calibrator.

5.6.3 Monte Carlo Simulation

GEANT4, short for Geometry and Tracking 4, is a freely available Monte Carlo Simulation toolkit developed in C++ with an object-oriented approach [253, 254]. It originated from the collaborative efforts of over 100 researchers under the RD44 collaboration. In this study, we employed the toolkit to simulate the two-vial experimental set-up of the MoS_2 NSs. The geometry of the system was modelled assuming a distribution of nanometric flakes in line with the concentration employed. At a first stage the interaction of the 511keV and Compton photons with the nanoflakes vial has been reproduced employing the low-energy, analytical cross-section derived from the re-engineering of the PENELOPE (PENetration and Energy Loss of Positrons and Electrons) Monte Carlo code [80, 81] that allows a considerable saving of computational time while remaining reliable for photons originating in the vial with the radioactive Gadolinium from the positron annihilation. Subsequently, to access the track structure of secondary electrons, another simulation campaign has been carried on with the Geant4-DNA [254] package and 10^6 photons. The Geant4-DNA project was initially launched by the European Space Agency to study the biological effects of radiation during extended manned space missions. The associated software packages include the refinement of electromagnetic physics models to accurately represent interactions down to the eV energy scale, and the integration of water radiolysis processes to account for the generation of oxidative radical species, in order to simulate both direct and non-direct ionizing radiation biological effects at the DNA level in nanodosimetric studies [276].

Using the radiochemistry models in Geant4-DNA [273, 274] we calculated yields of different species deriving from water radiolysis during and after the so-called “chemical stage" of the irradiation, lasting from 1 ps up to 1 μs after the physical interaction. To this end, the irradiation of a millimetric water cube with a scaled flakes distribution has been simulated, employing electrons with energies ranging from 300 eV to 350 keV. The resulting time-dependent radiolytic yields G(t), representing the number of molecules produced for a given radiolysis species normalized in energy, has been calculated for H_3O^+, OH, eaq, H_2O_2, H and OH^-.

Chapter 6

Discussion

The research within this thesis explores the complex connections between the fabrication of 2D transition metal dichalcogenide (TMDs) nanosheets, their fundamental properties in diverse environments, and the range of potential applications they offer. A strong emphasis on utilizing biocompatible solvents throughout the research highlights the commitment to exploring the potential of TMDs nanosheets within sensitive biological and biomedical contexts. The findings of three interconnected studies converge to illustrate the power of liquid-phase exfoliation for nanosheets production. The influence of different biocompatible solvents on nanosheets stability and behavior is demonstrated, along with the potential for TMDs nanosheets modification under radiation to suit specific purposes, as well as interaction with different bacteria.

This work highlights the versatility of TMDs nanosheets. Their unique electronic and optical properties and large surface area-to-volume ratios make them exceptionally promising candidates for various fields. The choice of fabrication method and, crucially, the solvent environment directly affect TMDs properties. The interplay between these parameters offers a path towards designing nanosheets for specific applications by tuning their stability, morphology, potential for functionalization, and interactions with biological or inorganic interfaces.

A significant takeaway of this research is the importance of considering biocompatibility from the earliest stages of materials development. The theoretical analysis of nanosheets-bacteria interactions within different solvents emphasizes how critical parameters like dielectric constant and surface charges are for governing nanosheets behavior in biological settings. This underlines the fact that moving away from toxic solvents is not merely a desirable shift, but one choice that can directly impact the functionality and applicability of the developed materials in biomedical contexts.

6.1 Synthesis of Key Findings

The three studies presented in this thesis provide a multifaceted analysis of TMDs nanosheets fabrication, properties, and applications. Here, I profoundly present the key findings and how they intertwine:

6.1.1 Interdisciplinary Insights from Bacterial Interactions

In Chapter 3, we explored the interactions between MoS_2 nanoflakes and bacterial strains by applying an extended DLVO model, offering valuable insights into the differential behavior of Gram-positive and Gram-negative bacteria. Considering the influence of solvent effects and bacterial characteristics, the study reveals nuances in the electrostatic repulsion and van der Waals interactions, shaping the overall interaction energy landscape. The model predicts significant differences in these forces across Gram-positive and Gram-negative bacteria. These differences are attributed to the composition and structure of bacterial membranes. The distinctly lower predicted electrostatic repulsion with E. coli is particularly notable. This theoretical framework informs TMDs' design for biological applications and highlights the necessity of choosing solvents based on the intended biological targets. These findings not only advance our understanding of bacterial-nanomaterial interactions but also lay the groundwork for subsequent investigations in biomedicine and environmental science.

6.1.2 Sustainable Dispersion Techniques and Characterization

Expanding on the insights from Chapter 3, the experimental investigation in Chapter 4 into cyrene as a biocompatible solvent for TMDs exfoliation demonstrates its viability for yielding high-quality nanosheets, corroborated by detailed characterization. Here we focus on the dispersion and characterization of MoS_2 and WS_2 in the green solvent cyrene. Employing a suite of experimental techniques, LPE using ultrasonication followed by centrifugation, allows for successful production of high-quality TMDs nanosheets. This is validated through multi-technique characterization of the produced nanomaterials including zeta-potential analysis, DLS, UV-vis, AFM, Raman, and SEM. The study provides a detailed characterization of the nanoflakes' morphology, stability, and thickness. While cyrene's characteristics, especially its viscosity, present challenges in the exfoliation process, the results highlight the potential of this solvent as a greener alternative to more commonly used but often hazardous solvents. The application of the DLVO theory to interepret the experimental findings further enhances the understanding of dispersion mechanisms, emphasizing the importance of sustainable solvent selection in achieving efficient dispersion and stability. The result is animpactful step towards broadening the range of solvent choices available for TMDsfabrication, specifically in applications where biocompatibility and reduced environmental impact are crucial.

6.1.3 Therapeutic Applications and Radiation Response

Exploration of TMDs nanosheets within a water environment under radiation reveals their potential for controlled modification. In Chapter 5, the focus shifts to the response of MoS_2 nanoflakes to high-energy photon irradiation in a water medium, with implications for radiotherapy and oncology applications. Leveraging LPE techniques and theoretical modeling based on the PENELOPE Monte Carlo code, the study investigates the structural and chemical changes induced by gamma photon irradiation. By connecting experimental observations with theoretical predictions, the research provides valuable insights into the complex interactions between MoS_2 nanoflakes and gamma radiation, highlighting the potential consequences for patients assuming drugs or contrast agents containing water-dispersed 2D nanoflakes, when possibly trated with gamma photon irradiation. The observed radiation-induced changes in nanosheets structure, as evidenced by alterations in chemical bonding and the generation of reactive oxygen species, have profound implications for biomedical applications.

6.2 The Significance of Integrated Findings

These three studies do not merely stand in isolation. They represent a cohesive approach demonstrating a deep understanding of fundamental interactions that are peculiar of 2D-nanomaterials and a drive towards greener fabrication methods. While each study addresses distinct aspects of TMDs nanosheet behaviour in various contexts, they are inherently interconnected, providing a comprehensive understanding of the behavior and potential applications of these nanomaterials.

The emphasis on biocompatible solvents throughout this thesis exemplifies the importance of a holistic view of nanosheets fabrication. It encourages us to move beyond solely considering material in isolation and instead consider its broader context—its fabrication, potential applications, and ultimate impact. By fostering this mindset and building a strong foundation of knowledge, we can navigate the development of TMDs and other next-generation materials in a manner that balances functionality with long-term responsibility.

The theoretical modeling informs the choice of solvents for fabrication, highlighting that biocompatible options are not merely desirable but can fundamentally affect material behavior. In turn, experimental results validate the importance of these considerations by demonstrating success with the biocompatible solvent cyrene. Also exploring nanosheets responsiveness to gamma radiation within a biocompatible environment provides the foundation for exploiting these phenomena in biomedical fields.

A notable aspect across all three studies is the consistent utilization of both experimental techniques and theoretical models to explain the behavior of 2D nanoflakes. LPE technique using ultrasonication followed by centrifugation, is employed to fabricate uniform nanoflakes in green solvents, emphasizing sustainability and biocompatibility. Additionally, DLVO (Derjaguin, Landau, Verwey, Overbeek) theory serves as a foundational framework for analyzing the interactions between nanoflakes and biological entities, providing insights into the underlying forces governing these interactions.

6.2.1 The Crucial Importance of Biocompatible Solvents

This thesis underlines biocompatible solvents' pivotal role in TMDs nanosheets fabrication and their translation into diverse applications. Moving beyond traditional fabrication routes that often rely on toxic solvents, we lay the groundwork for a new paradigm in nanosheets fabrication where safety and environmental impact are prioritized alongside functionality. Here are the reasons why this shift is so crucial:

- Shaping nanosheets-Biological Interactions: Our theoretical modeling highlights that solvents are not merely passive mediums during fabrication, but rather active players in influencing nanosheets behavior. Parameters like dielectric constant and polarity, which differ between biocompatible and more traditional solvents, directly modulate the fundamental forces governing stability, aggregation potential and interactions with biological surfaces and membranes. This understanding empowers more informed choices, possibly allowing the tailoring of TMDs behavior by matching the solvent to the desired application, enhancing stability in specific biological fluids.
- Expanding Materials Possibilities: The successful demonstration of nanosheets production in cyrene expands the fabrication toolkit. Solvent compatibility is a critical factor determining which nanomaterials are compatible with different exfoliation methods. By widening the range of usable solvents to include greener options, we open the door to exploring a wider variety of TMDs and potentially other 2D materials. This is essential for realizing diverse potential applications with specific property requirements.
- Safeguarding Sensitive Environments: Biomedical applications offer a compelling case for biocompatible solvents. Whether for diagnostics, targeted drug delivery, or therapeutic platforms, TMDs nanosheets will come into direct contact with cells, tissues, and biological fluids. Thus, quitting with toxic solvents not only reduces hazards during fabrication, but minimizes any potential risk of contamination or harm during their use within a biological setting. This commitment to safety is essential for establishing trust in TMD-based technologies and facilitating their adoption in sensitive areas.
- Environmental Responsibility: The potential impact of these materials extends beyond biological settings. The use of biocompatible solvents supports a more sustainable approach to materials development that aims to minimize the environmental footprint of scientific and technological advancements. TMDs, due to their unique properties, possess transformative potential across fields like electronics, energy, and catalysis. By embedding biocompatibility concerns into their development from the earliest stages, we help drive a shift towards creating new materials with a reduced environmental burden.

The findings from the three studies presented in this thesis offer a diverse perspective on the behavior and implications of 2D TMDs, particularly in the context of their interactions with biological systems and radiation environments. By synthesizing the key insights across these chapters, we gain a deeper understanding of 2D TMDs nanomaterial properties, their response to various environmental factors, and their potential applications in diverse fields.

6.2.2 Theory and Experimental Integration

A unifying theme across the studies is the integration of theoretical frameworks, particularly the Derjaguin-Landau-Verwey-Overbeek (DLVO) theory, to guide experimental design and interpretation. The DLVO theory provides a robust theoretical foundation for understanding the interactions between nanomaterials and their surrounding environments, considering the main actors of physics into play, namely van der Waals forces, electrostatic repulsion, and solvent effects.

Incorporating an on-purpose adapted version of the DLVO theory in the analyses of nanosheets-bacteria interactions and solvent-mediated exfoliation processes underscores its significance in nanoscience. By coupling experimental observations with theoretical models, we can predict and manipulate the dispersion stability, interaction energies, and structural transformations of nanomaterials, enabling their rational design for specific applications.

For instance, the DLVO-based analysis of the antimicrobial activity of 2D-MoS_2 nanoflakes against different bacteria strains sheds light on the underlying mechanisms governing nanoobject-bacteria interactions. The model-guided understanding of the interplay between electrostatic forces and van der Waals attractions reveals how the surface chemistry, size, and charge of the MoS_2 nanoflakes can be tailored to enhance their antibacterial efficacy. This knowledge paves the way for developing targeted antimicrobial strategies and designing advanced nanomaterial-based coatings and agents for biomedical applications.

Similarly, applying DLVO theory in studying solvent-mediated exfoliation of 2D TMDs nanosheets provides insights into the dispersion stabilization mechanisms. By considering the balance of attractive and repulsive forces, we can select appropriate solvents, such as cyrene, that effectively disperse and stabilize the 2D TMDs nanosheets, as has been done in this thesis in chapter 4, making them suitable for a wide range of applications, including flexible electronics, energy storage and biomedical devices.

Moreover, our study utilize Monte Carlo simulations to explore the gamma radiation-induced structural alterations of nanomaterials. This approach provides theoretical insights and contributes to refining and expanding existing theoretical frameworks in nanoscience. By exploring how ionizing radiation influences the structure and properties of nanomaterials 96 within aqueous environments, we enrich our fundamental understanding of nanomaterial behavior in intricate and evolving settings. Interestingly, we find that, in addition to the direct gamma photon - nanoflake interactions, indirect interactions between reactive species produced by gamma radiation- induced hydrolysis of water and nanoflakes play a fundamental role, which is peculiar of the water context under ionizing radiation treatment. These theoretical advancements serve as the foundation for constructing predictive models essential for guiding the design and optimization of nanomaterials. Such optimized nanomaterials hold promise for diverse applications, including radiation therapy, environmental remediation, and radiation dosimetry.

For the experimental part of this thesis, we systematically explored nanosheets fabrication using LPE by ultrasonication, which breaks down bulk materials into nanosheets, followed by centrifugation to purify, isolate, and size select these exfoliated nanomaterials. This well-established method for producing nanosheets from bulk materials formed the foundation of our experiments.

We employed a comprehensive suite of characterization techniques to analyze the nanomaterials' structural, optical, and morphological properties. UV-vis spectroscopy revealed their optical properties. Zeta potential analysis measured their surface charge and colloidal stability, while Dynamic Light Scattering (DLS) determined their size distribution and stability profiles. Raman spectroscopy explored the number of layers per flake, while Atomic Force Microscopy (AFM) and Scanning Electron Microscopy (SEM) provided high-resolution surface morphology images. Finally, X-ray Photoelectron Spectroscopy (XPS) revealed the elemental composition and chemical state, providing a deeper understanding of the materials' properties.

The above exfoliation and characterization has been used in both Chapters 4 and 5. Chapter 4 investigated cyrene as an LPE solvent to exfoliate both MoS_2 and WS_2, due to cyrene eco-friendliness and compatibility with our materials. Chapter 5 then focused on water as a solvent, capitalizing on its biocompatibility and abundance, making it ideal for potential biomedical applications.

6.2.3 Practice and Application

Beyond the contributions stated in the thesis, the findings from these studies have direct implications for various fields, including biomedicine, materials science, and environmental engineering, highlighting the versatility and impact of nanomaterials.

In biomedicine, the antimicrobial properties of TMDs nanoflakes in general and 2D MoS_2, in particular, hold promising potential for developing novel antibacterial agents and coatings. By leveraging the unique interactions between the nanoflakes and E. coli, for example, we might effectively design targeted strategies to combat some bacterial infections. The understanding of how the surface chemistry and charge of the nanoflakes influence their antimicrobial efficacy provides a foundation for the rational design of nanomaterial-based antimicrobial solutions.

Furthermore, the stability and biocompatibility of cyrene-dispersed 2D TMDs nanosheets make them attractive candidates for various biomedical applications, such as drug delivery systems and biosensors. The ability to tailor the properties of these nanomaterials through solvent selection and functionalization strategies opens up new avenues for developing advanced biomedical technologies. For instance, the high colloidal stability and tunable surface chemistry of the cyrene-exfoliated 2D TMDs nanosheets can improve the efficacy and safety of drug treatments. Additionally, integrating these nanomaterials into biosensing platforms can enhance the performance and functionality of these medical devices, ultimately leading to improved patient outcomes.

Developing advanced electronic and energy storage devices often relies on integrating nanomaterials with unique optical, electrical, and mechanical properties. The high dispersibility, stability, and tunable functionalities of the cyrene-exfoliated 2D TMDs nanosheets make them promising candidates for these applications. For instance, integrating these nanomaterials into flexible electronic devices may enable the fabrication of light-weight, bendable, and highly conductive components, opening up new possibilities for wearable electronics and conformable displays. Similarly, using 2D TMDs nanosheets in energy storage devices, such as batteries and supercapacitors, can enhance energy density and power density, contributing to the advancement of sustainable energy technologies.

Moreover, the insights gained from studying the radiation-induced structural modifications of nanomaterials have implications for various fields, including radiation therapy and environmental remediation. By understanding how nanomaterials respond to ionizing radiation in aqueous environments, we can develop novel approaches for targeted cancer treatments and radioactive waste management.

In radiation therapy, the ability to tailor nanomaterials' structural and functional properties in response to ionizing radiation can enable the design of advanced theranostic agents. These multifunctional nanomaterials can simultaneously serve as imaging contrast agents and targeted delivery vehicles for therapeutic payloads, potentially enhancing the efficacy and precision of cancer treatments. Additionally, the potential use of irradiated nanomaterials as radiation-sensitive sensors and detectors warrants further exploration for applications in radiation dosimetry and environmental monitoring, aiding in assessing and managing radiation exposure in various settings.

Collectively, the findings presented in the three studies offer a holistic understanding of the behavior and applications of 2D nanoflakes in diverse environments. By examining bacterial interactions, dispersion characteristics, and responses to irradiation, the research underscores the versatility and potential of these nanomaterials across various fields, including biomedicine, environmental remediation, and advanced materials science. Further interdisciplinary research is warranted to explore the different properties and applications of 2D nanoflakes, leveraging the insights gained from these studies to address pressing societal challenges and advance scientific knowledge.

Chapter 7

Conclusion and Future Outlook

7.1 Conclusion:

In conclusion, our research journey into the synthesis, functional properties, and potential applications of two-dimensional transition metal dichalcogenides (TMDs) nanosheets synthesized using environmentally friendly solvents has yielded valuable insights and promising avenues for future exploration. Through a comprehensive examination of TMDs nanosheets' antibacterial properties, response to irradiation, and synthesis methodologies, we have contributed significantly to understanding these nanomaterials in biomedical applications.

Our investigation into the liquid-phase exfoliation of TMDs nanosheets in cyrene and water solvents has demonstrated the efficacy of environmentally friendly synthesis routes. By optimizing exfoliation parameters and employing innovative pre-treatment methods, we achieved the fabrication of high-quality nanosheets with controlled size, thickness, and morphology. These results highlight the scalability and sustainability of our synthesis approach on a large-scale production base and lay a solid foundation for developing TMDs nanosheets with tailored properties for diverse biomedical applications.

By combining theoretical frameworks with experimental methodologies, we have contributed to the ongoing exploration of two-dimensional materials in medical science and technology. Moving forward, our findings offer further innovation and discovery in the field of nanomedicine, driving the potential development of next-generation nanomaterials with transformative impacts on healthcare and beyond.

Targeting the understanding of nanosheets interactions and the refinement of production processes this thesis employs two approaches: DLVO theory and Monte Carlo simulations for theoretical understanding of nanosheet interactions and experimental method through liquid-phase exfoliation (ultrasonication) followed by a number of advanced spectroscopical and microscopical characterization techniques (UV-vis, zeta, DLS, Raman, AFM, SEM, XPS). This synergy between theory and experiment refines production processes and unlocks a deeper grasp of nanosheet interactions.

Our exploration of the antibacterial properties of TMDs nanosheets has revealed promising avenues for combating bacterial infections and enhancing medical device coatings. Through theoretical modeling, we have elucidated the intricate interactions between TMDs nanosheets and bacterial strains, using a version of the DLVO theory's specifically developed to study to the interaction of MoS_2 nanoflakes with various strains of bacteria. Through rigorous analysis, it was determined that the electrostatic and van der Waals forces played pivotal roles, with the distinction in the behaviour between gram-positive and gram-negative bacteria becoming evident. The unique behavior of E. coli, in contrast to other bacteria, emerged as a notable finding, owing much to its peculiar membrane structure and lower ζ-potential. The introduction of the green, but organic, solvent cyrene into the model unveiled a different mediating effect on these interactions when compared to the traditional use of water.

The theoretical exploration was followed by an experimental characterization of the MoS_2/WS_2 nanosheets produced using in cyrene. This study introduced a pretreatment step involving bath sonication followed by regular ultrasonication-based exfoliation. The resulting dispersion was characterized by different techniques, and again, we used the DLVO theory adapted to study the nanoflake-nanoflake interactions, followed by the long-term evaluation of the dispersion's stability. The characterization evidenced the exfoliated nanosheets' morphological characteristics and surface charge dynamics.The findings also underline the high quality of the obtained nanoflakes through cyrene-based exfoliation. This study demonstrates cyrene as a potential green solvent that doesn't compromise the quality of the resulting nanomaterials.

Furthermore, our investigation into the response of TMDs nanosheets to irradiation has unveiled exciting prospects for their utilization in radiotherapy and oncology. By unraveling the structural and chemical changes induced in TMDs nanosheets upon ionizing irradiation exposure, we study the effects of 511-keV photon irradiation on the MoS_2 nanosheets exfoliated in water followed by centrifugation and detailed characterization as the previous study. This study marked a significant leap forward, illustrating the potential consequences for these nanomaterials when used for clinical settings and sujected to irradiation-based therapies, particularly in oncology. The experimental results, supported by Monte Carlo simulations, painted a detailed picture of the structural and compositional changes induced by irradiation, fundamentally completing our undestanding of the behaviour of nanomaterials in medical applications. The emergence of new Raman vibration modes and the XPS analysisshed light on the oxidation processes at play, suggestingthe mechanism of action and the type of impact of gamma photons on two-dimensional materials in radiotherapy treatments.

Finally, The contributions of this thesis to the field are manifold, presenting both methodological advancements and novel experimental insights. The extended DLVO model offers a powerful tool for predicting interactions across a spectrum of bacteria and nanomaterials. At the same time, the experimental techniques for nanoflake production set new standards for efficiency and sustainability in material science. The innovative use of Monte Carlo simulations in conjunction with experimental data establishes a robust method for understanding the effects of radiolysis on nanomaterials. This methodology can be applied broadly across various forms of nanotechnology.

The implications of the findings extend into numerous areas. In material science, the research provides a blueprint for producing high-quality nanomaterials using environmentally friendly solvents, which could impact the industry's approach to nanomaterial synthesis. For the medical field, the potential applications of MoS_2 nanoflakes in bioimaging, drug delivery, and as therapeutic agents are vast, with this thesis serving as a launching pad for further exploration into the medical applications of two-dimensional materials.

7.2 Future Outlooks and challenges:

7.2.1 Future Outlooks

The research presented in this thesis lays the groundwork for a future where TMDs nanosheets play a transformative role in biomedicine and beyond. The commitment to biocompatible fabrication and the exploration of potential applications offer a pathway for using the exceptional properties of these materials in a responsible and impactful manner. Here, we outline promising future directions and address challenges.

Looking ahead, our research opens up compelling avenues for further innovation. One key area lies in integrating machine learning (ML) algorithms to revolutionize the liquid-phase exfoliation of Transition Metal Dichalcogenides (TMDs). By training ML models on large datasets of synthesis parameters, we can identify patterns, correlations, and optimal conditions that might be difficult to discern through traditional methods alone. This would accelerate our understanding of the exfoliation process, enabling us to tailor nanosheet properties with greater precision and yield. Moreover, ML can assist in selecting the most suitable environmentally friendly solvents and optimizing their ratios, further enhancing the sustainability of TMDs production. Beyond streamlining experimental processes, ML can even suggest novel synthesis strategies or predict the properties of unexplored TMDs materials, driving the discovery of the next generation of biomedical nanomaterials.

Another area to focus on in our future work is advanced biological investigations such as In-vitro cytotoxicity studies; conducting comprehensive in-vitro studies on TMDs nanosheet interactions with diverse mammalian cell lines will provide valuable insights into their biocompatibility and potential therapeutic applications. By carefully assessing cellular viability, proliferation, and morphology, we can determine safe dosage ranges and clarify any adverse effects, and facilitate for safer biomedical applications. Also, animal model studies (in-vivo), are certainly crucial for assessing the translational potential of TMDs nanosheets in living organisms. By employing animal models, we can explore more biocompatibility, pharmacokinetics, and therapeutic efficacy, providing essential preclinical data necessary for eventual clinical trials. These studies will shed light on the physiological responses and long-term effects of TMDs nanosheets, facilitating the development of targeted therapies.

Another area of interest regards the antibacterial action efficacy, given the escalating threat of antibiotic resistance, exploring the antibacterial properties of TMDs nanosheets against a broad spectrum of clinically relevant pathogens is imperative. By conducting rigorous antibacterial efficacy studies, including assessments against multi-drug resistant strains, we can ascertain the potential of TMDs nanosheets as alternative antimicrobial agents. Understanding the mechanisms underlying their antibacterial activity will aid in combating infectious diseases and inspire the development of novel therapeutic strategies.

7.2.2 Challenges and Improvements

7.2.2.1 Refining the Theoretical Framework for Biomedical Precision:

The extended DLVO model provides insights into the interplay between solvents, TMDs, and bacteria. However, to maximize its predictive power for biomedical applications, refinements are essential:

Addressing Surface Heterogeneity: The current model could be refined to account for the variations in bacterial membrane properties, including differences in membrane thickness and membrane protein composition. Additionally, considering the actual geometry of bacteria, which can range from 2 to 6 micrometers in length, is crucial. Bacterial shapes, whether rod-like, spherical, or spiral, influence the interaction dynamics with TMD nanosheets. A more nuanced model that incorporates these factors could better predict interactions between TMD nanosheets and diverse bacterial strains. Including an image depicting the typical dimensions and shapes of bacteria could further illustrate these interactions.

Predicting Functionalization Effects: The model could be adapted to predict how modifying the surface of TMDs nanosheets would influence their interactions with bacteria or other cellular components. This would allow the design of targeted functionalization strategies for specific applications.

Diverse Targets: Investigate the model's applicability for interactions with various other biological targets, including viruses, different mammalian cell types, or specific tissues. This expansion would open avenues for diverse drug delivery or targeting applications.

7.2.2.2 Expanding the Biocompatible Fabrication Toolkit:

The successful use of cyrene highlights the feasibility of green alternatives in TMDs fabrication. Future endeavors in this domain include:

TMDs Diversity: Systematically investigate the suitability of cyrene or its tailored co-solvent systems for other TMDs beyond MoS_2 and WS_2. This could unveil TMDs-specific advantages for biomedical use based on differences in bandgap, bio-reactivity, or functionalization potential.

Process Optimization: Conduct studies to reduce cyrene's viscosity challenges. This could involve varying sonication parameters (such as time, power and temperature), exploring pre- and post-exfoliation treatments, or employing co-solvents selected for optimal TMDs dispersibility.

Alternative Green Methods: Investigate other biocompatible synthesis routes. These could include modified CVD techniques using non-toxic precursors or novel bottom-up synthesis strategies designed around minimizing the use of harsh chemicals.

7.2.2.3 TMDs-Based Innovations for Cancer Therapy:

After radiation exposure, the observed changes in water-dispersed TMDs require further investigation to understand the underlying mechanisms fully. This research should include:

Quantifying Dose-Response Effects: Rigorous studies are needed to map the relationship between radiation dose, type of radiation (gamma, electron beam, etc.), and the resulting structural and chemical modifications in TMDs nanosheets.

Radiosensitizing Agents: Conduct rigorous in vitro and in vivo studies to evaluate the efficacy of radiation-modified TMDs in enhancing the effects of radiotherapy. This would involve cell culture models and animal studies, aiming to lower the required radiation dose for effective treatment.

7.2.2.4 Translating into clinical use:

Translating these innovations into clinical use requires addressing practical concerns:

Scalability and Cost: Develop industrially viable, biocompatible processes for large-scale TMDs production while maintaining cost-effectiveness.

Safety and Regulation: Establish comprehensive safety standards through extensive toxicity and long-term biocompatibility studies. Engage proactively with regulatory bodies to establish protocols for novel TMDs-based therapeutics.

Ethical Considerations: Foster open dialogue with stakeholders, including patients and healthcare providers, to address ethical considerations associated with new medical nanomaterials.

The Power of Collaboration: Accelerating the realization of TMDs-based technologies hinges on multidisciplinary collaboration. Strong partnerships between materials scientists, biologists, medical researchers, chemical engineers, and regulatory specialists will ensure safe, effective, and sustainable implementation of these innovations.

Appendix A

Supplementary Materials for Chapter 4

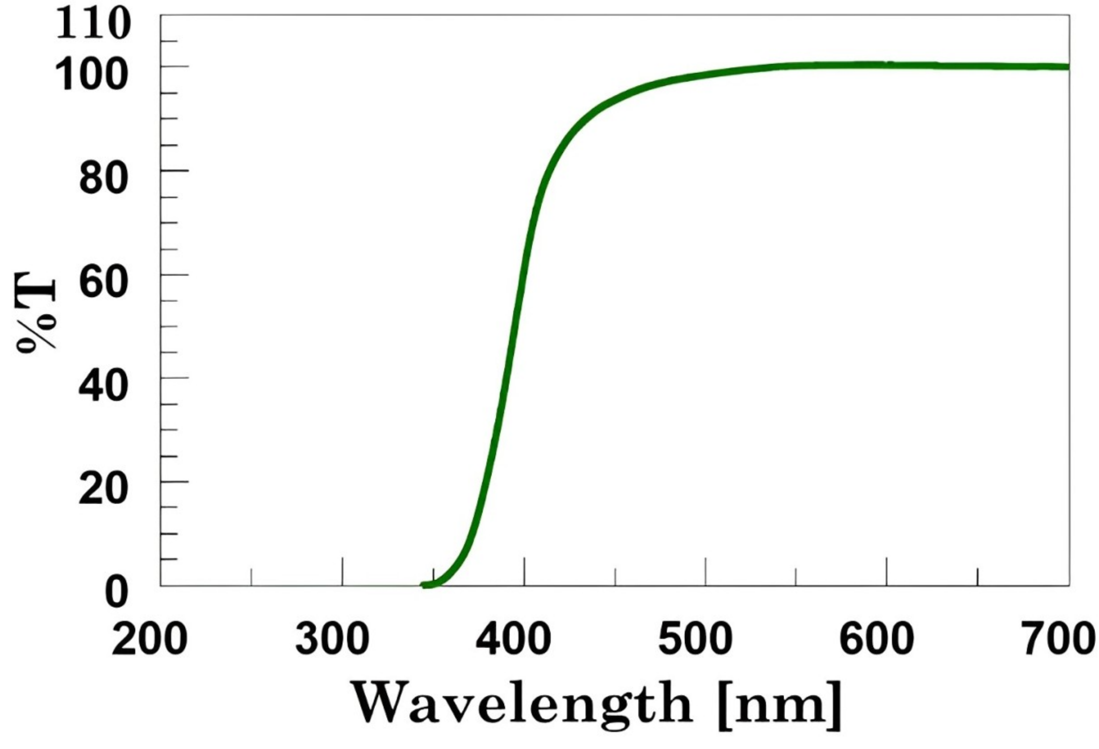

Figure A.1: UV spectra of pure Cyrene (y axis is reported % Transmittance). A total extinction of the UV radiation from 200 to 360 occurs

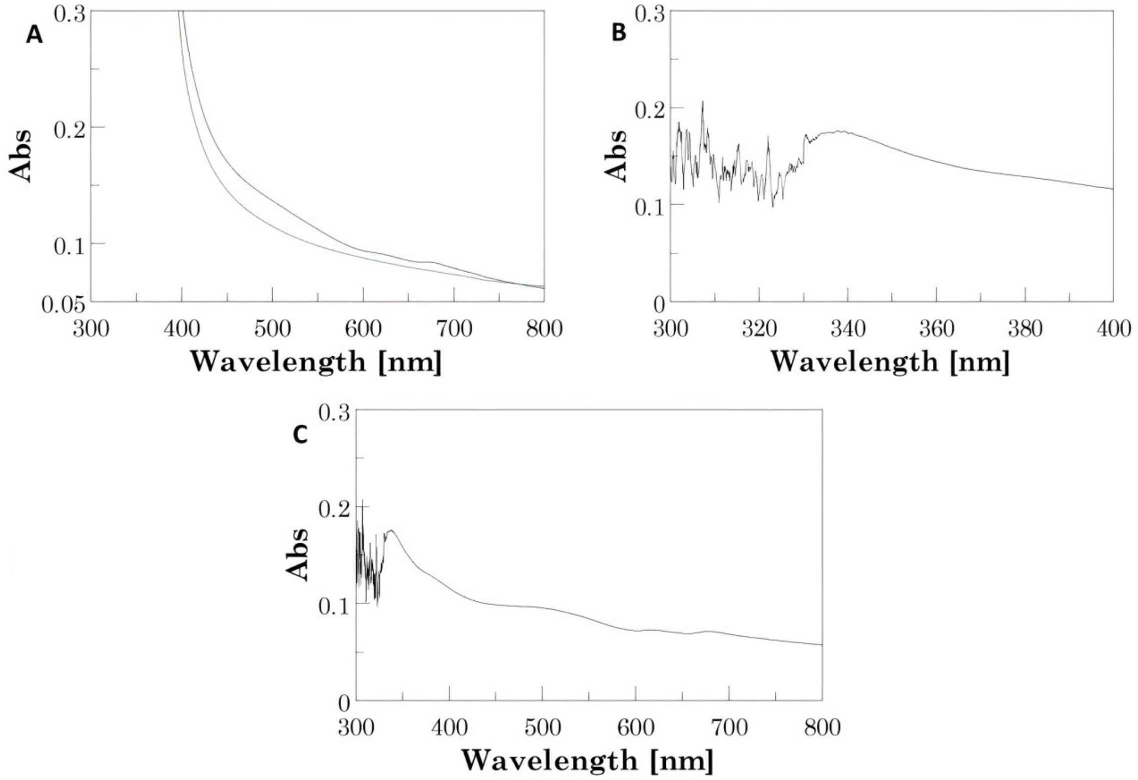

Figure A.2: UV spectra of Cyrene: water 1:1 (green line) and MoS_2/Cyrene: water 1: 1 (blue line) B. Difference spectrum of MoS_2/Cyrene: water 1:1 and Cyrene: water 1:1. C. Enlargement of the difference spectrum in panel B. The absorbance interference of Cyrene in water did not allow to determine the minimum in the UV profile occurring in the range of 320-340 nm.

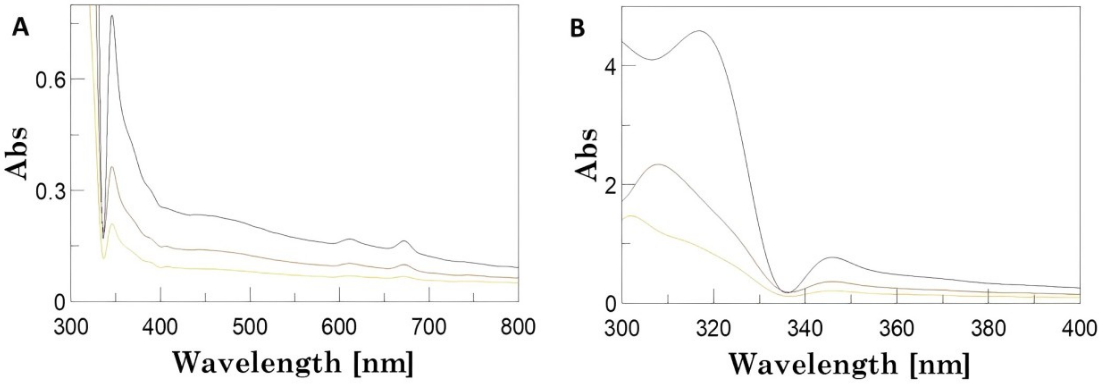

Figure A.3: Deconvoluted UV-vis spectra of MoS_2/Cyrene: MeOH at dilution level 1:5 (blue line), . 1:9 (red line) and 1:17 (green line). B. Enlargement of the deconvoluted UV-vis spectra reported in A in the range 300-400 nm.

2D material: solvent	λ_A	Ext_A	λ_B	Ext_B	Ext_{334}
MoS_2/Cyrene: MeOH 1:1	669	0.310	610	0.345	0.557

$$\mathrm{N} = 23.1 \times 10^{36} \times e^{\frac{54888}{\lambda_A}} = 5.6$$

$$\mathrm{L} = \frac{3.5\,x\,\mathrm{Ext_B}/\mathrm{Ext_{334}} - 0.14}{11.5 - 3.5\,x\,\mathrm{Ext_{334}}/\mathrm{Ext_B}}$$

$$\mathrm{L} = 0.121 \mu m$$

Table A.1: Values of extinction of radiation at wavelengths corresponding to the maxima in excitons A and B and at 334 nm. The values were taken in the difference spectrum (Figure A.2)

Appendix B

Supplementary Materials for Chapter 5

B.1 Sample characterization

B.1.1 UV-Visible absorbance Spectroscopy

The basic information about the physical parameters of the exfoliated 2D NSs, such as the <N>, <L>, and Mean concentration <L>, were extracted from UV-VIS extinction spectra acquired by a V-730 Jasco UV-Visible Spectrophotometer.

The extinction spectra contain the contribution from both absorbance and scattering components. We quantified the physical parameters of 2D NSs from these two components using formula reported in literature [145, 196] our experimental protocol, at lower centrifugal force 100 g, scattering component was more dominant with high extinction peaks at 680 nm, so we discarded this sample for any further characterization. Whereas, at 1000 g, the two exciton peaks, A-exciton, and B-exciton shifted towards lower wavelength region and consequently few-layered enriched dispersion is obtained. The extinction spectra of MoS_2 after the final step of centrifugation at 1000 g is shown in Figure. After irradiating the sample, a red shift in the two excitonic peaks is observed which corresponds to the change in the layer number and lateral size of the irradiated treated 2D NSs, Figure B.1.

B.1.2 Dynamic Light Scattering (DLS): size and ζ-potential measurements

Size measurements of 2D-MoS_2 were performed by DLS technique using a Malvern Zetasizer nano ZS. Data reported is taken as the average of three measurements (n = 3) measured at 25°C in disposable folded capillary cells (DTS1070) in water dispersants.

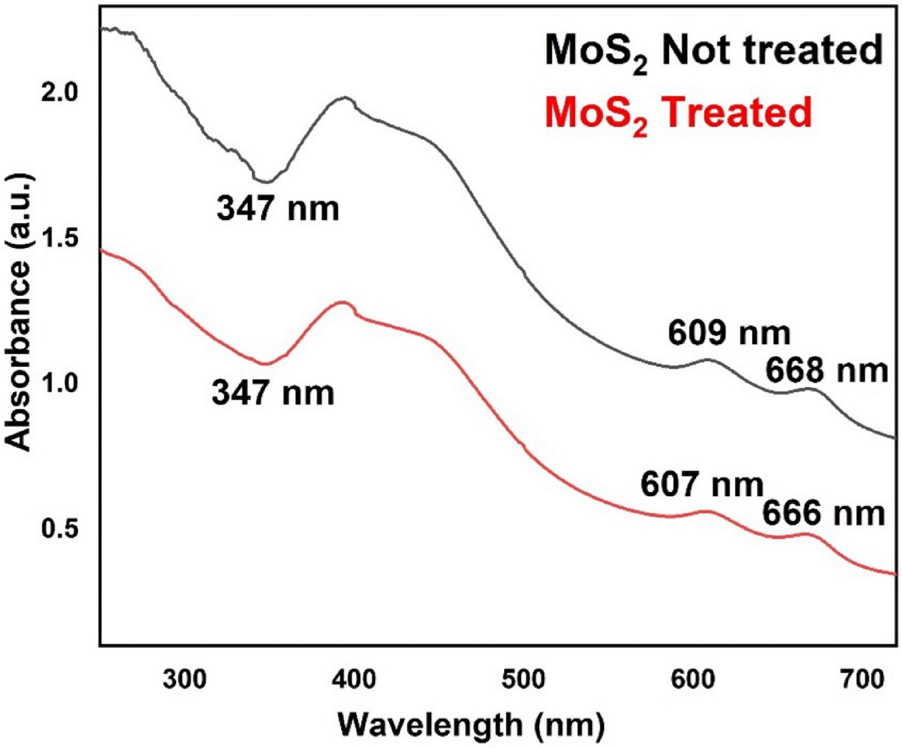

Figure B.1: Corresponds to the comparative UV-vis absorbance spectra of Not treated MoS_2 dispersion and irradiated-treated 2D MoS_2 dispersion with 68Ga radioisotope photons, respectively.

Liquid phase exfoliation produces also surface charges of the 2D-MoS_2 NSs which plays an important role in understanding the stability kinetics of liquid exfoliated dispersions. At this purpose ζ-Potential measurements were also performed. These measurements were carried out on laser interferometric technique (Malvern Zetasizer Nano system) with irradiation from 633 nm He-Ne laser. The samples were injected in folded capillary cells, and the electrophoretic mobility (μ) value was measured using a combination of electrophoresis and laser Doppler velocimetry techniques. All the measurements were carried out at 25 °C.

Surface charge present on the exfoliated 2D NSs is essential in deciding its fate in its interaction with the outer context. The quantitative information obtained from the measured electrophoretic mobility and surface charge in a given medium explains the stability kinetics of exfoliated 2D NSs, in pure water or in any given solvent. We observed a nearly unchanged NS ζ-Potential after radiation treatment with a tiny decrease of its negative value and, thus, a small decrease in the negative overall charge value accumulated over the NS surfaces. This, in turn, implies also a little decrease in the stability of the dispersion in water over the two weeks. The slight decrease in the ζ-Potential negative values could be attributed to a moderate partialization of the initial negative surface charges with some H+ ions present in solution because of the well-known slightly acidic behavior of the H_2O_2 excess, produced by radiolysis induced by the ionizing radiation interaction with water solvent. Moreover, the little decrease trend remained quite consistent in all the software runs over the measurement duration.

Also, mean size of exfoliated 2D NSs measured by DLS showed a trend to aggregation of the nanoflakes after treatment. In fact, the average DLS value measured for exfoliated untreated 2D NSs was ≈ 190 nm, whereas after irradiation, the average size of 2D MoS_2 NSs increased to about 220 nm, as shown in Table S1 B.1. These findings explain why the treatment of 2D NSs with γ-photons in water solution affects the stability kinetics of the NSs. The statistical value of the mean DLS size and ζ-Potential for the probed nanoflakes is reported in Table S1 B.1.

2D nanomaterial	Centrifugal force (g)	Average Zeta potential (ζ) mV	Electrophoretic mobility (μ)	Average DLS size d (nm)
MoS_2 (non-irradiated)	1000 g	-32.1 ± 1.5	-2.193 ± 0.4	194 nm
MoS_2 (Irradiated)	1000 g	-29.8 ± 1.62	-2.33 ± 0.6	220 nm

Table B.1: Represents the average linear size d (nm) of the nanosheets as estimated by DLS measurements and the average ζ-potential value of the NSs for treated and untreated cases. The analysed NS sample was fabricated by centrifuging at 1000 g.

B.1.3 SEM-EDS for morphological and semiquantitative chemical Analysis

The morphological properties of MoS_2 flakes were examined in pristine and Au-coated conditions by using a field emission gun scanning electron microscope Zeiss Leo 1530 model (ENEA, Centro Ricerche Casaccia laboratory) working at low voltage (i.e., 8kV). Data image processing was done using Software controller FeSEM: SmartSem. A Zeiss Merlin VP compact equipped with charge compensation system and with Oxford Instruments Microanalysis both EDS X-max 50 and WDS Wave, (DiSTAR laboratory, Università degli Studi di Napoli Federico II), was used for semi quantitative chemical analyses of the samples. The Electron Microscope Field emission Zeiss Merlin VP Compact with camera Gemini II is composed by three secondary electron detectors SE2 (Classic Detector), VPSE (Variable Pressure) and InlensDuo (Low Voltage) and by two backscattered electron detectors AsB and InlensDuo. Data processing was done using INCA (EDS e WDS) e Aztec (EDS). The samples were placed on a glass support by appropriate droplet drop casting; then, they were metalized with graphite by using a sputter coater. The semi-quantitative chemical analyzes were carried out by imposing the closure at 100wt%, for an immediate reading of the data. For each sample 20 analysis points were performed.

B.1.4 Raman Micro-spectroscopy of 2D-MoS_2

In our experiment, Raman spectra were acquired by using a commercial micro-Raman system (WiTec, Alpha 300) endowed with a Raman probe at $\lambda_{exc} = 532$ nm. A typical Raman spectrum of the of the produced nanoflakes exhibits the two characteristic bands,

E^1_{2g} and A_{1g}, corresponding to in-plane and out-of-plane vibrational modes [197, 97]. According to literature[101, 277, 278] the frequency shift $\Delta\nu_{MoS_2} = \nu_{A_{1g}}$ - ν^1_{2g} between these modes can be used to identify the number of layers n in 2D-MoS_2. Therefore, to get this parameter for the flakes produced by our protocol, we performed a Raman analysis on exfoliated MoS_2 deposited on a coverslip. In particular, 50 μL of the nanoflakes suspension were dropped on a glass coverslip and allowed to dry at room temperature.

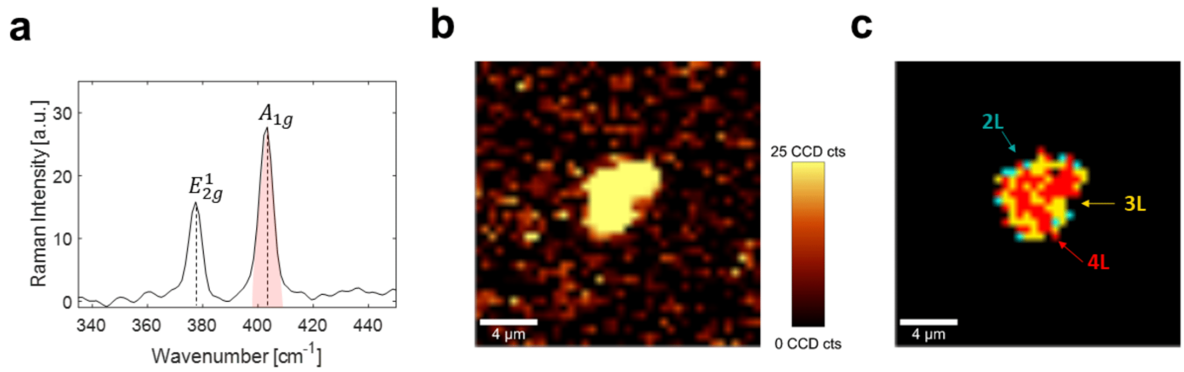

Figure B.2: Typical Raman spectrum of exfoliated 2D-MoS_2, showing the two characteristic peaks of E^1_{2g} and A_{1g} modes at about 380 cm^{-1} and 403 cm^{-1}, respectively; b) mapping of the band intensity distribution of the A_{1g} spectral peak highlighted in red in a), obtained in a raster scanning of a 2D-MoS_2 agglomerate in a 20 μm × 20 μm region. Acquisition parameters were 7 mW laser beam power and 0.5 s acquisition time, respectively, while the step size was 500 nm. c) Map reporting the number of layers for the agglomerate of flakes shown in b)

In Figure B.2 we show a typical Raman spectrum of exfoliated 2D-MoS_2, showing the two characteristic peaks of E^1_{2g} and A_{1g} modes at about 380 cm^{-1} and 403 cm^{-1}, respectively (a); a mapping in b of the band intensity distribution of the A_{1g} spectral peak highlighted in red in a, obtained by a raster scanning of a 2D-MoS_2 agglomerate in a 20 μm × 20 μm region. The Raman map in b clearly reveals the presence of a nanoflake agglomerate in its central region. In c a map is shown reporting the number of layers for the agglomerate of flakes shown in b, estimated from the difference of the two characteristic peaks positions (2L: 23.4 cm^{-1}, 3L: 24.6 cm^{-1}, 4L: 25.9 cm^{-1})[218].

B.1.5 Atomic Force Microscopy (AFM)

To analyse the nanoflakes morphology, Atomic Force Microscopy (AFM) was also employed. At this purpose, 50 μL of 2D-MoS_2 suspension was dropped onto a Si/SiO_2 substrate heated at $\sim$ 100 °C and allowed to evaporate. This procedure strongly reduced 2D-MoS_2 aggregation. AFM measurements were performed in AC mode, so that in each scan both phase and morphological (height) maps were acquired.

ImageJ software was used for quantitative analysis of the AFM images in terms of area, perimeter, circularity, and roughness. The algorithm operates a specific background

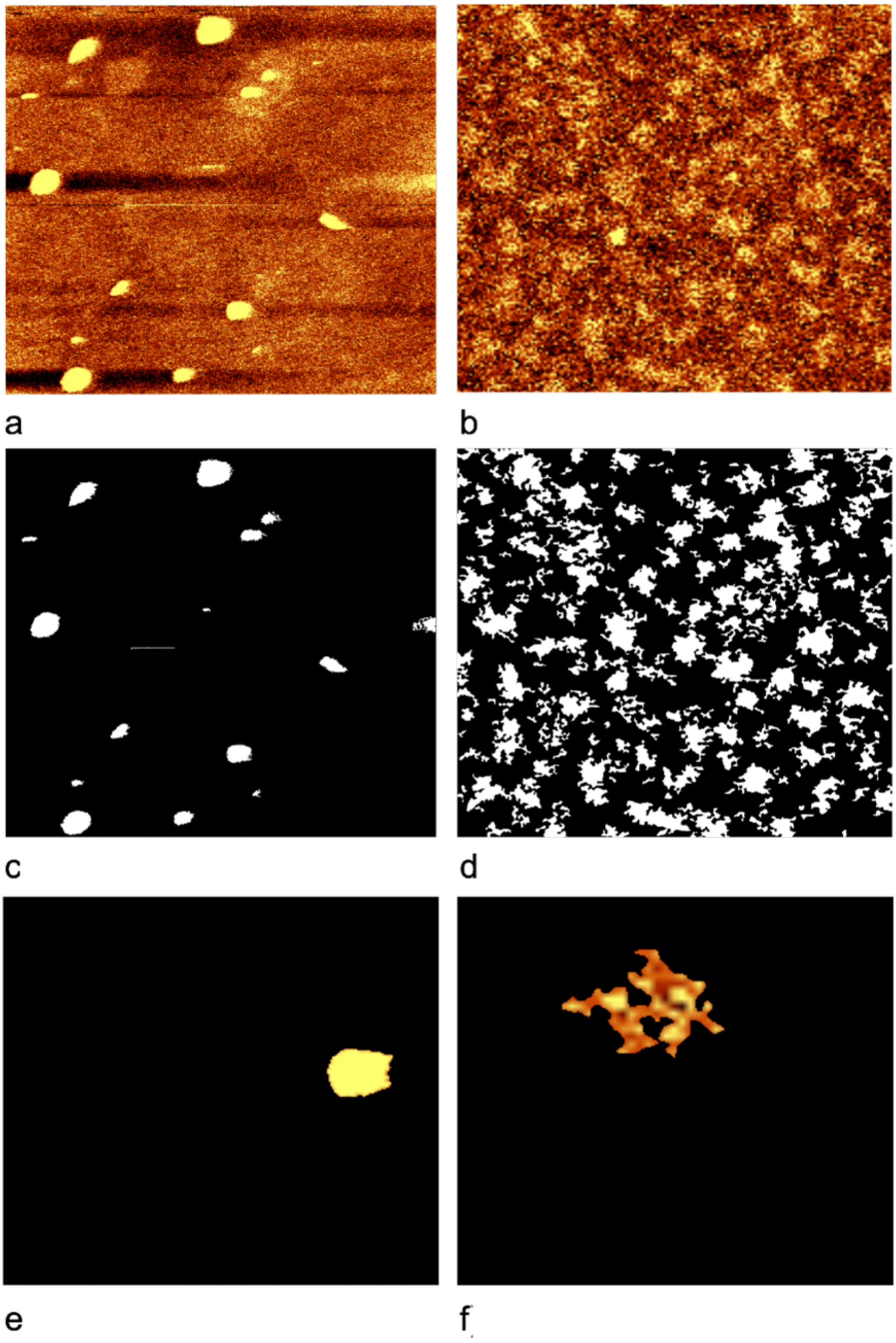

Figure B.3: a AFM image of treated 2D MoS_2 nanoflakes b AFM image of untreated 2D MoS_2 nanoflakes c - d segmentation masks applied as pre-processed step to select treated and untreated MoS_2 nanoflakes; e - f typical segmented treated and untreated MoS_2 nanoflakes. ”

subtraction for the acquired images, creating a mask for segmenting the nanoflakes in the field of view. Therefore, 2D-MoS_2 were counted and analysed. In particular, the following values were obtained: i) the area A corresponding to the number of pixels assigned to each nanoflake, ii) the perimeter P given by the length of its boundaries, and iii) the solidity S, a dimensionless quantity given by the following formula:

$$\mathrm{S} = \frac{\mathrm{A}}{\mathrm{A_c}} \tag{B.1}$$

where $A_c$is the convex area associated with the convex hull in which the nanoflake can be inscribed. On the basis of the previous parameters, the form factor was also estimated F:

$$\mathrm{F} = \frac{4\,.\,\pi\,.\,\mathrm{A}}{\mathrm{p}\,.\,\mathrm{p}} \tag{B.2}$$

Finally, 2D-MoS_2 roughness was calculated, by taking advantage of a plug-in written for ImageJ by Chinga et al. [279]. Roughness was estimated starting from mean deviation (Ra) and root mean deviation (Rq) of pixels from available topographical images.

B.1.6 X-ray Photoelectron Spectroscopy (XPS)

X-Ray Photoelectron spectra were recorded on a XPS Versa Probe II (PHI, ChanassenUS) by large area analysis mode where the monochromated Al anodic beam of 100 μm, at 100 W power, normal to the surface, is rastered over an area of 1400X300 μm with the analyser at 45° with sample surface. Survey spectra were acquired with an accumulation time at least of 20 minutes at high pass energy (187 KeV) while high resolution spectra of the elements of interests where acquired at 11.7 KeV . Spectra were analysed by Multipack (PHI, Chanassen US) software and all the peaks were referenced to the adventious carbon peaks C1s at 284.8 eV binding energy. Samples were prepared by dropping a suspension of the aqueous suspensions of MoS_2 on a flat surface of silicon and the liquid evaporated in a vacuum chamber. As control the suspending aqueous media were also analysed to exclude potential contaminations (data not shown).

	Mean Range (mm)	Maximum range (mm)
Water	2.24	8.92
Glass	0.83	3.30

Table B.2: Mean and maximum range of positron from ^{68}Ga in water and glass

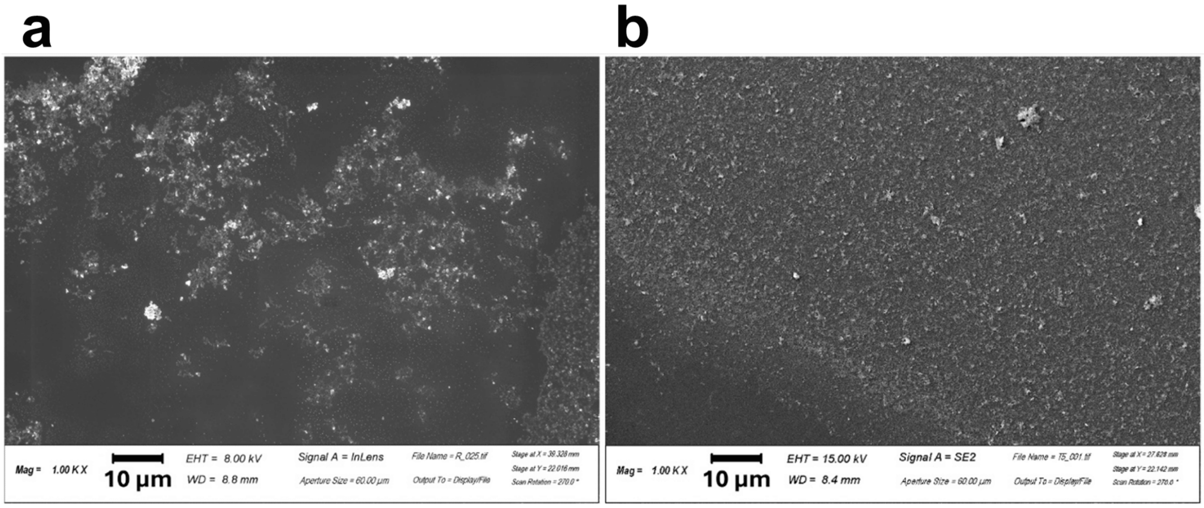

Figure B.4: Distribution of MoS_2 nanoparticles in non-irradiated but exfoliated MoS_2 NSs and in the irradiated MoS_2 samples b, sometimes large aggregates are visible.

	Treated		**Not treated**	
Parameters	**Solidity**	**Form Factor**	**Solidity**	**Form Factor**
Mean ± std	0.8±0.1	0.5±0.2	0.6±0.1	0.3±0.2
Min - Max	0.4-1	0.1-0.90	0.4-0.9	0.1-0.9

Table B.3: statistical analysis of Solidity and Form factor in treated and not treated cases.

	Treated - Ra value in nm	Treated - Ra value in nm
Mean	0.11±0.47	0.15±1.4
Min - Max	0.09-9.01	0.01-1.4

Table B.4: Statistical analysis of Ra (peak-to-valley) roughness parameters in treated and untreated cases.

	Untreated	**Treated (not altered)**	**Treated (altered)**
		Mean (wt%, weight percent)	
S	40.1 ± 0.6	40.1 ± 0.3	35 ± 2
Mo	59.9 ± 0.6	59.9 ± 0.3	65 ± 2
Tot	100.00	100.00	100.00
		APFU (Atoms Per Formula Unit)	
S	1.25 ± 0.02	1.2 ± 0.3	1.1 ± 0.1
Mo	0.62 ± 0.01	0.6 ± 0.3	0.68 ± 0.02
S/Mo	2.01 ± 0.03	2.0 ± 0.6	1.60 ± 0.1
		Formula	
	MoS_2	MoS_2	$MOS_{1.6}$

Table B.5: Stoichiometric effects of ionizing radiation on a statistical sample of 20 analysed MoS_2 NSs.

	Spectral window	Pristine		MoS$_2$ Sonicated		2D NSs Sonicated Centrifuged		2D NSs - TS Sonicated Centrifuged Irradiated	
		Pos	% at	Pos	% at	Pos	% at	Pos	% at
S 2p (MoS$_2$)		162.29	66.67	162.3	61.75	162.29	55.31	162.28	60.15
	159 - 173 eV	163.47	33.33	163.48	30.88	163.47	27.66	163.46	30.08
S 2p (Sulfate)		-	-	168.07	4.91	168.25	11.35	167.86	6.51
		-	-	169.25	2.46	169.43	5.68	169.04	3.26
S 2s (MoS$_2$)		226.83	13.98	226.74	13.5	226.77	13.51	227.64	10.1
S 2s (organosulfur)				228.47	3.02	228.48	3.63	-	-
Mo IV 5/2 -MoIVSyOx		229.51	48.48	229.42	45.93	229.46	43.28	229.48	24.6
Mo IV 3/2 - MoIVSyOx		232.64	32.48	232.55	30.77	232.59	28.99	232.61	16.48
MoV - MoVSyOx	225 - 239 eV	-	-	-	-	-	-	230.45	25.37
Mo V 3/2 - MoVSyOx		-	-	-	-	-	-	233.58	17
S 2s (Sulfate)		-	-	-	-	-	-	233.45	3.26
Mo VI 5/2 - MoVISyOx		232.87	2.67	232.48	4.06	232.66	6.33	233.46	1.92
Mo VI 3/2 - MoVISyOx		236	1.79	235.61	2.72	235.79	4.24	236.59	1.28

Table B.6: Spectral position of energy peaks in the XPS spectra and quantitative surface composition of samples after deconvolution of S and Mo envelops.

	RSF Corrected	Pristine	MoS$_2$ Sonicated	2D NSs	2D NSs -TS
C 1s	8.944	7.88	13.69	14.12	12.76
O 1s	21.107	3.75	12.63	25.42	12.02
S 2p	7.888	28.33	24.38	20.88	24.38
Mo 3d	39.479	60.05	49.3	39.58	50.84

Table B.7: shows the position and quantitative surface composition of samples after deconvolution of S and Mo envelops. It clearly shows a comparison between the 2D NSs and the treated samples exhibiting the shift in the BE peaks after the irradiation procedure (RSF is the Relative Sensitivity Factor).

Bibliography

[1] Paul JA Borm, David Robbins, Stephan Haubold, Thomas Kuhlbusch, Heinz Fissan, Ken Donaldson, Roel Schins, Vicki Stone, Wolfgang Kreyling, Jurgen Lademann, et al. The potential risks of nanomaterials: a review carried out for ecetoc. *Particle and fibre toxicology*, 3:1–35, 2006.

[2] TSV Satyanarayana and Rathika Rai. Nanotechnology: the future. *Journal of interdisciplinary dentistry*, 1(2):93–100, 2011.

[3] A Paul Alivisatos. Semiconductor clusters, nanocrystals, and quantum dots. *science*, 271(5251):933–937, 1996.

[4] MS Dresselhaus, G Dresselhaus, and PC Eklund. Fullerenes. *Journal of materials research*, 8(8):2054–2097, 1993.

[5] Chintamani Nagesa Ramachandra Rao, BC Satishkumar, A Govindaraj, and Manashi Nath. Nanotubes. *ChemPhysChem*, 2(2):78–105, 2001.

[6] Wei Lu and Charles M Lieber. Semiconductor nanowires. *Journal of Physics D: Applied Physics*, 39(21):R387, 2006.

[7] Andre Konstantin Geim. Graphene: status and prospects. *science*, 324(5934):1530–1534, 2009.

[8] Xiao Zhang, Zhuangchai Lai, Qinglang Ma, and Hua Zhang. Novel structured transition metal dichalcogenide nanosheets. *Chemical Society Reviews*, 47(9):3301–3338, 2018.

[9] Dara Van Gough, Abigail T Juhl, and Paul V Braun. Programming structure into 3d nanomaterials. *Materials today*, 12(6):28–35, 2009.

[10] K Gajanan and SN Tijare. Applications of nanomaterials. *Materials Today: Proceedings*, 5(1):1093–1096, 2018.

[11] Hua Zhang, Manish Chhowalla, and Zhongfan Liu. 2d nanomaterials: graphene and transition metal dichalcogenides. *Chemical Society Reviews*, 47(9):3015–3017, 2018.

[12] Andre K Geim. Nobel lecture: Random walk to graphene. *Reviews of Modern Physics*, 83(3):851, 2011.

[13] S Chaiyakun, N Witit-Anun, N Nuntawong, P Chindaudom, S Oaew, C Kedkeaw, P Limsuwan, et al. Preparation and characterization of graphene oxide nanosheets. *Procedia Engineering*, 32:759–764, 2012.

[14] Md Golam Rasul, Alper Kiziltas, Babak Arfaei, and Reza Shahbazian-Yassar. 2d boron nitride nanosheets for polymer composite materials. *npj 2D Materials and Applications*, 5(1):56, 2021.

[15] Varrla Eswaraiah, Qingsheng Zeng, Yi Long, and Zheng Liu. Black phosphorus nanosheets: synthesis, characterization and applications. *Small*, 12(26):3480–3502, 2016.

[16] Xifeng Liu, Bipin Gaihre, Matthew N George, Yong Li, Maryam Tilton, Michael J Yaszemski, and Lichun Lu. 2d phosphorene nanosheets, quantum dots, nanoribbons: Synthesis and biomedical applications. *Biomaterials science*, 9(8):2768–2803, 2021.

[17] Kang Hyuck Lee, Hyeon-Jin Shin, Jinyeong Lee, In-yeal Lee, Gil-Ho Kim, Jae-Young Choi, and Sang-Woo Kim. Large-scale synthesis of high-quality hexagonal boron nitride nanosheets for large-area graphene electronics. *Nano letters*, 12(2):714–718, 2012.

[18] Mohammadreza Soleymaniha, Mohammad-Ali Shahbazi, Ali Reza Rafieerad, Aziz Maleki, and Ahmad Amiri. Promoting role of mxene nanosheets in biomedical sciences: therapeutic and biosensing innovations. *Advanced healthcare materials*, 8(1):1801137, 2019.

[19] Jingfang Yu, Qiang Wang, Dermot O'Hare, and Luyi Sun. Preparation of two dimensional layered double hydroxide nanosheets and their applications. *Chemical Society Reviews*, 46(19):5950–5974, 2017.

[20] Q.H. Wang, K. Kalantar-Zadeh, A. Kis, J.N. Coleman, and M.S. Strano. Electronics and optoelectronics of two-dimensional transition metal dichalcogenides. *Nature Nanotechnology*, 7(11):699–712, 2012.

[21] Rudren Ganatra and Qing Zhang. Few-layer mos2: A promising layered semiconductor. *ACS Nano*, 8(5):4074–4099, May 2014. 1, 26.

[22] Andrea Splendiani, Liang Sun, Yuanbo Zhang, Tianshu Li, Jonghwan Kim, Chi-Yung Chim, Giulia Galli, and Feng Wang. Emerging photoluminescence in monolayer mos2. *Nano Letters*, 10(4):1271–1275, April 2010. 1, 7.

[23] Humberto R Gutiérrez, Nestor Perea-López, Ana Laura Elías, Ayse Berkdemir, Bei Wang, Ruitao Lv, Florentino López-Urías, Vincent H Crespi, Humberto Terrones, and Mauricio Terrones. Extraordinary room-temperature photoluminescence in triangular ws2 monolayers. *Nano Letters*, 13(8):3447–3454, August 2013. 1, 7.

[24] Nicolas Onofrio, David Guzman, and Alejandro Strachan. Novel doping alternatives for single-layer transition metal dichalcogenides. *Journal of Applied Physics*, 122(18):185102, November 2017. 1, 7.

[25] Hannu-Pekka Komsa, Jani Kotakoski, Simon Kurasch, Ossi Lehtinen, Ute Kaiser, and Arkady V Krasheninnikov. Two-dimensional transition metal dichalcogenides under electron irradiation: Defect production and doping. *Physical Review Letters*, 109(3), July 2012. 1, 7.

[26] Xiangjun Liu and Yong-Wei Zhang. Thermal properties of transition-metal dichalcogenide. *Chinese Physics B*, 27(3):034402, March 2018. 1.

[27] Rusen Yan, Jeffrey R Simpson, Simone Bertolazzi, Jacopo Brivio, Michael Watson, Xufei Wu, Andras Kis, Tengfei Luo, Angela R Hight Walker, and Huili Grace Xing. Thermal conductivity of monolayer molybdenum disulfide obtained from temperature-dependent raman spectroscopy. *ACS Nano*, 8(1):986–993, January 2014. 1.

[28] Mojtaba Ahmadi, Omid Zabihi, Seokwoo Jeon, Mitra Yoonessi, Aravind Dasari, Seeram Ramakrishna, and Minoo Naebe. 2d transition metal dichalcogenide nanomaterials: Advances, opportunities, and challenges in multi-functional polymer nanocomposites. *Journal of Materials Chemistry A*, 8(3):845–883, October 2019.

[29] Damien Voiry, Jieun Yang, and Manish Chhowalla. Recent strategies for improving the catalytic activity of 2d tmd nanosheets toward the hydrogen evolution reaction. *Advanced materials*, 28(29):6197–6206, 2016.

[30] Stanley S Chou, Bryan Kaehr, Jaemyung Kim, Brian M Foley, Mrinmoy De, Patrick E Hopkins, Jiaxing Huang, C Jeffrey Brinker, and Vinayak P Dravid. Chemically exfoliated MoS2 as near-infrared photothermal agents. *Angewandte Chemie International Edition*, 52(15):4160–4164, 2013.

[31] Xiao Zhang, Zhuangchai Lai, Chaoliang Tan, and Hua Zhang. Solution-processed two-dimensional mos2 nanosheets: preparation, hybridization, and applications. *Angewandte Chemie International Edition*, 55(31):8816–8838, 2016.

[32] Zhuangzhi Wu, Dezhi Wang, Xiuqi Zan, and Aokui Sun. Synthesis of ws2 nanosheets by a novel mechanical activation method. *Materials Letters*, 64(7):856–858, 2010.

[33] Teng Liu and Zhuang Liu. 2d MoS2 nanostructures for biomedical applications. *Advanced healthcare materials*, 7(8):1701158, 2018.

[34] Kateryna Bazaka, Igor Levchenko, Jian Wei Mark Lim, Oleg Baranov, Carles Corbella, Shuyan Xu, and Michael Keidar. Mos2-based nanostructures: synthesis and applications in medicine. *Journal of Physics D: Applied Physics*, 52(18):183001, 2019.

[35] V Yadav, S Roy, P Singh, Z Khan, and A Jaiswal. 2d mos2-based nanomaterials for therapeutic, bioimaging, and biosensing applications. *Small*, 15(1):1803706, 2019.

[36] Ming Liu, Heng Zhu, Yuan Wang, Canan Sevencan, and Bao-Lian Li. Functionalized mos2-based nanomaterials for cancer phototherapy and other biomedical applications. *ACS Materials Letters*, 3(5):462–496, 2021.

[37] Haotian Wang, Zhiyi Lu, Shicheng Xu, Desheng Kong, Judy J Cha, Guangyuan Zheng, Po-Chun Hsu, Kai Yan, David Bradshaw, Fritz B Prinz, et al. Electrochemical tuning of vertically aligned mos2 nanofilms and its application in improving hydrogen evolution reaction. *Proceedings of the National Academy of Sciences*, 110(49):19701–19706, 2013.

[38] Yukyung Shin, Jayeong Kim, Yujin Jang, Eunji Ko, Nam-Suk Lee, Seokhyun Yoon, and Myung Hwa Kim. Vertically-oriented ws2 nanosheets with a few layers and its raman enhancements. *Nanomaterials*, 10(9):1847, 2020.

[39] Sedigheh Niknam, Seyed Ahmad Dehdast, Omid Pourdakan, Mohammad Shabani, and Mohammad Kazem Koohi. Tungsten disulfide nanomaterials (ws2 nm) application in biosensors and nanomedicine: A review. *Nanomedicine Research Journal*, 7(3):214–226, 2022.

[40] Yibo Liu and Juewen Liu. Hybrid nanomaterials of ws 2 or mos 2 nanosheets with liposomes: biointerfaces and multiplexed drug delivery. *Nanoscale*, 9(35):13187–13194, 2017.

[41] H. Li, J. Wu, Z. Yin, and H. Zhang. Preparation and applications of mechanically exfoliated single-layer and multilayer mos2 and wse2 nanosheets. *Accounts of Chemical Research*, 47(5):1067–1075, 2014.

[42] Bin Ai, Helmuth Moehwald, Dayang Wang, and Gang Zhang. Advanced colloidal lithography beyond surface patterning. *Advanced Materials Interfaces*, 4(1):1600271, 2017.

[43] Jieqiong Qin, Zhi Yang, Feifei Xing, Liangzhu Zhang, Hongtao Zhang, and Zhong-Shuai Wu. Two-dimensional mesoporous materials for energy storage and conversion: current status, chemical synthesis and challenging perspectives. *Electrochemical Energy Reviews*, 6(1):9, 2023.

[44] Xinsheng Wang, Hongbin Feng, Yongmin Wu, and Liying Jiao. Controlled synthesis of highly crystalline mos2 flakes by chemical vapor deposition. *Journal of the American Chemical Society*, 135(14):5304–5307, 2013.

[45] Jialiang Deng, Bingyu Xia, Xiaochuan Ma, Haoqi Chen, Huan Shan, Xiaofang Zhai, Bin Li, Aidi Zhao, Yong Xu, Wenhui Duan, et al. Epitaxial growth of ultraflat stanene with topological band inversion. *Nature materials*, 17(12):1081–1086, 2018.

[46] Dmitry Bokov, Abduladheem Turki Jalil, Supat Chupradit, Wanich Suksatan, Mohammad Javed Ansari, Iman H Shewael, Gabdrakhman H Valiev, and Ehsan Kianfar. Nanomaterial by sol-gel method: synthesis and application. *Advances in Materials Science and Engineering*, 2021:1–21, 2021.

[47] Yenny Hernandez, Valeria Nicolosi, Mustafa Lotya, Fiona M Blighe, Zhenyu Sun, Sukanta De, Iain T McGovern, Brendan Holland, Michele Byrne, Yurii K Gun'Ko, et al. High-yield production of graphene by liquid-phase exfoliation of graphite. *Nature Nanotechnology*, 3(9):563–568, 2008.

[48] Keith R Paton, Eswaraiah Varrla, Claudia Backes, Ronan J Smith, Umar Khan, Arlene O'Neill, Conor Boland, Mustafa Lotya, Oana M Istrate, Paul King, et al. Scalable production of large quantities of defect-free few-layer graphene by shear exfoliation in liquids. *Nature materials*, 13(6):624–630, 2014.

[49] Long Zhang, Jiajie Liang, Yi Huang, Yanfeng Ma, Yan Wang, and Yongsheng Chen. Size-controlled synthesis of graphene oxide sheets on a large scale using chemical exfoliation. *Carbon*, 47(14):3365–3368, 2009.

[50] A. Ciesielski and P. Samorì. Graphene via sonication assisted liquid-phase exfoliation. *Chemical Society Reviews*, 43(2):381–398, 2014.

[51] Aline Amorim Graf. *Physical and chemical characterisation of exfoliated layered nanomaterials.* Thesis, University of Sussex, 2020.

[52] Jonathan N Coleman, Mustafa Lotya, Arlene O'Neill, Shane D Bergin, Paul J King, Umar Khan, Karl Young, Amelie Gaucher, Sukanta De, Ronan J Smith, et al. Two-dimensional nanosheets produced by liquid exfoliation of layered materials. *Science*, 331(6017):568–571, 2011.

[53] J. N. Coleman. Liquid exfoliation of defect-free graphene. *Accounts of Chemical Research*, 46(1):14–22, 2013.

[54] Hin Chun Yau, Mustafa K Bayazit, Joachim HG Steinke, and Milo SP Shaffer. Sonochemical degradation of n-methylpyrrolidone and its influence on single walled carbon nanotube dispersion. *Chemical Communications*, 51(93):16621–16624, September 2015. 3, 51, 97.

[55] Sean P Ogilvie, Matthew J Large, Giuseppe Fratta, Manuela Meloni, Ruben Canton-Vitoria, Nikos Tagmatarchis, Florian Massuyeau, Christopher P Ewels, Alice AK King, and Alan B Dalton. Considerations for spectroscopy of liquid-exfoliated 2d materials: Emerging photoluminescence of n-methyl-2-pyrrolidone. *Scientific Reports*, 7(1):16706, December 2017. 3, 51, 97.

[56] Gerald L Kennedy and Robert D Short. Biological effects of acetamide, formamide, and their monomethyl and dimethyl derivatives. *CRC critical reviews in toxicology*, 17(2):129–182, 1986.

[57] Agency for Toxic Substances and Disease Registry (ATSDR). Toxfaqs for chloroform. `https://www.atsdr.cdc.gov/ToxProfiles/tp6.pdf`, 2015.

[58] Agency for Toxic Substances and Disease Registry (ATSDR). Toxfaqs for methylene chloride. `https://www.atsdr.cdc.gov/toxprofiles/tp14.pdf`, 2019.

[59] Lei Liu, Zhigang Shen, Min Yi, Xiaojing Zhang, and Shulin Ma. A green, rapid and size-controlled production of high-quality graphene sheets by hydrodynamic forces. *Rsc Advances*, 4(69):36464–36470, 2014.

[60] Shuaishuai Liang, Min Yi, Zhigang Shen, Lei Liu, Xiaojing Zhang, and Shulin Ma. One-step green synthesis of graphene nanomesh by fluid-based method. *RSC Advances*, 4(31):16127–16131, 2014.

[61] HM Solomon, BA Burgess, GL Kennedy, and RE Staples. 1-methyl-2-pyrrolidone (nmp): reproductive and developmental toxicity study by inhalation in the rat. *Drug and chemical toxicology*, 18(4):271–293, 1995.

[62] Naya A Stini, Petros L Gkizis, and Christoforos G Kokotos. Cyrene: a bio-based novel and sustainable solvent for organic synthesis. *Green Chemistry*, 24(17):6435–6449, 2022.

[63] Jason E Camp. Bio-available solvent cyrene: synthesis, derivatization, and applications. *ChemSusChem*, 11(18):3048–3055, 2018.

[64] João Fernandes, Siva Sankar Nemala, Giovanni De Bellis, and Andrea Capasso. Green solvents for the liquid phase exfoliation production of graphene: the promising case of cyrene. *Frontiers in Chemistry*, 10:878799, 2022.

[65] J. Occhiuzzi, G.G. Politano, G. D'olimpio, and A. Politano. The quest for green solvents for the sustainable production of nanosheets of two-dimensional (2d) materials, a key issue in the roadmap for the ecology transition in the flatland. *Molecules*, 28(5):1484, 2023.

[66] Joanna Cytarska, Joanna Szulc, Dominika Kolodziej-Sobczak, Jessica Alves Nunes, Edeildo Ferreira da Silva-Junior, and Krzysztof Z LKaczkowski. Cyrene as a tyrosinase inhibitor and anti-browning agent. *Food Chemistry*, 442:138430, 2024.

[67] Tiziana Marino, Francesco Galiano, Antonio Molino, and Alberto Figoli. New frontiers in sustainable membrane preparation: Cyrene™ as green bioderived solvent. *Journal of Membrane Science*, 580:224–234, Jun 2019.

[68] Jaber Adam, Manjot Singh, Avazbek Abduvakhidov, Maria Rosaria Del Sorbo, Chiara Feoli, Fida Hussain, Jasneet Kaur, et al. The effectiveness of cyrene as a solvent in exfoliating 2d tmds nanosheets. *International Journal of Molecular Sciences*, 24(13):10450, 2023.

[69] Xiao Li, Jingyang Shan, Weizhen Zhang, Shao Su, Lihui Yuwen, and Lianhui Wang. Recent advances in synthesis and biomedical applications of two-dimensional transition metal dichalcogenide nanosheets. *Small*, 13(5):1602660, 2017.

[70] Tae In Kim, Bu kil Kwon, Jonghee Yoon, I. Park, G. Bang, Yongkeun Park, Yeo S. Seo, and Sung-Yool Choi. Antibacterial activities of graphene oxide-molybdenum disulfide nanocomposite films. *ACS applied materials & interfaces*, 9 9:7908–7917, 2017.

[71] Shounak Roy, A. Mondal, Varnika Yadav, A. Sarkar, Ruptanu Banerjee, Pallab Sanpui, and Amit K Jaiswal. Mechanistic insight into the antibacterial activity of chitosan exfoliated mos2 nanosheets: Membrane damage, metabolic inactivation, and oxidative stress. *ACS applied bio materials*, 2 7:2738–2755, 2019.

[72] U. Qumar, M. Ikram, M. Imran, A. Haider, A. ul Hamid, J. Haider, K. Riaz, and S. Ali. Synergistic effect of bi-doped exfoliated mos2 nanosheets on their bactericidal and dye degradation potential. *Dalton transactions*, 2020.

[73] Michael Bae, J. Oh, Shuhao Liu, N. Nagabandi, Y. Yegin, William DeFlorio, L. Cisneros-Zevallos, and E. Scholar. Nanotoxicity of 2d molybdenum disulfide, mos2, nanosheets on beneficial soil bacteria, bacillus cereus and pseudomonas aeruginosa. *Nanomaterials*, 11, 2021.

[74] M. Kumari and Hemant K. Kashyap. Mos2 nanosheet induced destructive alterations in the escherichia coli bacterial membrane. *Soft matter*, 2022.

[75] Qilan Xu, P. Zhu, Jiarong Zhang, Yuhui Liu, Ling Cai, Hui jun Jiang, Minghui Ji, and Jin Chen. Electrochemical formation of distinct nanostructured mos2 with altered antibacterial activity. *Materials Letters*, 271:127809, 2020.

[76] E. Karwowska, M. Kostecki, A. Sokołowska, R. Chodun, and K. Zdunek. Peculiar role of the metallic states on the nano-mos2 ceramic particle surface in antimicrobial and antifungal activity. *International Journal of Applied Ceramic Technology*, 12:885–890, 2015.

[77] Qin Gao, Xiao Zhang, Wenyan Yin, D. Ma, Changjian Xie, L. Zheng, Xinghua Dong, Linqiang Mei, Jie Yu, Chaozhan Wang, Zhanjun Gu, and Yuliang Zhao. Functionalized mos2 nanovehicle with near-infrared laser-mediated nitric oxide release and photothermal activities for advanced bacteria-infected wound therapy. *Small*, 14 45:e1802290, 2018.

[78] Si Chen, Nibin Shi, Min Huang, X. Tan, Xin Yan, Aodi Wang, Yuxiong Huang, R. Ji, Dong mei Zhou, Yong guan Zhu, A. Keller, J. Gardea-Torresdey, J. White, and Lijuan Zhao. Mos2 nanosheets-cyanobacteria interaction: Reprogrammed carbon and nitrogen metabolism. *ACS nano*, 2021.

[79] Y Zhao, Y Jia, J Xu, L Han, F He, and X Jiang. The antibacterial activities of mos2 nanosheets towards multi-drug resistant bacteria. *Chemical Communications (Cambridge, England)*, 57(24):2998–3001, 2021.

[80] F. Salvat et al. Penelope: a code system for monte carlo simulation of electron and photon transport. *Workshop Proceedings, OECD Nuclear Energy Agency, Issyles-Moulineaux*, 2001.

[81] J. Sempau, J. M. Fernández-Varea, E. Acosta, and F. Salvat. Experimental benchmarks of the monte carlo code penelope. *Nuclear Instruments and Methods in Physics Research Section B: Beam Interactions with Materials and Atoms*, 207(2):107–123, 2003.

[82] Xu Cui, Chenzhen Zhang, Rui Hao, and Yanglong Hou. Liquid-phase exfoliation, functionalization and applications of graphene. *Nanoscale*, 3(5):2118–2126, 2011.

[83] Alexandra S Pavlova, Ekaterina A Obraztsova, Alexey V Belkin, Christelle Monat, Pedro Rojo-Romeo, and Elena D Obraztsova. Liquid-phase exfoliation of flaky graphite. *Journal of Nanophotonics*, 10(1):012525–012525, 2016.

[84] Najme Sadat Taghavi and Reza Afzalzadeh. The effect of sonication parameters on the thickness of the produced mos2 nano-flakes. *Archives of Acoustics*, pages 31–40, 2021.

[85] Horacio J Salavagione, James Sherwood, Mario De bruyn, Vitaliy L Budarin, Gary J Ellis, James H Clark, and Peter S Shuttleworth. Identification of high performance solvents for the sustainable processing of graphene. *Green Chemistry*, 19(11):2550–2560, 2017.

[86] Jinseon Kim, Sanghyuk Kwon, Dae-Hyun Cho, Byunggil Kang, Hyukjoon Kwon, Youngchan Kim, Sung O. Park, Gwan Yeong Jung, Eunhye Shin, Wan-Gu Kim, Hyungdong Lee, Gyeong Hee Ryu, Minseok Choi, Tae Hyeong Kim, Junghoon Oh, Sungjin Park, Sang Kyu Kwak, Suk Wang Yoon, Doyoung Byun, Zonghoon Lee, and Changgu Lee. Direct exfoliation and dispersion of two-dimensional materials in pure water via temperature control. *Nature Communications*, 6:8294, 2015.

[87] Aideen Griffin, Katharina Nisi, Joshua Pepper, Andrew Harvey, Beata M. Szydłowska, Jonathan N. Coleman, and Claudia Backes. Effect of surfactant choice and concentration on the dimensions and yield of liquid-phase-exfoliated nanosheets. *Chemistry of Materials*, 32:2852–2862, 2020.

[88] D. V. Pinakov, G. N. Chekhova, A. V. Okotrub, and et al. Structure and supercapacitor properties of few-layer low-fluorinated graphene materials. *Journal of Materials Science*, 53:13053–13066, 2018.

[89] Marzieh Kajbafvala and Mansoor Farbod. Effective size selection of mos2 nanosheets by a novel liquid cascade centrifugation: Influences of the flakes dimensions on electrochemical and photoelectrochemical applications. *Journal of colloid and interface science*, 527:159–171, 2018.

[90] C. Backes, D. Hanlon, B.M. Szydlowska, A. Harvey, S. Yuan, V. Vega-Mayoral, B.R. Davies, P.-L. Zhao, D. Hanlon, E.J.G. Santos, et al. Production of highly monolayer enriched dispersions of liquid-exfoliated nanosheets by liquid cascade centrifugation. *ACS Nano*, 10(2):1589–1601, 2016.

[91] Claudia Backes, Thomas M Higgins, Alan Kelly, Conor Boland, Alan Harvey, Damien Hanlon, and Jonathan N Coleman. Guidelines for exfoliation, characterization and processing of layered materials produced by liquid exfoliation. *Chemistry of Materials*, 29(1):243–255, 2017.

[92] E Varrla, C Backes, KR Paton, A Harvey, Z Gholamvand, J McCauley, and JN Coleman. Large-scale production of size-controlled mos2 nanosheets by shear exfoliation. *Chemistry of Materials*, 27(3):1129–1139, 2015.

[93] Gary Cunningham, Mustafa Lotya, Claudio S Cucinotta, Stefano Sanvito, Shane D Bergin, Robert Menzel, and Jonathan N Coleman. Solvent exfoliation of transition metal dichalcogenides: Dispersibility of exfoliated nanosheets varies only weakly between compounds. *ACS Nano*, 6(4):3468–3480, 2012.

[94] Arlene O'Neill, Umar Khan, Peter N Nirmalraj, John Boland, and Jonathan N Coleman. Graphene dispersion and exfoliation in low boiling point solvents. *The Journal of Physical Chemistry C*, 115(13):5422–5428, 2011.

[95] JASCO Inc. Uv-vis spectroscopy instrumentation. `https://jascoinc.com/learning-center/theory/spectroscopy/uv-vis-spectroscopy/instrumentation/`, 2024. Accessed: 2024-06-11.

[96] Andrea C Ferrari and Denis M Basko. Raman spectroscopy as a versatile tool for studying the properties of graphene. *Nature Nanotechnology*, 8(4):235–246, 2013.

[97] H. Li, Q. Zhang, C.C.R. Yap, B.K. Tay, T.H.T. Edwin, A. Olivier, and D. Baillargeat. From bulk to monolayer mos2: Evolution of raman scattering. *Adv. Funct. Mater.*, 22:1385–1390, 2012.

[98] Zhong Lin, Bruno R Carvalho, Ethan Kahn, Ruitao Lv, Rahul Rao, Humberto Terrones, Marcos A Pimenta, and Mauricio Terrones. Defect engineering of two-dimensional transition metal dichalcogenides. *2D Materials*, 3(2):022002, 2016.

[99] C. Lee, H. Yan, L.E. Brus, T.F. Heinz, J. Hone, and S. Ryu. Anomalous lattice vibrations of single- and few-layer mos2. *ACS Nano*, 4:2695–2700, 2010.

[100] X. Zhang, X.-F. Qiao, W. Shi, J.-B. Wu, D.-S. Jiang, and P.-H. Tan. Phonon and raman scattering of two-dimensional transition metal dichalcogenides from monolayer, multilayer to bulk material. *Chem. Soc. Rev.*, 44:2757–2785, 2015.

[101] Ayse Berkdemir, Humberto R Gutiérrez, Andrés R Botello-Méndez, Nestor Perea-López, Ana Laura Elías, Cheng-Wei Chia, and Mauricio Terrones. Identification of individual and few layers of ws2 using raman spectroscopy. *Scientific Reports*, 3(1):1–8, 2013.

[102] Sean Ogilvie. *Liquid phase exfoliation and interfacial assembly of two-dimensional nanomaterials*. Thesis, University of Sussex, 2019.

[103] Andres Castellanos-Gomez, Michele Buscema, Robert Molenaar, Vivek Singh, Liesbeth Janssen, Herre S J van der Zant, and Gary A Steele. Deterministic transfer of two-dimensional materials by all-dry viscoelastic stamping. *2D Materials*, 1(1):011002, 2014.

[104] Hong Li, Jun Wu, Xiaoyu Huang, Guang Lu, Jing Yang, Xuehong Lu, Qihua Xiong, and Hua Zhang. Rapid and reliable thickness identification of two-dimensional nanosheets using optical microscopy. *ACS Nano*, 7(11):10344–10353, 2013.

[105] Jie Wang, Luning Sun, Mingchu Zou, Wei Gao, Chang Liu, Li Shang, Zhenmeng Peng, and Yong Cao. Functionalization of graphene oxide with well-defined poly(n-isopropylacrylamide) via surface-initiated raft polymerization. *Macromolecules*, 51(1):425–433, 2018.

[106] Oxford Instruments. Scanning probe microscopy. `https://raman.oxinst.com/techniques/scanning-probe-microscopy`, 2024. Accessed: 2024-06-11.

[107] Juan I Paredes, Silvia Villar-Rodil, Amelia Martínez-Alonso, and Juan M D Tascón. Graphene oxide dispersions in organic solvents. *Langmuir*, 24(19):10560–10564, 2008.

[108] Hu Tao, Yong Zhang, Yang Gao, Zhenhua Sun, Chang Yan, and John Texter. Scalable exfoliation and dispersion of two-dimensional materials–an update. *Physical Chemistry Chemical Physics*, 16:921–943, 2014.

[109] Yi Lin, T. V. Williams, and John W. Connell. Soluble, exfoliated hexagonal boron nitride nanosheets. *The Journal of Physical Chemistry Letters*, 1(1):277–283, 2009.

[110] Sourav Bhattacharjee. Dls and zeta potential–what they are and what they are not? *Journal of controlled release*, 235:337–351, 2016.

[111] Umar Khan, Arlene O'Neill, Mustafa Lotya, Sukanta De, and Jonathan N Coleman. High-concentration solvent exfoliation of graphene. *Small*, 6(7):864–871, 2010.

[112] Valeria Nicolosi, Manish Chhowalla, Mercouri G Kanatzidis, Michael S Strano, and Jonathan N Coleman. Liquid exfoliation of layered materials. *Science*, 340(6139):1226419, 2013.

[113] Zeiss. Microscope zeiss merlin. `https://mikroskopiadlaprzemyslu.pl/images/doc/microscope-zeiss-merlin-eng.pdf`. Accessed: 2024-06-11.

[114] Physical Electronics. Xps/esca. `https://www.phi.com/surface-analysis-techniques/xps-esca.html`, 2024. Accessed: 2024-06-11.

[115] Dong Yang, Aruna Velamakanni, Gulru Bozoklu, Sungjin Park, Meryl Stoller, Richard D Piner, and Rodney S Ruoff. Chemical analysis of graphene oxide films after heat and chemical treatments by x-ray photoelectron and micro-raman spectroscopy. *Carbon*, 47(1):145–152, 2009.

[116] Luca D'Arsiè, Santiago Esconjauregui, Robert S Weatherup, Xiaojun Wu, Andres Castellanos-Gomez, Julius Surgailis, et al. Stable, scalable, and high-quality graphene synthesis on nickel by controlled, surface-mediated segregation. *RSC Advances*, 6(115):113185–113192, 2016.

[117] Christina Frank, Dirk Werber, Jakob P Cramer, Mitra Askar, Mirko Faber, Matthias an der Heiden, Helen Bernard, Angelika Fruth, Rita Prager, Anke Spode, et al. Epidemic profile of shiga-toxin-producing escherichia coli o104:h4 outbreak in germany. *The New England Journal of Medicine*, 365(19):1771–1780, 2011.

[118] Hannah H Tuson and Douglas B Weibel. Bacteria-surface interactions. *Soft Matter*, 9(18):4368–4380, 2013.

[119] Jun Kyun Oh, Yildiz Yegin, Fang Yang, Ming Zhang, Jian Li, Shiang Huang, Stanislav V Verkhoturov, Erik A Schweikert, Katrina Perez-Lewis, Ethan A Scholar, et al. The influence of surface chemistry on the kinetics and thermodynamics of bacterial adhesion. *Scientific Reports*, 8(1):1–13, 2018.

[120] YH An and RJ Friedman. Concise review of mechanisms of bacterial adhesion to biomaterial surfaces. *Journal of Biomedical Materials Research*, 43(3):338–348, 1998.

[121] A. K Geim and K. S Novoselov. The rise of graphene. In *Nanoscience and Technology: A Collection of Reviews from Nature Journals*, pages 11–19. World Scientific, 2010.

[122] K S Novoselov, V I Fal'ko, L Colombo, P R Gellert, M G Schwab, and K Kim. A roadmap for graphene. *Nature*, 490(7419):192–200, 2012.

[123] Mahmood Aliofkhazraei, Nasar Ali, William I Milne, Cengiz S Ozkan, Stanislaw Mitura, and Jean L Gervasoni. *Graphene Science Handbook: Applications and Industrialization*. CRC Press, Boca Raton, FL, 2016.

[124] Shilpi Goenka, Vimal Sant, and Shilpi Sant. Graphene-based nanomaterials for drug delivery and tissue engineering. *Journal of Controlled Release*, 173:75–88, 2014.

[125] João Santos, Marta Moschetta, Jota Rodrigues, Pedro Alpuim, and Andrea Capasso. Interactions between 2d materials and living matter: A review on graphene and hexagonal boron nitride coatings. *Frontiers in Bioengineering and Biotechnology*, 9:1–25, 2021.

[126] S Gupta, E Heintzman, and J Jasinski. Secondary electron intensity contrast imaging and friction properties of micromechanically cleaved graphene layers on insulating substrates. *Journal of Electronic Materials*, 43(9):3458–3469, 2014.

[127] Teng Liu and Zhuang Liu. 2d mos2 nanostructures for biomedical applications. *Advanced Healthcare Materials*, 7(8):1701158, 2018.

[128] F Xu. *Large scale manufacturing of WS2 nanomaterials and their application in polymer nanocomposites*. PhD thesis, University of Exeter, 2013.

[129] C Zhu, Z Zeng, H Li, F Li, C Fan, and H Zhang. Single-layer mos2-based nanoprobes for homogeneous detection of biomolecules. *Journal of the American Chemical Society*, 135(16):5998–6001, 2013.

[130] Jian Zhen Ou, Adam F Chrimes, Yuan Wang, Shaoyin Tang, Michael S Strano, and Kourosh Kalantar-zadeh. Ion-driven photoluminescence modulation of quasi-two-dimensional mos2 nanoflakes for applications in biological systems. *Nano Letters*, 14(2):857–863, 2014.

[131] W Yin, L Yan, J Yu, G Tian, L Zhou, X Zheng, X Zhang, Y Yong, J Li, Z Gu, et al. High-throughput synthesis of single-layer mos2 nanosheets as a near-infrared photothermal-triggered drug delivery for effective cancer therapy. *ACS Nano*, 8(7):6922–6933, 2014.

[132] S Wang, X Li, Y Chen, X Cai, H Yao, W Gao, Y Zheng, X An, J Shi, and H Chen. A facile one-pot synthesis of a two-dimensional mos2/bi2s3 composite theranostic nanosystem for multi-modality tumor imaging and therapy. *Advanced Materials (Deerfield Beach, Fla.)*, 27(17):2775–2782, 2015.

[133] Teng Liu, Chao Wang, Wenying Cui, Hua Gong, Chengyu Liang, Xiaoyan Shi, Zhen Li, Bai Sun, and Zhuang Liu. Combined photothermal and photodynamic therapy delivered by pegylated mos2 nanosheets. *Nanoscale*, 6(19):11219–11225, 2014.

[134] H.F. Liu, S.L. Wong, and D.Z. Chi. Cvd growth of mos2-based two-dimensional materials. *Chemical Vapor Deposition*, 21(7-8-9):241–259, 2015.

[135] J Yu, W Yin, X Zheng, G Tian, X Zhang, T Bao, X Dong, Z Wang, Z Gu, X Ma, et al. Smart mos2/fe3o4 nanotheranostic for magnetically targeted photothermal therapy guided by magnetic resonance/photoacoustic imaging. *Theranostics*, 5(9):931–945, 2015.

[136] Athanasios B Bourlinos, Vasilios Georgakilas, Radek Zboril, Theodore A Steriotis, and Athanasios K Stubos. Liquid-phase exfoliation of graphite towards solubilized graphenes. *Small (Weinheim an Der Bergstrasse, Germany)*, 5(16):1841–1845, 2009.

[137] S Tkachev, M Monteiro, J Santos, E Placidi, M Ben Hassine, P Marques, P Ferreira, P Alpuim, and A Capasso. Environmentally friendly graphene inks for touch screen sensors. *Advanced Functional Materials*, 31(33):2103287, 2021.

[138] Viviane Forsberg, Ru Zhang, Joakim Bäckström, Christina Dahlström, Britta Andres, Magnus Norgren, Mattias Andersson, Magnus Hummelgård, and Håkan Olin. Exfoliated MoS2 in water without additives. *PloS One*, 11(4):e0154522, 2016.

[139] Ryan J Barnes, Rodrigo Molina, Jiaqiang Xu, Peter J Dobson, and Ian P Thompson. Comparison of tio2 and zno nanoparticles for photocatalytic degradation of methylene blue and the correlated inactivation of gram-positive and gram-negative bacteria. *Journal of Nanoparticle Research*, 15(2):1–11, 2013.

[140] V I Syngouna and C V Chrysikopoulos. Inactivation of ms2 bacteriophage by titanium dioxide nanoparticles in the presence of quartz sand with and without ambient light. *Journal of Colloid and Interface Science*, 497:117–125, 2017.

[141] V I Syngouna and C V Chrysikopoulos. Bacteriophage ms2 and titanium dioxide heteroaggregation: Effects of ambient light and the presence of quartz sand. *Colloids and Surfaces B: Biointerfaces*, 180:281–288, 2019.

[142] V I Syngouna, K I Kourtaki, M P Georgopoulou, and C V Chrysikopoulos. The role of nanoparticles (titanium dioxide, graphene oxide) on the inactivation of co-existing bacteria in the presence and absence of quartz sand. *Environmental Science and Pollution Research International*, 29(13):19199–19211, 2022.

[143] W Zhou, X Gao, D Liu, and X Chen. Gold nanoparticles for in vitro diagnostics. *Chemical Reviews*, 115(19):10575–10636, 2015.

[144] Wojciech Pajerski, Dorota Ochonska, Monika Brzychczy-Wloch, Piotr Indyka, Maciej Jarosz, Sylwia Golda-Cepa, Zbigniew Sojka, and Andrzej Kotarba. Attachment efficiency of gold nanoparticles by gram-positive and gram-negative bacterial strains governed by surface charges. *Journal of Nanoparticle Research*, 21(8):1–12, 2019.

[145] M Singh, C Zannella, V Folliero, RD Girolamo, F Bajardi, A Chianese, L Altucci, A Damasco, MR Del Sorbo, C Imperatore, et al. Combating actions of green 2d-materials on gram positive and negative bacteria and enveloped viruses. *Frontiers in Bioengineering and Biotechnology*, 8:1–26, 2020.

[146] Maria P Georgopoulou, Vasiliki I Syngouna, and Constantinos V Chrysikopoulos. Influence of graphene oxide nanoparticles on the transport and cotransport of biocolloids in saturated porous media. *Colloids and Surfaces B: Biointerfaces*, 189:110841, 2020.

[147] Jacob Israelachvili. *Intermolecular and Surface Forces*. Academic Press, Elsevier, 2011.

[148] Jennifer Samphire, Yuiko Takebayashi, Stephen A Hill, Nicholas Hill, Kate J Heesom, Philip A Lewis, Dominic Alibhai, Eilis C Bragginton, Josephine Dorh, Neciah Dorh, et al. Green fluorescent carbon dots as targeting probes for led-dependent bacterial killing. *Nano Select*, 3(3):662–672, 2022.

[149] Hiroyuki Ohshima and Kimiko Makino. *Colloid and interface science in pharmaceutical research and development.* Elsevier, 2014.

[150] Gwanghyun Hwang, Insung S Ahn, Byung Jin Mhin, and Jin Young Kim. Adhesion of nano-sized particles to the surface of bacteria: Mechanistic study with the extended dlvo theory. *Colloids and Surfaces B: Biointerfaces*, 97:138–144, 2012.

[151] Magdy Farahat, Tsuyoshi Hirajima, Keiko Sasaki, and Kenji Doi. Adhesion of escherichia coli onto quartz, hematite and corundum: Extended dlvo theory and flotation behavior. *Colloids and Surfaces B: Biointerfaces*, 74(1):140–149, 2009.

[152] Tania M Mohona, Amit Gupta, A B M Masud, Shu-Ching Chien, Lih-Ching Lin, Prathima C Nalam, and Nirupam Aich. Aggregation behavior of inorganic 2d nanomaterials beyond graphene: Insights from molecular modeling and modified dlvo theory. *Environmental Science & Technology*, 53(8):4161–4172, 2019.

[153] Zachary S Baird, Petri Uusi-Kyyny, Juho P Pokki, Eugene Pedegert, and Ville Alopaeus. Vapor pressures, densities, and pc-saft parameters for 11 bio-compounds. *International Journal of Thermophysics*, 40(11):1–36, 2019.

[154] Sigma-Aldrich. The future of solvents: Bio renewable. Online, 2019. 10-03-2022.

[155] Farbod Alimohammadi, Meisam Sharifian Gh, Nuwan H Attanayake, Akila C Thenuwara, Yury Gogotsi, Babak Anasori, and Daniel R Strongin. Antimicrobial properties of 2d MnO2 and MoS2 nanomaterials vertically aligned on graphene materials and Ti3C2 MXene. *Langmuir: The ACS Journal of Surfaces and Colloids*, 34(24):7192–7200, 2018.

[156] Shajia Begum, Avijit Pramanik, Kent Gates, Yong Gao, and Paresh C Ray. Antimicrobial peptide-conjugated mos2-based nanoplatform for multimodal synergistic inactivation of superbugs. *ACS Applied Bio Materials*, 2(2):769–776, 2019.

[157] K Tang, L Wang, H Geng, J Qiu, H Cao, and X Liu. Molybdenum disulfide (mos2) nanosheets vertically coated on titanium for disinfection in the dark. *Arabian Journal of Chemistry*, 13(1):1612–1623, 2020.

[158] C L C Rodriguez, P A R Munoz, K Z Donato, L Seixas, R K Donato, and G J M Fechine. Understanding the unorthodox stabilization of liquid phase exfoliated molybdenum disulfide (mos2) in water medium. *Physical Chemistry Chemical Physics : PCCP*, 22(3):1457–1465, 2020.

[159] James Sherwood, Mario De bruyn, Andri Constantinou, Laurianne Moity, Con Robert McElroy, Thomas J Farmer, Timothy Duncan, William Raverty, Andrew J Hunt, and James H Clark. Dihydrolevoglucosenone (cyrene) as a bio-based alternative for dipolar aprotic solvents. *Chemical Communications (Cambridge, England)*, 50(68):9650–9652, 2014.

[160] Sharyn Brown, James P Santa Maria, Jr, and Suzanne Walker. Wall teichoic acids of gram-positive bacteria. *Annual Review of Microbiology*, 67:313–336, 2013.

[161] Andrew L Lovering, Sherif S Safadi, and Natalie CJ Strynadka. Structural perspective of peptidoglycan biosynthesis and assembly. *Annual Review of Biochemistry*, 81:451–478, 2012.

[162] Joseph A H Romaniuk and Lynette Cegelski. Bacterial cell wall composition and the influence of antibiotics by cell-wall and whole-cell nmr. *Philosophical Transactions of the Royal Society B: Biological Sciences*, 370(1679):20150024, 2015.

[163] JJ Maurer, DP Schmidt, P Petrosko, S Sanchez, L Bolton, and MD Lee. Development of primers to o-antigen biosynthesis genes for specific detection of escherichia coli o157 by pcr. *Applied and Environmental Microbiology*, 65(7):2954–2960, 1999.

[164] L Brown, JM Wolf, R Prados-Rosales, and Arturo Casadevall. Through the wall: Extracellular vesicles in gram-positive bacteria, mycobacteria and fungi. *Nature Reviews. Microbiology*, 13(10):620–630, 2015.

[165] Emilisa Frirdich and Chris Whitfield. Lipopolysaccharide inner core oligosaccharide structure and outer membrane stability in human pathogens belonging to the enterobacteriaceae. *Journal of Endotoxin Research*, 11(3):133–144, 2005.

[166] Timothy D Ho and Matthew K Waldor. Enterohemorrhagic escherichia coli o157:h7 gal mutants are sensitive to bacteriophage p1 and defective in intestinal colonization. *Infection and Immunity*, 75(4):1661–1666, 2007.

[167] Madeleine Ramstedt, Ryuma Nakao, Sun Nyunt Wai, Bernt Eric Uhlin, and Jean-François Boily. Monitoring surface chemical changes in the bacterial cell wall: Multivariate analysis of cryo-x-ray photoelectron spectroscopy data. *The Journal of Biological Chemistry*, 286(14):12389–12396, 2011.

[168] K.S. Novoselov, D. Jiang, F. Schedin, T.J. Booth, V.V. Khotkevich, S.V. Morozov, and A.K. Geim. Two-dimensional atomic crystals. *Proceedings of the National Academy of Sciences of the United States of America*, 102(28):10451–10453, 2005.

[169] J.M. Raimond, M. Brune, Q. Computation, F. de Martini, and C. Monroe. Electric field effect in atomically thin carbon films. *Science*, 306(5696):666–670, 2004.

[170] X. Huang, Z. Zeng, and H. Zhang. Metal dichalcogenide nanosheets: Preparation, properties and applications. *Chemical Society Reviews*, 42(5):1934–1946, 2013.

[171] B. Li, C. Lai, G. Zeng, D. Huang, L. Qin, M. Zhang, M. Cheng, X. Liu, H. Yi, C. Zhou, et al. Black phosphorus, a rising star 2d nanomaterial in the post-graphene era: Synthesis, properties, modifications, and photocatalysis applications. *Small*, 15:e1804565, 2019.

[172] Z. Guo, W. Ding, X. Liu, Z. Sun, and L. Wei. Two-dimensional black phosphorus: A new star in energy applications and the barrier to stability. *Applied Materials Today*, 14:51–58, 2019.

[173] K. Kalantar-Zadeh and J.Z. Ou. Biosensors based on two-dimensional mos2. *ACS Sensors*, 1(1):5–16, 2016.

[174] Y. Chen, C. Tan, H. Zhang, and L. Wang. Two-dimensional graphene analogues for biomedical applications. *Chemical Society Reviews*, 44(9):2681–2701, 2015.

[175] X. Li and H. Zhu. Two-dimensional mos2: Properties, preparation, and applications. *Journal of Materials*, 1:33–44, 2015.

[176] M. Chhowalla, Z. Liu, and H. Zhang. Two-dimensional transition metal dichalcogenide (tmd) nanosheets. *Chemical Society Reviews*, 44(9):2584–2586, 2015.

[177] H. Yuan, H. Wang, and Y. Cui. Two-dimensional layered chalcogenides: From rational synthesis to property control via orbital occupation and electron filling. *Accounts of Chemical Research*, 48(1):81–90, 2015.

[178] S.B. Desai, S.R. Madhvapathy, M. Amani, D. Kiriya, M. Hettick, M. Tosun, Y. Zhou, M. Dubey, J.W. Ager, D. Chrzan, et al. Gold-mediated exfoliation of ultralarge optoelectronically-perfect monolayers. *Advanced Materials*, 28(20):4053–4058, 2016.

[179] J. Shi, R. Tong, X. Zhou, Y. Gong, Z. Zhang, Q. Ji, Y. Zhang, Q. Fang, L. Gu, X. Wang, et al. Temperature-mediated selective growth of mos2/ws2 and ws2/mos2 vertical stacks on au foils for direct photocatalytic applications. *Advanced Materials*, 28(51):10664–10672, 2016.

[180] K.-G. Zhou, N.-N. Mao, H.-X. Wang, Y. Peng, and H.-L. Zhang. A mixed-solvent strategy for efficient exfoliation of inorganic graphene analogues. *Angewandte Chemie International Edition*, 50(47):10839–10842, 2011.

[181] M.A. Lukowski, A.S. Daniel, F. Meng, A. Forticaux, L. Li, and S. Jin. Enhanced hydrogen evolution catalysis from chemically exfoliated metallic mos2 nanosheets. *Journal of the American Chemical Society*, 135(28):10274–10277, 2013.

[182] A. Jawaid, D. Nepal, K. Park, M. Jespersen, A. Qualley, P. Mirau, L.F. Drummy, and R.A. Vaia. Mechanism for liquid phase exfoliation of mos2. *Chemistry of Materials*, 28(2):337–348, 2016.

[183] A. Gupta, V. Arunachalam, and S. Vasudevan. Liquid-phase exfoliation of mos2 nanosheets: The critical role of trace water. *The Journal of Physical Chemistry Letters*, 7(23):4884–4890, 2016.

[184] C.-X. Hu, Y. Shin, O. Read, and C. Casiraghi. Dispersant-assisted liquid-phase exfoliation of 2d materials beyond graphene. *Nanoscale*, 13(1):460–484, 2021.

[185] J. Shen, Y. He, J. Wu, C. Gao, K. Keyshar, X. Zhang, Y. Yang, M. Ye, R. Vajtai, J. Lou, et al. Liquid phase exfoliation of two-dimensional materials by directly probing and matching surface tension components. *Nano Letters*, 15(9):5449–5454, 2015.

[186] R.A. Sheldon. Metrics of green chemistry and sustainability: Past, present, and future. *ACS Sustainable Chemistry & Engineering*, 6(1):32–48, 2018.

[187] N. Guajardo and P.D. de María. Assessing biocatalysis using dihydrolevoglucosenone (cyrene™) as versatile bio-based (co)solvent. *Molecular Catalysis*, 485:110813, 2020.

[188] D. Kong and A.V. Dolzhenko. Cyrene: A bio-based sustainable solvent for organic synthesis. *Sustainable Chemistry and Pharmacy*, 25:100591, 2022.

[189] M. De Bruyn, J. Fan, V.L. Budarin, D.J. Macquarrie, L.D. Gomez, R. Simister, T.J. Farmer, W.D. Raverty, S.J. McQueen-Mason, and J.H. Clark. A new perspective in bio-refining: Levoglucosenone and cleaner lignin from waste biorefinery hydrolysis lignin by selective conversion of residual saccharides. *Energy & Environmental Science*, 9(8):2571–2574, 2016.

[190] K. Pan, Y. Fan, T. Leng, J. Li, Z. Xin, J. Zhang, L. Hao, J. Gallop, K.S. Novoselov, and Z. Hu. Sustainable production of highly conductive multilayer graphene ink for wireless connectivity and iot applications. *Nature Communications*, 9(1):5197, 2018.

[191] J. Adam, M.R. Del Sorbo, J. Kaur, R. Romano, M. Singh, M. Valadan, and C. Altucci. Surface interactions studies of novel two-dimensional molybdenum disulfide with gram-negative and gram-positive bacteria. *Analytical Letters*, 56(2):357–371, 2022.

[192] Y. Xu, H. Cao, Y. Xue, B. Li, and W. Cai. Liquid-phase exfoliation of graphene: An overview on exfoliation media, techniques, and challenges. *Nanomaterials*, 8(12):942, 2018.

[193] F. Mori, M. Kubouchi, and Y. Arao. Effect of graphite structures on the productivity and quality of few-layer graphene in liquid-phase exfoliation. *Journal of Materials Science*, 53(18):12807–12815, 2018.

[194] P. He, J. Cao, H. Ding, C. Liu, J. Neilson, Z. Li, I.A. Kinloch, and B. Derby. Screen-printing of a highly conductive graphene ink for flexible printed electronics. *ACS Applied Materials & Interfaces*, 11(34):32225–32234, 2019.

[195] A. Citarella, A. Amenta, D. Passarella, and N. Micale. Cyrene: A green solvent for the synthesis of bioactive molecules and functional biomaterials. *International Journal of Molecular Sciences*, 23(4):15960, 2022.

[196] J. Kaur, M. Singh, C. Dell‘aversana, R. Benedetti, P. Giardina, M. Rossi, M. Valadan, A. Vergara, A. Cutarelli, A.M.I. Montone, et al. Biological interactions of biocompatible and water-dispersed mos2 nanosheets with bacteria and human cells. *Scientific Reports*, 8(1):16386, 2018.

[197] G. Rusciano, A. Capaccio, A. Sasso, M. Singh, M. Valadan, C. Dell’aversana, L. Altucci, and C. Altucci. Single-cell photothermal analysis induced by mos2 nanoparticles by raman spectroscopy. *Frontiers in Bioengineering and Biotechnology*, 10:844011, 2022.

[198] J. Wilson and A. Yoffe. The transition metal dichalcogenides discussion and interpretation of the observed optical, electrical and structural properties. *Advances in Physics*, 18(73):193–335, 1969.

[199] Claudia Backes, Damien Hanlon, Beata M Szydlowska, Andrew Harvey, Ronan J Smith, Thomas M Higgins, and Jonathan N Coleman. Preparation of liquid-exfoliated transition metal dichalcogenide nanosheets with controlled size and thickness: a state of the art protocol. *JoVE (Journal of Visualized Experiments)*, N/A(118):e54806, 2016.

[200] Claudia Backes, Ronan J Smith, Niall McEvoy, Nina C Berner, David McCloskey, Hannah C Nerl, Arlene O'Neill, Paul J King, Tom Higgins, Damien Hanlon, et al. Edge and confinement effects allow in situ measurement of size and thickness of liquid-exfoliated nanosheets. *Nature communications*, 5(1):4576, 2014.

[201] Liudmil Antonov and Daniela Nedeltcheva. Resolution of overlapping uv–vis absorption bands and quantitative analysis. *Chemical Society Reviews*, 29(3):217–227, 2000.

[202] Shivani Sharma, Shubham Bhagat, Jasvir Singh, Ravi Chand Singh, and Sandeep Sharma. Excitation-dependent photoluminescence from ws2 nanostructures synthesized via top-down approach. *Journal of Materials Science*, 52(19):11326–11336, 2017.

[203] Konstantinos Kouroupis-Agalou, Andrea Liscio, Emanuele Treossi, Luca Ortolani, Vittorio Morandi, Nicola Maria Pugno, and Vincenzo Palermo. Fragmentation and exfoliation of 2-dimensional materials: a statistical approach. *Nanoscale*, 6(11):5926–5933, 2014.

[204] M.A. Bissett, S.D. Worrall, I.A. Kinloch, and R.A.W. Dryfe. Comparison of two-dimensional transition metal dichalcogenides for electrochemical supercapacitors. *Electrochimica Acta*, 201:30–37, 2016.

[205] Y. Chen. Growth of a large, single-crystalline ws2 monolayer for high-performance photodetectors by chemical vapor deposition. *Micromachines*, 12(2):137, 2021.

[206] R.D. Deegan, O. Bakajin, T.F. Dupont, G. Huber, S.R. Nagel, and T.A. Witten. Capillary flow as the cause of ring stains from dried liquid drops. *Nature*, 389(6653):827–829, 1997.

[207] C. Backes, D. Campi, B.M. Szydlowska, K. Synnatschke, E. Ojala, F. Rashvand, A. Harvey, A. Griffin, Z. Sofer, N. Marzari, et al. Equipartition of energy defines the size–thickness relationship in liquid-exfoliated nanosheets. *ACS Nano*, 13:7050–7061, 2019.

[208] S. Ott, N. Wolff, F. Rashvand, V.J. Rao, J. Zaumseil, and C. Backes. Impact of the mos2 starting material on the dispersion quality and quantity after liquid phase exfoliation. *Chemistry of Materials*, 31(20):8424–8431, 2019.

[209] H. Ma, Z. Shen, and S. Ben. Understanding the exfoliation and dispersion of mos2 nanosheets in pure water. *Journal of Colloid and Interface Science*, 517:204–212, 2018.

[210] W. Li, Z. Yang, M. Sun, and J. Dong. Interlayer interactions in transition metal dichalcogenides heterostructures. *Reviews in Physics*, 9:100077, 2022.

[211] I.C. Gerber, E. Courtade, S. Shree, C. Robert, T. Taniguchi, K. Watanabe, A. Balocchi, P. Renucci, D. Lagarde, X. Marie, et al. Interlayer excitons in bilayer mos2 with strong oscillator strength up to room temperature. *Physical Review B*, 99(3):035443, 2018.

[212] Z. Cheng, B. Zhang, X. An, Z. Lu, G. Zhang, F. Ma, and F. Zhou. First-principles delimitation of the boundary between intralayer and interlayer in two-dimensional structures. *The Journal of Physical Chemistry C*, 123(44):26912–26920, 2019.

[213] S. Ott, M. Lakmann, and C. Backes. Impact of pretreatment of the bulk starting material on the efficiency of liquid phase exfoliation of ws2. *Nanomaterials*, 11(4):1072, 2021.

[214] W. Qiao, S. Yan, X. He, X. Song, Z. Li, X. Zhang, W. Zhong, and Y. Du. Effects of ultrasonic cavitation intensity on the efficient liquid-exfoliation of mos2 nanosheets. *RSC Advances*, 4(98):50981–50987, 2014.

[215] Landon B. Oakes, Cary Pint, Rizia Bardhan, Yang Xu, Joan Valentine, and Paul Laibinis. *Controlling Nanomaterial Assembly to Improve Material Performance in Energy Storage Electrodes*. PhD thesis, Vanderbilt University, 2016.

[216] G.-Q. Han, Y.-R. Liu, W.-H. Hu, B. Dong, X. Li, Y.-M. Chai, Y.-Q. Liu, and C.-G. Liu. Ws2 nanosheets based on liquid exfoliation as effective electrocatalysts for hydrogen evolution reaction. *Materials Chemistry and Physics*, 167:271–277, 2015.

[217] F. Ghasemi and S. Mohajerzadeh. Sequential solvent exchange method for controlled exfoliation of mos2 suitable for phototransistor fabrication. *ACS Applied Materials & Interfaces*, 8(48):31179–31191, 2016.

[218] J. Kaur, A.M. Gravagnuolo, P. Maddalena, C. Altucci, P. Giardina, and F. Gesuele. Green synthesis of luminescent and defect-free bio-nanosheets of mos2: Interfacing two-dimensional crystals with hydrophobins. *RSC Advances*, 7(36):22400–22408, 2017.

[219] L. Pan, Y.-T. Liu, X.-M. Xie, and X.-Y. Ye. Facile and green production of impurity-free aqueous solutions of ws2 nanosheets by direct exfoliation in water. *Small*, 12(47):6703–6713, 2016.

[220] V. Paolucci, G. D'olimpio, L. Lozzi, A.M. Mio, L. Ottaviano, M. Nardone, G. Nicotra, P. Le-Cornec, C. Cantalini, and A. Politano. Sustainable liquid-phase exfoliation of layered materials with nontoxic polarclean solvent. *ACS Sustainable Chemistry & Engineering*, 8(48):18830–18840, 2020.

[221] Hiroyuki Ohshima. Theory of electrostatics and electrokinetics of soft particles. *Science and Technology of Advanced Materials*, 10(6):063001, 2009.

[222] A. Gupta and S. Vasudevan. Understanding surfactant stabilization of mos2 nanosheets in aqueous dispersions from zeta potential measurements and molecular dynamics simulations. *The Journal of Physical Chemistry C*, 122(34):19243–19250, 2018.

[223] B. Chakraborty, A. Das, A. Kumar, A. Barui, M. Kumar, and C.R. Chaudhuri. Real time estimation of stem cell zeta potential and dimension during proliferation using mos2 nanosheets field effect transistor. *Sensors and Actuators B: Chemical*, 380:133351, 2023.

[224] Wei-Ming Huang, Wei-Siang Liao, Yu-Min Lai, and I-Wen Peter Chen. Tuning the surface charge density of exfoliated thin molybdenum disulfide sheets via non-covalent functionalization for promoting hydrogen evolution reaction. *Journal of Materials Chemistry C*, 8(2):510–517, 2020.

[225] A. Gupta, V. Arunachalam, and S. Vasudevan. Water dispersible, positive and negatively charged mos2 nanosheets: Surface chemistry and the role of surfactant binding supporting information content. *The Journal of Physical Chemistry Letters*, 6(4):739–744, 2015.

[226] Matthew A Diasio and David L Green. The effect of solvent viscosity on production of few-layer graphene from liquid-phase exfoliation of graphite. *MRS Advances*, 4(3-4):241–247, 2019.

[227] N. Baig, I. Kammakakam, W. Falath, and I. Kammakakam. Nanomaterials: A review of synthesis methods, properties, recent progress, and challenges. *Materials Advances*, 2(6):1821–1871, Mar. 2021.

[228] S. C. Currall, E. B. King, N. Lane, J. Madera, and S. Turner. What drives public acceptance of nanotechnology? `www.luxresearchinc.com/compass.html`, 2006.

[229] G. R. Bhimanapati et al. Recent advances in two-dimensional materials beyond graphene. *ACS Nano*, 9(12):11509–11539, Nov. 06 2015.

[230] Manish Chhowalla, Hyeon Suk Shin, Goki Eda, Lain-Jong Li, Kian Ping Loh, and Hua Zhang. The chemistry of two-dimensional layered transition metal dichalcogenide nanosheets. *Nature chemistry*, 5(4):263–275, 2013.

[231] Q. Fu et al. Synthesis and enhanced electrochemical catalytic performance of monolayer ws2(1-x)se2x with a tunable band gap. *Adv. Mater.*, 27(32):4732–4738, Aug. 2015.

[232] H. Yuan et al. Application of two-dimensional mos2 nanosheets in the property improvement of polyimide matrix: Mechanical and thermal aspects. *Compos. Part A Appl. Sci. Manuf.*, 95:220–228, Apr. 2017.

[233] B. Zhao et al. 2d metallic transition-metal dichalcogenides: Structures, synthesis, properties, and applications. *Advanced Functional Materials*, 31(48), Nov. 01 2021.

[234] W. Zhou, H. Gong, X. Jin, Y. Chen, H. Li, and S. Liu. Recent progress of two-dimensional transition metal dichalcogenides for thermoelectric applications. *Frontiers in Physics*, 10, Mar. 11 2022.

[235] J. Kaur et al. Electrostatically driven scalable synthesis of mos2-graphene hybrid films assisted by hydrophobins. *RSC Adv.*, 7(79):50166–50175, 2017.

[236] J. Pellico, P. J. Gawne, and R. T. M. De Rosales. Radiolabelling of nanomaterials for medical imaging and therapy. *Chemical Society Reviews*, 50(5):3355–3423, Mar. 07 2021.

[237] L. Fusco et al. Graphene and other 2d materials: A multidisciplinary analysis to uncover the hidden potential as cancer theranostics. *Theranostics*, 10(12):5435–5488, 2020.

[238] Steven Y Yap, Thomas W Price, Huguette Savoie, Ross W Boyle, and Graeme J Stasiuk. Selective radiolabelling with 68 ga under mild conditions: a route towards a porphyrin pet/pdt theranostic agent. *Chemical communications*, 54(57):7952–7954, 2018.

[239] N. Huo, Y. Yang, and J. Li. Optoelectronics based on 2d tmds and heterostructures. *J. Semicond.*, 38(3), Mar. 2017.

[240] T. Mueller and E. Malic. Exciton physics and device application of two-dimensional transition metal dichalcogenide semiconductors. *npj 2D Materials and Applications*, 2(1), Dec. 01 2018.

[241] S. K. Liao et al. Satellite-to-ground quantum key distribution. *Nature*, 549(7670):43–47, Sep. 2017.

[242] K. Alexandrou et al. Improving the radiation hardness of graphene field effect transistors. *Appl. Phys. Lett.*, 109(15), Oct. 2016.

[243] T. Vogl et al. Radiation tolerance of two-dimensional material-based devices for space applications. *Nat. Commun.*, 10(1), Dec. 2019.

[244] A. V. Krasheninnikov. Are two-dimensional materials radiation tolerant? *Nanoscale Horizons*, 5(11):1447–1452, Nov. 01 2020.

[245] K. Guo, A. Baidak, and Z. Yu. Recent advances in green synthesis and modification of inorganic nanomaterials by ionizing and non-ionizing radiation. *Journal of Materials Chemistry A*, 8(44):23029–23058, Nov. 28 2020.

[246] G. Y. Zhao et al. Recent progress on irradiation-induced defect engineering of two-dimensional 2h-mos 2 few layers. *Appl. Sci.*, 9(4), Feb. 2019.

[247] Guosheng Song, Liang Cheng, Yu Chao, Kai Yang, and Zhuang Liu. Emerging nanotechnology and advanced materials for cancer radiation therapy. *Advanced materials*, 29(32):1700996, 2017.

[248] Eslam Aboelezz and Brian W Pogue. Review of nanomaterial advances for ionizing radiation dosimetry. *Applied Physics Reviews*, 10(2), 2023.

[249] J. Patel and A. Patel. Nano drug delivery systems for space applications. In *Handbook of Space Pharmaceuticals*, pages 1–22. Springer International Publishing, 2019.

[250] A. Abedini, M. Saraji, A. A. A. Bakar, P. Susthitha Menon, and S. Shaari. Gamma–radiation-assisted synthesis of luminescent zno/ag heterostructure core–shell nanocomposites. *Plasmonics*, 13:771–778, 2018.

[251] M. A. Hubaut, A. Fagart, and D. Tonnelet. Gallium 68. *Med. Nucl.*, 42(6):463–465, 2018.

[252] J. Cal-González, J. L. Herraiz, S. España, P. G. Corzo, J. J. Vaquero, M. Desco, and J. M. Udias. Positron range estimations with penelopet. *Physics in Medicine & Biology*, 58(15):5127, 2013.

[253] J. Allison et al. Recent developments in geant4. *Nuclear instruments and methods in physics research section A: Accelerators, Spectrometers, Detectors and Associated Equipment*, 835:186–225, 2016.

[254] S. Incerti et al. The geant4-dna project. *International Journal of Modeling, Simulation, and Scientific Computing*, 1(02):157–178, 2010.

[255] G. A. P. Cirrone et al. Validation of the geant4 electromagnetic photon cross-sections for elements and compounds. *Nuclear Instruments and Methods in Physics Research Section A: Accelerators, Spectrometers, Detectors and Associated Equipment*, 618(1-3):315–322, 2010.

[256] R Ribberfors. X-ray incoherent scattering total cross sections and energy-absorption cross sections by means of simple calculation routines. *Physical Review A*, 27(6):3061, 1983.

[257] C. Moore et al. In vitro localisation and degradation of few-layer mos2 submicrometric plates in human macrophage-like cells: A label free raman micro-spectroscopic study. *2D Mater.*, 7(2), 2020.

[258] R. J. Smith et al. Large-scale exfoliation of inorganic layered compounds in aqueous surfactant solutions. *Adv. Mater.*, 23(34):3944–3948, 2011.

[259] C. Huo et al. 2d materials via liquid exfoliation: a review on fabrication and applications. *Sci. Bull.*, 60(23):1994–2008, Dec. 2015.

[260] Intek Song, Chibeom Park, and Hee Cheul Choi. Synthesis and properties of molybdenum disulphide: from bulk to atomic layers. *RSC Adv.*, 5:749, 2015.

[261] Yeung Yu Hui, Xiaofei Liu, Wenjing Jie, Ngai Yui Chan, Jianhua Hao, Yu-Te Hsu, Lain-Jong Li, Wanlin Guo, and Shu Ping Lau. Exceptional tunability of band energy in a compressively strained trilayer mos2 sheet. *ACS Nano*, 7(8):7126–7131, 2013.

[262] J. F. Felix et al. A comprehensive study on the effects of gamma radiation on the physical properties of a two-dimensional ws2 monolayer semiconductor. *Nanoscale Horizons*, 5(2):259–267, 2020.

[263] Yupu He et al. γ-ray dose dependent conductivity of mos2 nanomaterials at different temperatures. *CrystEngComm*, 21(44):6830–6837, 2019.

[264] L. Zhang et al. 2d atomic crystal molecular superlattices by soft plasma intercalation. *Nat Commun*, 11:5960, 2020.

[265] D Ganta, S Sinha, and Richard T Haasch. 2-d material molybdenum disulfide analyzed by xps. *Surface Science Spectra*, 21(1):19–27, 2014.

[266] H. Lamkaouane et al. Efficient and facile synthetic route of moo3:mos2 hybrid thin layer via oxidative reaction of mos2 nanoflakes. *Nanomaterials*, 12, 2022.

[267] P. Afanasiev and C. Lorentz. Oxidation of nanodispersed mos2 in ambient air: The products and the mechanistic steps. *Journal of Physical Chemistry C*, 123:7486–7494, 2019.

[268] T. Y. Ko et al. On-stack two-dimensional conversion of mos2 into moo3. *2D Materials*, 4, 2017.

[269] I. A. de Castro et al. Molybdenum oxides – from fundamentals to functionality. *Advanced Materials*, 29, 2017.

[270] Albert Bruix, Henrik Gøbel Fuchtbauer, Anders K Tuxen, Alexander S Walton, Mie Andersen, Søren Porsgaard, Flemming Besenbacher, Bjørk Hammer, and Jeppe V Lauritsen. In situ detection of active edge sites in single-layer mos2 catalysts. *ACS nano*, 9(9):9322–9330, 2015.

[271] Burcu Ozden, Min P Khanal, Juhong Park, Sunil Uprety, Vahid Mirkhani, Kosala Yapabandara, Kyunghyuk Kim, Marcelo Kuroda, Michael J Bozack, Wonbong Choi, et al. Raman and x-ray photoelectron spectroscopy investigation of the effect of gamma-ray irradiation on mos2. *Micro & Nano Letters*, 12(4):271–274, 2017.

[272] C. Y. Xu et al. Homogeneous surface oxidation and triangle patterning of monolayer mos 2 by hydrogen peroxide. *Appl Surf Sci*, 452:451–456, 2018.

[273] M. Karamitros et al. Modeling radiation chemistry in the geant4 toolkit. *Prog. Nucl. Sci. Technol*, 2:503–508, 2011.

[274] M. Karamitros et al. Diffusion-controlled reactions modeling in geant4-dna. *Journal of Computational Physics*, 274:841–882, 2014.

[275] J. L. Capelo-Martinez. *Microwaves in Organic Synthesis Practical Microwave Synthesis for Organic Chemists Microinstrumentation.* Wiley-VCH Verlag GmbH, 2009.

[276] D. Bianco, C. Villagrasa, and M. Dos Santos. Multi-scale analysis of simulated proton and alpha irradiation. *Radiat Prot Dosimetry*, 164:444–448, 2015.

[277] S. Mignuzzi et al. Effect of disorder on raman scattering of single-layer mo s2. *Phys. Rev. B - Condens. Matter Mater. Phys.*, 91(19), May 2015.

[278] Namphung Peimyoo, Jingzhi Shang, Weihuang Yang, Yanlong Wang, Chunxiao Cong, and Ting Yu. Thermal conductivity determination of suspended mono-and bilayer ws 2 by raman spectroscopy. *Nano Research*, 8:1210–1221, 2015.

[279] G. Chinga, O. Gregersen, B. Dougherty, and M. Anal. Paper surface characterisation by laser profilometry and image analysis. *Microscopy and Analysis*, 96:21–24, 2003.